

AD-A072 839

MASSACHUSETTS INST OF TECH CAMBRIDGE AEROPHYSICS LAB F/G 20/4  
TURBULENT BOUNDARY LAYERS ON AN AIRFOIL IN SEVERAL ADVERSE PRES-ETC(U)  
AUG 78 R T CERVISI F49620-77-C-0031

UNCLASSIFIED

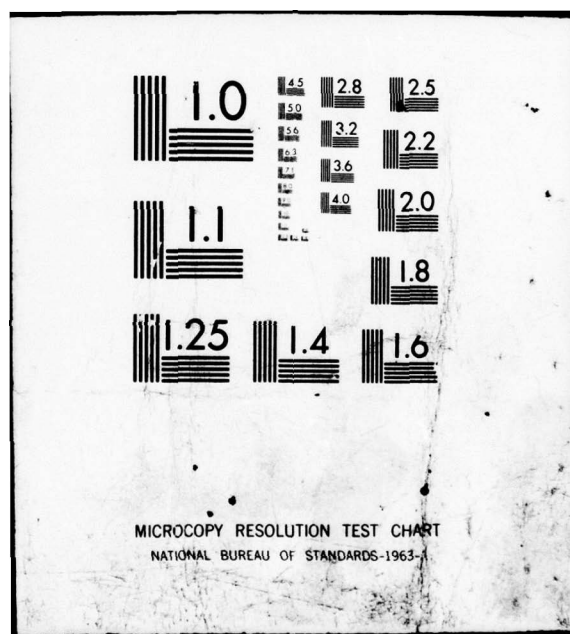
MIT-TR-203

AFOSR-TR-78-1450

NL

1 OF 2  
AD  
A072B39





~~LEVEL~~2  
B.S.

TURBULENT BOUNDARY LAYERS ON AN AIRFOIL IN SEVERAL  
ADVERSE PRESSURE GRADIENTS

AD A0728839

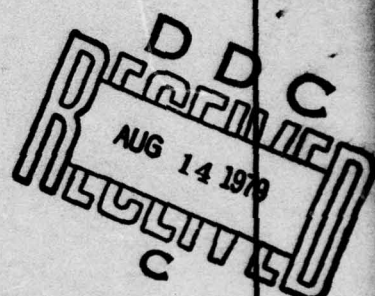
MASSACHUSETTS INSTITUTE OF TECHNOLOGY  
 AEROPHYSICS LABORATORY

560 Memorial Drive, Cambridge, MA 02139

TR 203

by

Richard T. Cervisi



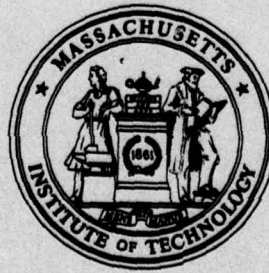
## FINAL SCIENTIFIC REPORT

AFOSR CONTRACT F49620-77C-0031

OSP 84744

August, 1978

DDC FILE COPY



This document has been approved  
 for public release and sale; its  
 distribution is unlimited.

DISTRIBUTION UNLIMITED

AIR FORCE OFFICE OF SCIENTIFIC RESEARCH (AFSC)  
NOTICE OF TRANSMITTAL TO DDC

This technical report has been reviewed and is  
approved for public release IAW AFR 190-12 (7b).  
Distribution is unlimited.

A. D. BLOSE  
Technical Information Officer

ADA072839

REPORT DOCUMENTATION PAGE		READ INSTRUCTIONS BEFORE COMPLETING FORM	
1. REPORT NUMBER	18 AFOSR TR-78-1450	2. GOVT ACCESSION NO.	3. RECIPIENT'S CATALOG NUMBER
4. TITLE (and Subtitle)	TURBULENT BOUNDARY LAYERS ON AN AIRFOIL IN SEVERAL ADVERSE PRESSURE GRADIENTS.		
5. TYPE OF REPORT & PERIOD COVERED	FINAL rept. 1 Jan 77 - 30 Jun 78		
6. PERFORMING ORG. REPORT NUMBER	MIT-TR-203		
7. AUTHOR(s)	10 RICHARD T. CERVISI		
8. CONTRACT OR GRANT NUMBER(s)	15 F49620-77-C-0031		
9. PERFORMING ORGANIZATION NAME AND ADDRESS	16 MASSACHUSETTS INSTITUTE OF TECHNOLOGY AEROSPHYSICS LABORATORY CAMBRIDGE, MASSACHUSETTS 02139		
11. CONTROLLING OFFICE NAME AND ADDRESS	17 AIR FORCE OFFICE OF SCIENTIFIC RESEARCH/NA BLDG 410 BOLLING AIR FORCE BASE, D C 20332		
14. MONITORING AGENCY NAME & ADDRESS (if different from Controlling Office)	18 (12) 135p.		
16. DISTRIBUTION STATEMENT (of this Report)	Approved for public release; distribution unlimited.		
17. DISTRIBUTION STATEMENT (of the abstract entered in Block 20, if different from Report)	D D C Approved AUG 14 1979 C REF ID: A642142		
18. SUPPLEMENTARY NOTES			
19. KEY WORDS (Continue on reverse side if necessary and identify by block number)	GROUND TESTING WIND TUNNELS UNSTEADY FLOW UNSTEADY BOUNDARY LAYER		
20. ABSTRACT (Continue on reverse side if necessary and identify by block number)	Turbulent boundary layer profiles in a wide range of adverse pressure gradients (.0019 < p* < .1040) were measured using a boundary layer velocity-flow angle measuring probe designed for this experiment. The different pressure gradients were created on a NACA 0012 airfoil by changing the angular orientation of an elliptic cylinder placed near the airfoils trailing edge. Rotating the elliptic cylinder to various angular positions changed the effective angle of attack and camber of the airfoil-ellipse combination thereby creating different pressure distributions about the airfoil. In anticipation of spinning the ellipse to over		

create an unsteady flow in future experiments, this experiment defined the steady state environment. The boundary layer profiles are presented in three different graphical formats; conventional nondimensional plots, profiles in modified Law of the Wall coordinates and Velocity Defect Law graphs. The Law of the Wall was modified to account for longitudinal streamline curvature. Local skin friction coefficients were found using the modified Law of the Wall in the form of a Clauser chart. The boundary layer data was checked for repeatability, consistency and agreement with theory and previous experiments. The final results were deemed excellent.

Accession For	
NTIS	GRANT
DDC TAB	<input checked="" type="checkbox"/>
Unannounced	<input type="checkbox"/>
Justification	
By	
Distribution	
Availability Codes	
Dist	Avail and/or special

UNCLASSIFIED

TURBULENT BOUNDARY LAYERS ON AN AIRFOIL IN SEVERAL  
ADVERSE PRESSURE GRADIENTS

by

Richard T. Cervisi

Submitted to the Department of  
Aeronautics and Astronautics on August 18, 1978  
in partial fulfillment of the requirements for  
the degree of Master of Science

ABSTRACT

Turbulent boundary layer profiles in a wide range of adverse pressure gradients ( $.0019 \leq p^* \leq .1040$ ) were measured using a boundary layer velocity-flow angle measuring probe designed for this experiment. The different pressure gradients were created on a NACA 0012 airfoil by changing the angular orientation of an elliptic cylinder placed near the airfoil's trailing edge. Rotating the elliptic cylinder to various angular positions changed the effective angle of attack and camber of the airfoil-ellipse combination thereby creating different pressure distributions about the airfoil. In anticipation of spinning the ellipse to create an unsteady flow in future experiments, this experiment defined the steady state environment.

The boundary layer profiles are presented in three different graphical formats; conventional nondimensional plots, profiles in modified Law of the Wall coordinates and Velocity Defect Law graphs. The Law of the Wall was modified to account for longitudinal streamline curvature. Local skin friction coefficients were found using the modified Law of the Wall in the form of a Clauser chart.

The boundary layer data was checked for repeatability, consistency and agreement with theory and previous experiments. The final results were deemed excellent.

Thesis Supervisor: Eugene E. Covert  
Title: Professor of Aeronautics  
and Astronautics

This document has been approved  
for public release and sale; its  
distribution is unlimited.

## ACKNOWLEDGEMENTS

I would like to thank Professor Covert for his assistance and friendly advice. It was always a pleasant and educational experience when I approached him for help. Frank Durgin must also be thanked for his help and insights and applauded for enduring my continual interruptions. My gratitude goes, too, to Janice Lucci for her excellent typing, to Joe Marksteiner for his fine workmanship on the probe and to Mike Lazar and Jerry Fanucci for their help and for providing me with humorous interludes. I would also like to express my appreciation to the Air Force Office of Scientific Research for sponsoring the experiments. Finally, my special thanks goes to Joan, my wife, for her help and boundless patience.

This Final Report on contract F49620-77-C-0031 for the period January 1, 1977 to June 30, 1978 covers work prepared since the last interim report from January 1, 1978 to June 30, 1978.

Accession For	
NTIS GEN&I <input checked="" type="checkbox"/>	
DDC TAB <input type="checkbox"/>	
Unannounced <input type="checkbox"/>	
Justification _____	
By _____	
Distribution/ _____	
Availability Codes _____	
Dist	Avail and/or special
A	

## TABLE OF CONTENTS

<u>CHAPTER</u>		<u>PAGE</u>
	Introduction	15
I	Description of the Experiment and Associated Instrumentation	21
II	Procedure, Problems and Solutions	24
III	Reducing the Data	26
IV	Discussion of Results	34
V	Conclusions and Recommendations	45
 <u>APPENDICES</u>		
A	Propagation of Errors	48
B	Calculating Coordinates of Probe Mounting Holes for Given Axial Measuring Station	51
C	References	53
 <u>TABLES</u>		
 <u>FIGURES</u>		

## LIST OF SYMBOLS AND ABBREVIATIONS

Traditional	Computer Graphics
A	Constant in Law of the Law
B	Constant in Law of the Law
c	Chord
$c_f$	Local coefficient of skin friction
$c_p$	Pressure coefficient
$delh$	Dynamic pressure (inch of alcohol)
e	Rate of strain
G	Clauser's boundary layer family parameter eq. 3.12
h	Vertical distance from the chord at which the ellipse is located
H	Tradition boundary layer family parameter, equals $\delta^*/\theta$
HS	High speed
$\lambda$	Mixing length
LS	Low speed
NO	No ellipse
p	Pressure ( $lb/ft^2$ )
$p^*$	Dimensionless pressure gradient parameter, eq. I.4
q	Dynamic pressure ( $lb/ft^2$ )
R	Local Radius of curvature of the airfoil (ft)
RC	Resistor-capacitor circuit

## LIST OF SYMBOLS AND ABBREVIATIONS-CONTINUED

Traditional	Computer Graphics	
SD		Standard deviation
T		Temperature ( $^{\circ}$ C)
u	U	Velocity in the boundary layer parallel to the airfoil surface
$u_{\tau}$	$U_T$	Friction velocity, eq. 3.3
$-\rho \overline{u'v'}$		Reynold's shear stress
$U_{\infty}$		Free stream velocity potential
$U_p$		Potential velocity at the airfoil surface, eq 4.1
$U_{\theta}$		u velocity at $y = \theta$
v		Velocity in the boundary layer perpendicular to airfoil surface
V		Volts
x	X	Axial position measured form airfoil's leading edge
y	Y	Distance normal to the airfoil surface
$\alpha$	ALPHA	Ellipse angle, positive in clockwise direction, equals zero when semi-major axis is parallel with the airfoil chord
$\alpha'$		Empirical constant in discussion of effects of streamline curvature
$\beta$		Constant
$\gamma$		$U_{\theta}/U_p$
$\delta$		Boundary layer height

## LIST OF SYMBOLS AND ABBREVIATIONS-CONTINUED

Traditional	Computer Graphics	
$\delta^*$	DT	Displacement thickness, eq.3.9
$\Delta$	CT	Clauser's thickness, eq.3.8
$\theta$	MT	Momentum thickness, eq.3.5
$\kappa$		von Karman's constant
$\mu$		Viscosity ( $\text{lb.sec}/\text{ft}^2$ )
$\nu$		Kinematic viscosity ( $\text{ft}^2/\text{sec}$ )
$\rho$		Density ( $\text{lb.sec}^2/\text{ft}^4$ )
$\tau$		Shear stress
$\tau_w$		Wall shear stress

## LIST OF TABLES

TABLE		PAGE
I	Procedure and Run Schedule	55
II	The Ratio of Potential Velocity at the Airfoil Surface to Freestream Velocity as a Function of Ellipse Angle for the Two Boundary Layer Measuring Stations.	59
III	Characteristic Boundary Layer Parameters and Dimensionalizing Data.	60

LIST OF FIGURES

FIGURE	PAGE
1. Schematic diagram of the experiment	64
2. Plan view and typical section of Wright Brothers Wind Tunnel	65
3. Several different views of the airfoil, ellipse, probe and sideboards	66
4.(a, b) The boundary layer velocity-flow angle measuring probe	67
a. Photographs	
b. Schematic diagram	
5. Circuitry used to control probe movements	69
6. Circuitry used to find the zero height voltage	70
7. Velocity vs. Hot Wire Volts; hot wire calibration curves for one days runs	71
8.(a, b) Modified Clauser chart	72
a. Examples of determining $c_f$	
b. Clauser chart further modified with an improved mixing length assumption	
9. Pressure coefficient vs. nondimensional chord	No ellipse 74
Run A: $q_\infty = 6.84 \text{ lb./ft}^2$	
Run B: $q_\infty = 25.55$	
Ref. [18]	
10. Pressure coefficient vs. nondimensional chord	$\alpha = 0^\circ$ 75
Run C: $q_\infty = 6.37 \text{ lb./ft}^2$	
Run D: $q_\infty = 25.38$	
11. Pressure coefficient vs. nondimensional chord	$\alpha = 45^\circ$ 76
Run E: $q_\infty = 6.73 \text{ lb./ft}^2$	
Run F: $q_\infty = 26.07$	
12. Pressure coefficient vs. nondimensional chord	$\alpha = 90^\circ$ 77
Run G: $q_\infty = 6.39 \text{ lb./ft}^2$	

FIGURE	PAGE
13. Pressure coefficient vs. nondimensional chord Run I: $q = 26.30 \text{ lb/ft}^2$ Run J: $q_\infty = 6.20$	$\alpha = 135^\circ$ 78
14. Axial pressure coefficient gradient vs. $\alpha$ at $x/c = .6875$ and $x/c = .9380$	79
15. Conventional nondimensional boundary layer profiles: $u/U_p$ vs $y/\theta$ 15. $u/U_p$ vs $y/\theta$ $x/c = .6875$ No ellipse 80 Run 2: $U_\infty = 148.0 \text{ ft/sec}$	
16. $u/U_p$ vs $y/\theta$ $x/c = .6875$ No ellipse 81 Run 3: $U_\infty = 73.5 \text{ ft/sec}$ Run 4: $U_\infty = 74.7$	
17. $u/U_p$ vs $y/\theta$ $x/c = .6875$ $\alpha = 0^\circ$ 82 Run 7: $U_\infty = 73.6 \text{ ft/sec}$ Run 8: $U_\infty = 73.2$	
18. $u/U_p$ vs $y/\theta$ $x/c = .6875$ $\alpha = 45^\circ$ 83 Run 9: $U_\infty = 73.2 \text{ ft/sec}$ Run 10: $U_\infty = 73.2$	
19. $u/U_p$ vs $y/\theta$ $x/c = .6875$ $\alpha = 45^\circ$ 84 Run 11: $U_\infty = 147.5 \text{ ft/sec}$	
20. $u/U_p$ vs $y/\theta$ $x/c = .6875$ $\alpha = 90^\circ$ 85 Run 13: $U_\infty = 74.6 \text{ ft/sec}$ Run 14: $U_\infty = 78.6$	
21. $u/U_p$ vs $y/\theta$ $x/c = .6875$ $\alpha = 135^\circ$ 86 Run 17: $U_\infty = 75.7 \text{ ft/sec}$ Run 18: $U_\infty = 75.8$	
22. $u/U_p$ vs $y/\theta$ $x/c = .6875$ $\alpha = 135^\circ$ 87 Run 20: $U_\infty = 153.4 \text{ ft/sec}$	
23. $u/U_p$ vs $y/\theta$ $x/c = .9380$ $\alpha = 0^\circ$ 88 Run 21: $U_\infty = 74.2 \text{ ft/sec}$ Run 22: $U_\infty = 74.2$	

## FIGURE

24. $u/U_p$ vs $y/\theta$	$x/c = .9380$	$\alpha = 0^\circ$	89
Run 24: $U_\infty = 147.6$ ft/sec			
25. $u/U_p$ vs $y/\theta$	$x/c = .9380$	$\alpha = 45^\circ$	90
Run 25: $U_\infty = 75.1$ ft/sec			
Run 26: $U_\infty = 75.1$			
26. $u/U_p$ vs $y/\theta$	$x/c = .9380$	$\alpha = 45^\circ$	91
Run 27: $U_\infty = 148.1$ ft/sec			
Run 28: $U_\infty = 148.1$			
27. $u/U_p$ vs $y/\theta$	$x/c = .9380$	$\alpha = 90^\circ$	92
Run 29: $U_\infty = 74.2$ ft/sec			
Run 30: $U_\infty = 74.2$			
28. $u/U_p$ vs $y/\theta$	$x/c = .9380$	$\alpha = 90^\circ$	93
Run 32: $U_\infty = 149.8$ ft/sec			
29. $u/U_p$ vs $y/\theta$	$x/c = .9380$	$\alpha = 135^\circ$	94
Run 33: $U_\infty = 150.6$ ft/sec			
Run 34: $U_\infty = 150.5$			
30. $u/U_p$ vs $y/\theta$	$x/c = .9380$	$\alpha = 135^\circ$	95
Run 35: $U_\infty = 74.5$ ft/sec			
Run 36: $U_\infty = 74.5$			
31. $u/U_p$ vs $y/\theta$	$x/c = .9380$	No ellipse	96
Run 37: $U_\infty = 74.4$ ft/sec			
Run 38: $U_\infty = 74.4$			
32. $u/U_p$ vs $y/\theta$	$x/c = .9380$	No ellipse	97
Run 39: $U_\infty = 150.3$ ft/sec			
Run 40: $U_\infty = 150.3$			
33. Comparison of the present experiment's boundary layer profiles with theory and past experiment by plotting: $\gamma$ vs. $H$			98
34. Momentum thickness vs. ellipse angle			99

Boundary layer profiles in Law of the Wall coordinates:

$u/u_\tau$ vs $yu_\tau/v$			
35. $u/u_\tau$ vs $yu_\tau/v$	$x/c = .6875$	No ellipse	100
Run 2: $U_\infty = 148.0$ ft/sec			
Run 3: $U_\infty = 73.5$			
Run 4: $U_\infty = 74.7$			
36. $u/u_\tau$ vs $yu_\tau/v$	$x/c = .6875$	$\alpha = 0^\circ$	101
Run 7: $U_\infty = 73.6$ ft/sec			
Run 8: $U_\infty = 73.2$			
37. $u/u_\tau$ vs $yu_\tau/v$	$x/c = .6875$	$\alpha = 45^\circ$	102
Run 9: $U_\infty = 73.2$ ft/sec			
Run 10: $U_\infty = 73.2$			
Run 11: $U_\infty = 147.6$			
Run 12: $U_\infty = 147.5$			

## FIGURE

Boundary layer profiles in Law of the Wall coordinates:

 $u/u_\tau$  vs  $yu_\tau/v$  (continued)

38.  $u/u_\tau$  vs  $yu_\tau/v$   $x/c = .6875$   $\alpha = 90^\circ$  103  
 Run 13:  $U_\infty = 74.9$  ft/sec  
 Run 14:  $U_\infty^\infty = 78.6$

39.  $u/u_\tau$  vs  $yu_\tau/v$   $x/c = .6875$   $\alpha = 135^\circ$  104  
 Run 17:  $U_\infty = 75.7$  ft/sec  
 Run 18:  $U_\infty^\infty = 75.8$   
 Run 20:  $U_\infty^\infty = 153.4$

40.  $u/u_\tau$  vs  $yu_\tau/v$   $x/c = .9380$   $\alpha = 0^\circ$  105  
 Run 21:  $U_\infty = 74.2$  ft/sec  
 Run 22:  $U_\infty = 74.2$   
 Run 24:  $U_\infty = 147.6$

41.  $u/u_\tau$  vs  $yu_\tau/v$   $x/c = .9380$   $\alpha = 45^\circ$  106  
 Run 25:  $U_\infty = 75.1$  ft/sec  
 Run 26:  $U_\infty = 75.1$   
 Run 27:  $U_\infty = 148.1$   
 Run 28:  $U_\infty = 148.1$

42.  $u/u_\tau$  vs  $yu_\tau/v$   $x/c = .9380$   $\alpha = 90^\circ$  107  
 Run 29:  $U_\infty = 74.2$  ft/sec  
 Run 30:  $U_\infty = 74.2$   
 Run 32:  $U_\infty = 149.8$

43.  $u/u_\tau$  vs  $yu_\tau/v$   $x/c = .9380$   $\alpha = 135^\circ$  108  
 Run 33:  $U_\infty = 150.6$  ft/sec  
 Run 34:  $U_\infty = 150.5$   
 Run 35:  $U_\infty = 74.5$   
 Run 36:  $U_\infty = 74.5$

44.  $u/u_\tau$  vs  $yu_\tau/v$   $x/c = .9380$  No ellipse 109  
 Run 37:  $U_\infty = 74.4$  ft/sec  
 Run 38:  $U_\infty = 74.4$   
 Run 39:  $U_\infty = 150.3$   
 Run 40:  $U_\infty = 150.3$

45.  $c_f$  as determined from the modified Clauser chart vs.  $c_f$  calculated from Ludwieg and Tillman's empirical equation. 110

FIGURE	PAGE
46. The local skin friction coefficient vs. ellipse angle	111
47. The nondimensional pressure gradient ( $p^*$ ) vs. ellipse angle	112
Boundary layer profiles plotted in Velocity Defect Law coordinates: $(U_p - u) / u_\tau$ vs. $y/\Delta$	
48. $(U_p - u) / u_\tau$ vs. $y/\Delta$	No ellipse 113
Run 2: $U_\infty = 148.0$ ft/sec	$x/c = .6875$
Run 39: $U_\infty = 150.3$	$x/c = .9380$
49. $(U_p - u) / u_\tau$ vs $y/\Delta$	No ellipse 114
Run 3: $U_\infty = 73.5$ ft/sec	$x/c = .6875$
Run 37: $U_\infty = 74.4$	$x/c = .9380$
50. $(U_p - u) u_\tau$ vs $y/\Delta$	No ellipse 115
Run 4: $U_\infty = 74.7$ ft/sec	$x/c = .6875$
Run 38: $U_\infty = 74.4$	$x/c = .6875$
51. $(U_p - u) / u_\tau$ vs $y/\Delta$	No ellipse 116
Run 40: $U_\infty = 150.3$ ft/sec	$x/c = .9380$
52. $(U_p - u) / u_\tau$ vs $y/\Delta$	$\alpha = 0^\circ$ 117
Run 7: $U_\infty = 73.6$ ft/sec	$x/c = .6875$
Run 21: $U_\infty = 74.2$	$x/c = .9380$
53. $(U_p - u) / u_\tau$ vs $y/\Delta$	$\alpha = 0^\circ$ 118
Run 8: $U_\infty = 73.2$ ft/sec	$x/c = .6875$
Run 22: $U_\infty = 74.2$	$x/c = .9380$
54. $(U_p - u) / u_\tau$ vs $y/\Delta$	$\alpha = 0^\circ$ 119
Run 24: $U_\infty = 147.6$ ft/sec	$x/c = .9380$
55. $(U_p - u) / u_\tau$ vs $y/\Delta$	$\alpha = 45^\circ$ 120
Run 9: $U_\infty = 73.2$ ft/sec	$x/c = .6875$
Run 26: $U_\infty = 75.1$	$x/c = .9380$
56. $(U_p - u) / u_\tau$ vs $y/\Delta$	$\alpha = 45^\circ$ 121
Run 10: $U_\infty = 73.2$ ft/sec	$x/c = .6875$
Run 25: $U_\infty = 74.1$	$x/c = .9380$
57. $(U_p - u) / u_\tau$ vs $y/\Delta$	$\alpha = 45^\circ$ 122
Run 11: $U_\infty = 147.6$ ft/sec	$x/c = .6875$
Run 27: $U_\infty = 148.1$	$x/c = .9380$

## FIGURE

## PAGE

Boundary layer profiles plotted in Velocity Defect Law Coordinates: $(U_p - u) / u_\tau$ vs $y / \Delta$ (Continued)		
58. $(U_p - u) / u_\tau$ vs $y / \Delta$	$\alpha = 45^\circ$	123
Run 12: $U_\infty = 147.5$ ft/sec	$x/c = .6875$	
Run 28: $U_\infty = 148.1$	$x/c = .9380$	
59. $(U_p - u) / u_\tau$ vs $y / \Delta$	$\alpha = 90^\circ$	124
Run 13: $U_\infty = 74.9$ ft/sec	$x/c = .6875$	
Run 29: $U_\infty = 74.2$	$x/c = .9380$	
60. $(U_p - u) / u_\tau$ vs $y / \Delta$	$\alpha = 90^\circ$	125
Run 14: $U_\infty = 78.6$ ft/sec	$x/c = .6875$	
Run 30: $U_\infty = 74.2$	$x/c = .9380$	
61. $(U_p - u) / u_\tau$ vs $y / \Delta$	$\alpha = 90^\circ$	126
Run 32: $U_\infty = 149.8$ ft/sec	$x/c = .9380$	
62. $(U_p - u) / u_\tau$ vs $y / \Delta$	$\alpha = 135^\circ$	127
Run 17: $U_\infty = 75.7$ ft/sec	$x/c = .6875$	
Run 18: $U_\infty = 74.5$	$x/c = .9380$	
63. $(U_p - u) / u_\tau$ vs $y / \Delta$	$\alpha = 135^\circ$	128
Run 18: $U_\infty = 75.8$ ft/sec	$x/c = .6875$	
Run 36: $U_\infty = 74.5$	$x/c = .9380$	
64. $(U_p - u) / u_\tau$ vs $y / \Delta$	$\alpha = 135^\circ$	129
Run 20: $U_\infty = 153.4$ ft/sec	$x/c = .6875$	
Run 33: $U_\infty = 150.6$	$x/c = .9380$	
65. $(U_p - u) / u_\tau$ vs $y / \Delta$	$\alpha = 135^\circ$	130
Run 34: $U_\infty = 150.5$ ft/sec	$x/c = .9380$	
66. $(U_p - u) / u_\tau$ vs $y / \Delta$		131
Flat plate turbulent boundary layer profile from Phase 1		
67. The ratio of Clauser's thickness to boundary layer height vs. the equilibrium family parameter: $\Delta/\delta$ vs. G.		132

## INTRODUCTION

This thesis presents the findings, conclusions and recommendations of the second phase of a project whose goal is a better understanding of unsteady boundary layers, particularly those driven by unsteady external flows. Important in many aerodynamic applications, concrete examples of such phenomena are provided by the flows in compressors and turbines. In these devices, a series of closely spaced rotating and stationary blades act on the fluid, and each other, to perform and extract work. The interacting potential fields of the blades cause inefficiencies and noise. Energy losses are due in part to the unsteady boundary layers created on each blade. The sound produced is at the blade passing frequency (high in the audible range) and is high intensity. This type of noise is particularly annoying to any listener.

Up to the present time, few experiments have been done to help understand the basic unsteady fluid mechanics. This omission has been due to inherent experimental difficulties. For example, designing and building instrumentation to be mounted on a rotating or oscillating airfoil is a difficult and expensive task. Furthermore, data reduction is complicated by the accelerations imposed on the instruments in such an experiment. But with the need for more fuel efficient powerplants and the passing of stricter noise regulations, further experimental study is warranted both to identify the important parameters and to provide the initial velocity profiles computational fluid physicists need for their finite difference schemes.

In recognition of the experimental difficulties and in response to the above needs, this project's experiment has been designed to eliminate many of the problems and to provide the required data. From linear airfoil theory, it was known that the flow about an airfoil, under certain conditions, could be described by summing the contributions due to thickness, camber and angle of attack. Thickness could be provided by a symmetrical airfoil. Camber and angle of attack could be created by placing an elliptic cylinder (or any smooth cylindrical object) behind\* and below (or above) the symmetric airfoil, (See Fig. 1). Finally, by rotating the elliptic cylinder, the camber and angle of attack could be periodically varied creating a flapping airfoil or alternatively, creating an unsteady external flow about a symmetrical airfoil.

There are great advantages to such an arrangement. An unsteady boundary layer can be studied on an unmoving airfoil with stationary instrumentation. A wide range of pressure distributions can be created by changing the position of the elliptic cylinder with respect to the airfoil. The frequency of oscillation of the external flow is easily controlled by adjusting the cylinder's angular velocity. The limitations of the system are the limitations of linear airfoil theory; the airfoil must be thin and the ellipse cannot be so close to the airfoil as to cause violation of the Kutta condition at the trailing edge, i.e. the boundary layer on the airfoil cannot be allowed to separate. The significant drawback to the

\* The Kutta condition describes the flow dominating character of the trailing edge. Therefore, the flow can be most effectively controlled by locating the elliptical cylinder near this part of the airfoil.

arrangement is the circulation induced by the rotating elliptic cylinder. This circulation must be subtracted from the dynamic potential field to obtain the thickness, camber and angle of attack contributions.

A schematic diagram of the project's experiment is presented in Fig 1. Mounted in the airfoil are 35 static pressure taps. The elliptic cylinder can be moved to several positions with respect to the airfoil to create the desired pressure distributions. From above, the probe is used to measure the velocity profile of the upper surface boundary layer and when the airfoil is not present, the changing angle of attack along the chord generated by the rotating ellipse. Velocity measurements are made with a horizontal hot wire and direction measurements with an X-hot wire. The probe can be moved to about 10 locations along the chord of the airfoil.

The dynamic experimentation will be done in a later phase of the project. Planned work includes determining the amplitude and phase shift of the static pressures and boundary layer velocity profiles on the airfoil and of the flow angles along the chord in response to the rotating ellipse.

The first two phases were concerned with defining the steady state environment and verifying the experiment's design. Phase 1 [ 1 ] confirmed the two dimensionality of the experiment and the accuracy of the data taking equipment by measuring the turbulent boundary layer over a flat plate. Furthermore, after mathematically developing the theory, it was verified experimentally that linear airfoil theory can be used to describe the potential fields of various airfoil-ellipse combinations within the limits of small disturbances and satisfaction of the Kutta condition.

The goals of the present experiment, Phase 2, were the design and testing of a combination boundary layer velocity and flow angle measuring probe, the measurement of the boundary layer over the airfoil for various ellipse orientations and the identification of potential problems in reducing and interpreting the dynamic data. An important part of the second goal was determining the accuracy of using Clauser plots for finding the local skin friction coefficient.

The boundary layer over approximately the last two thirds of the airfoil is turbulent and subject to an adverse pressure gradient. A landmark study of such flows was performed by Clauser [2]. He looked for and found turbulent boundary layers in adverse pressure gradients whose velocity distributions, when plotted as

$$\frac{u - U_p}{u_\tau} \text{ vs. } \frac{y}{\delta} \quad (I.1)$$

were similar. He called these equilibrium profiles. To normalize the velocity defect, Clauser needed the wall shear stress. From a study by Ludwieg and Tillman, he was convinced that the Law of the Wall or Log Law was insensitive to adverse pressure gradients. By writing the Law of the Wall coordinates as

$$\frac{u}{u_\tau} = \frac{u}{U_p} \sqrt{\frac{2}{C_f}} \quad \text{and} \quad \frac{yu_\tau}{\nu} = \frac{yu_p}{\nu} \sqrt{\frac{C_f}{2}} \quad (I.2)$$

and plotting the coefficients of the square root terms using  $C_f$  as a parameter, he created a chart for determining the skin friction coefficient. (see fig. 8). Typical data points from the present experiment are shown in the figure. The line on which the log part of the data falls deter-

mines  $c_f$  for that boundary layer profile.

The Law of the Wall, deduced from assumptions of constant shear stress and of mixing length proportional to  $y$  near the wall, can be written

$$\frac{u}{u_\tau} = A \log_{10} \left( \frac{yu_\tau}{\nu} \right) + B \quad (I.3)$$

where  $A$  and  $B$  are traditionally considered as constants. In reality,  $A$  and  $B$  are probably influenced slightly by Reynold's number in so far as the shear stress is Reynold's number dependent [3]. The value of these constants used to reduce the data of this experiment are  $A=5.5$  and  $B=5.45$ , as measured by Patel [4]. In Patel's paper, he also shows that for sufficiently large values of the parameter

$$P^* = \frac{\nu}{\rho u_\tau^3} \frac{dp}{dx} \quad (I.4)$$

the Log Law breaks down (see fig. 41 for an example). He notes, however, that the values of  $P^*$  in Ludwieg's and Tillman's experiment were less than .00575; small enough for the Log Law to still apply.

From the boundary layer equations of motion, several authors (Townsend, Patel, Galbraith) have deduced the following relation:

$$\frac{\tau}{\tau_w} = 1 + P^* \frac{yu_\tau}{\nu} + \frac{1}{u_\tau^2} \int_0^y \left( u \frac{du}{dx} + \nu \frac{du}{dy} \right) dy \quad (I.5)$$

The Law of the Wall was originally derived from

$$\tau = \text{constant} = \rho \ell^2 \left( \frac{du}{dy} \right)^2 \quad (I.6)$$

assuming  $\tau = \tau_{wall}$  and  $\ell = Ky$ . I.5 clearly shows that  $\tau$  is not constant if  $p^*$  and/or the flow accelerations are sufficiently large. To modify the Log Law, either  $\tau$  must be measured directly or calculated from I.4 [5]. Another modification would be to make a better mixing length assumption. Several alternate assumptions appear in articles by Galbraith [5] and Sturek [6]. These mixing length equations depend on some or all of the following parameters:

$$Y/\delta, \delta^*, p^* \text{ and } \frac{\tau}{\tau_w}(Y)$$

In the preceding paragraphs, the motivation and theoretical basis of the current experiment were developed. The succeeding chapters will describe the experiment and the success of the theory.

## CHAPTER I

DESCRIPTION OF THE EXPERIMENT AND  
ASSOCIATED INSTRUMENTATION

With the exception of the boundary layer velocity-flow angle measuring probe, the equipment used in this experiment was the same as that used in Phase 1. Therefore, the descriptions presented below, except for that of the probe, will be brief.

The experiment was performed in the Wright Brothers Wind Tunnel (fig. 2) at M.I.T. The tunnel is a closed return facility with a top speed of 140 mph at 1 atm. Wind speed is measured with a pitot-static probe and a manometer.

The airfoil and sideboards were mounted in the test section as shown in fig. 3. The airfoil is a NACA 0012 Basic Thickness Form milled in two sections from aluminum. It has a 20 inch chord, a leading edge span of 20 inches and a trailing edge span of 20.25 inches. The divergence is designed to insure a two-dimensional flow by eliminating the displacement thickness of the boundary layers on the plywood sideboards. The sideboards dimensions are 60 x 75 x 1 inch. Static pressure taps are mounted in the sideboards for measuring downstream pressure. During the experiment, tape was used to seal possible cracks between the airfoil edges and the sideboards to eliminate crossflows and insure two-dimensionality.

The airfoil has 17 static pressure taps in its upper half and 18, including the zero angle of attack stagnation point tap, in its lower half. The taps from each half are connected to a Setra Systems No. 237 pressure

transducer though a Scanivalve. The system has a flat frequency response up to 800 Hz.

The elliptic cylinder is made of wood. Its semimajor axis is 5.56 inches, its semiminor axis is 2.42 inches and its span is 20 inches. For the present experiment, the ellipse was mounted at  $x/c = 1.175$  and  $h/c = -0.275$ , one of the positions investigated by Kanevsky [1].

The boundary layer velocity-flow angle measuring probe, fig. 4, was designed to the following requirements. The probe should be mounted 2 feet above the airfoil and be as narrow as possible to minimize interference and blockage. For the boundary layer measurements, at least 3 inches of movement perpendicular to the airfoil surface should be provided. Also, vertical deflection of the probe due to the wind must be less than .001 inches. For future angle of attack measurements, the whole assembly cannot deflect more than .05 degrees. Finally, lateral vibration should be minimized. All of the above requirements were met in the final design.

The probe is operated using the circuit in fig. 5. The distance traversed is measured by a Bourns Inc. linear potentiometer mounted in the probe. The output of the potentiometer is displayed on a Digitec No. 268 D.C. Millivoltmeter. The surface of the airfoil is found using the circuit in fig. 6. When the hot wire touches the airfoil, the circuit shorts out.

Velocity measurements were made with a hot wire system manufactured by Flow Corporation (now Gould Inc.). The system includes the hot wire, a 900-1 Constant Temperature anemometer whose output is fed into a 900-4A

Linearizer whose output is read from a 900-2D Digital Voltmeter. The wires were platinum, 0.0005 inches in diameter and about 0.01 inches long.

In general, the equipment was very reliable. There were some problems during the experimentation, to be described in the next chapter.

## CHAPTER II

PROCEDURE, PROBLEMS AND SOLUTIONS

In this chapter, inadaquacies in the procedure and equipment are identified. Also, some observations made during the experimentation are recorded here so that the next phase of the project will be less difficult.

The general procedure and a run schedule for the experiment appears in Table I. The first order of business was orienting the airfoil and sideboards. Yaw adjustments were made by aligning the sideboards with the wind tunnel centerline. The airfoil pitch was originally set to zero with a spirit level. Then the pressure distribution on the airfoil was measured and a 1 degree downwash was discovered. The airfoil was adjusted and the final symmetrical pressure distribution appears in fig. 9.

Pressure distributions on the airfoil for the remaining ellipse orientations were also measured. The only problem of note were fluctuating voltage readings caused by turbulence. Steady voltages were obtained with the aid of an RC circuit with a time constant of several seconds. The voltage readings were accurate to  $\pm .005$  volts.

The boundary layer traverses were the major data taking goal of this experiment. These measurements were complicated by two factors. A defective potentiometer in the linearizer caused the hot wire calibration to change every time the system was turned off. Secondly, the air temperature in the wind tunnel fluctuated. The Wright Brothers Wind Tunnel does not have a cooling system, so the equilibrium temperature at any speed depends on the outside temperature, wind speed and cloud cover.

The low speed runs (approximately 75 ft/sec.) usually came to an equilibrium temperature while the high speed runs (approximately 150 ft/sec.) often did not.

Due to these two factors, many hot wire calibrations were performed. In particular, the hot wire was recalibrated if the temperature changed more than 3 or 4 degrees centigrade. The calibration procedure was to raise the hot wire to a position where the wind speed relative to the free stream was known. The relationship was found by measuring with the hot wire the change in velocity between the top of the boundary layer and the calibration position. Knowing the potential velocity from the pressure distribution fixed the velocity at the calibration position.

As in the pressure measurements, turbulence caused the hot wire voltage to fluctuate. Again, an RC circuit was used to obtain a steady output. The readings were made to  $\pm .02$  volts.

The measurement of relative height in the boundary layer was quite accurate;  $\pm .0005$  volts. But the zero height could not be determined with certainty using the circuit previously described. Due to small vertical vibrations of the hot wire probe, probably caused by wind tunnel vibrations, the circuit would short out at some undetermined height above the airfoil. An alternate method of finding the zero height is described in the next chapter.

CHAPTER III  
REDUCING THE DATA

Data reduction was a very time consuming process. This was due to several deficiencies in the experiment which were identified as the data was reduced. These drawbacks and the data reduction process are described below.

Pressure coefficients were calculated using the following equations:

$$C_{p_{UPPER}} = \frac{(V - V_0)}{delh} 6.669^* \frac{\text{in of alcohol}}{\text{volt}} \quad (3.1)$$

$$C_{p_{LOWER}} = \frac{(V - V_0)}{delh} 9.097 \frac{\text{in of alcohol}}{\text{volt}} \quad (3.2)$$

where  $V_0$  is the pressure transducer voltage for zero pressure difference across the membrane and  $delh$  is the free stream dynamic pressure.  $delh$  measurements were made during each run as the temperature changed.\* The transducer constants were measured several times and were stable. The standard deviations of the pressure coefficients were determined to be (see appendix 2)  $SD_{upper} < .03$  and  $SD_{lower} < .05$

\* The specific gravity of the alcohol in the wind tunnel's manometer is given by:  $SG_{AL} = .812 - .0008 (T-60^{\circ}\text{F})$ . The ambient temperature during experimentation stayed between 50 and 80°F, usually near 60°F. By assuming  $SG_{AL} = .812$ , less than a 2% error in dynamic pressure is introduced. Therefore,  $SG_{ALC.} = .812$  was assumed during the data reduction. (See Appendix A)

Obtaining the boundary layer velocity profiles took by far the most time. Due to the bad potentiometer and the unstable temperatures, many hot wire calibrations had to be made. A typical set of curves appears in fig. 7. Since the graphs are nonlinear at low velocities hot wire readings were converted to velocities graphically. Furthermore, to maintain overall accuracy, if the temperature changed during a run  $3^{\circ}\text{C}$  or more that run was discarded. The reduced values are accurate to better than 3%.

Velocities were non-dimensionalized two ways. One method used the potential velocity,  $U_p$ , at the particular chord position. The second technique incorporated the friction velocity:  $u_\tau$  where

$$u_\tau = U_p \sqrt{c_f/2} \quad (3.3)$$

The friction velocity is equal to the square root of the Reynold's shear stress, ie.  $\sqrt{\rho u' v'}$ , in the lower part of the inner region of a turbulent boundary where the eddy (or Reynold's) stress is practically constant\* and equal to  $\tau_w$  [7].  $u/U_p$  is accurate to better than 3%. The accuracy of  $u/u_\tau$  depends on  $c_f$  which is determined below.

Heights in the boundary layer were calculated using

$$Y = (V - V_{zH}) 1.85 \text{ in/volt} = (V - V_o) 15424 \text{ ft/volt} \quad (3.4)$$

\* Assuming a constant eddy stress is a good approximation for flat plate profiles but not for flows subject to large adverse pressure gradients. (eq I.5).

where  $V_{zh}$  is the zero height voltage. As noted in the last chapter, the zero height voltage could not be determined during the experiment. The voltage used to reduce the data was found graphically by plotting (velocity vs. height in volts) the lower portion of each boundary layer profile and extrapolating the graph to zero velocity. The intercept point on the height axis was taken as zero height. It is estimated that the heights are correct to within .003 inches.

Heights were non-dimensionalized several ways. The momentum thickness, defined analytically by

$$\Theta = \int_0^{\delta} \left(1 - \frac{u}{U_p}\right) \frac{u}{U_p} dy \quad (3.5)$$

was one of the nondimensionalizing parameters. To calculate  $\Theta$ , the integral was approximated by the sum

$$\Theta = \sum_{i=1}^n \left(1 - \left(\frac{u}{U_p}\right)_i\right) \left(\frac{u}{U_p}\right)_i dely_i \quad (3.6)$$

where  $n$  is the number of points in the boundary layer profile up to the point where  $u = U_p$  and  $dely_i$  is given by

$$dely_i = \frac{y_{i+1} - y_{i-1}}{2} \quad (3.7)$$

Another parameter, which appears in the Log Law, was  $\gamma u_\tau$ .

By the definition of an equilibrium turbulent boundary layer, the third parameter, Clausers thickness,

$$\Delta = \int_0^\delta \frac{U_p - u}{u_\tau} dy = \delta \int_0^1 \frac{U_p - u}{u_\tau} d\left(\frac{y}{\delta}\right) \quad (3.8)$$

is always in constant ratio to  $\delta$ , unlike  $\theta$ . Therefore  $\Delta$  can be substituted for the indeterminate boundary layer height. Clauser's thickness was evaluated by first calculating the displacement thickness

$$\delta^* = \int_0^\delta \left(1 - \frac{u}{U_p}\right) dy \quad (3.9)$$

using the summing approximation described above. Then  $\Delta$  was found from

$$\Delta = \sqrt{2/c_f} \delta^* \quad (3.10)$$

$\delta^*$ , like  $\theta$ , is not in constant ratio with the boundary layer height in a turbulent boundary layer.  $\delta^*/\delta$  and  $\theta/\delta$  depend on  $c_f$  and hence Reynold's number [2].

Two more boundary layer characteristics which were calculated are

$$H = \delta^*/\theta \quad (3.11)$$

and

$$G = \frac{\int_0^1 \left(\frac{U_p - u}{u_\tau}\right)^2 d\left(\frac{y}{\delta}\right)}{\int_0^1 \left(\frac{U_p - u}{u_\tau}\right) d\left(\frac{y}{\delta}\right)} = \frac{1}{\Delta} \int_0^1 \left(\frac{U_p - u}{u_\tau}\right)^2 d\left(\frac{y}{\delta}\right) \quad (3.12)$$

$G$ , because it is independent of  $\delta$ , is a constant for a particular equilibrium boundary layer.

The skin friction coefficient, as noted in the introduction, was to be determined using Clausers' method. A small correction to the Law of the

wall had to be made first, however, to account for the effects of longitudinal streamline curvature. Such curvature, which causes extra rates of strain, can have large effects on the skin friction and turbulence structure [8].

For example, approximately a ten percent change in skin friction results from  $\delta/R = .01$ , where  $R$  is the radius of curvature. In the present experiment,  $\delta/R$  was between .002 and .01. Following Bradshaw[8], a corrected version of the Log-Law will be derived below.

In the inner region, or log region, of a turbulent boundary layer, turbulent energy production and dissipation are nearly equal. Expressed mathematically, this statement becomes

$$-\bar{u'v'} \frac{\partial u}{\partial y} \left( 1 + \alpha' \frac{e}{\partial u / \partial y} \right) \approx \frac{(-\bar{u'v'})^{3/2}}{\ell} \quad (3.13)$$

where  $e$  is the extra rate of strain and  $\alpha'$  is an empirical constant of 0 (10).  $e$  in the present experiment is  $-u/R$ . If the Reynold's shear stress is assumed constant and equal to  $\tau_w$ , ie.

$$-\bar{u'v'} = \tau_w / \rho \quad (3.14)$$

and if  $\ell = \kappa y$  where  $\kappa = .419$  as determined by Patel then 3.13 becomes

$$\frac{\partial u}{\partial y} = \frac{u \tau}{\kappa y} + \frac{\alpha'}{R} u \quad (3.15)$$

$$\frac{u}{u_\tau} = \frac{1}{K} \log_e (Y) + \frac{\alpha'}{R u_\tau} \int_0^Y u dy + C \quad (3.16)$$

It is sufficient to use the approximation  $u \propto y^{1/5}$  so that the remaining integral can be evaluated. The result is

(3.17)

$$\frac{u}{u_\tau} \left( 1 - \frac{5}{6} \frac{\alpha'}{R} Y \right) = \frac{1}{K} \log_e Y + C$$

Customarily assuming that  $u = 0$  at  $y = \delta^* / u_\tau$  leads to

$$\frac{u}{u_\tau} \left( 1 - \frac{5}{6} \frac{\alpha'}{R} Y \right) = A \log_{10} \left( \frac{Y u_\tau}{\delta^*} \right) + B \quad (3.18)$$

This equation becomes the Log Law for a flat plate when  $R = \infty$ .

For the mild convex curvature of an 0012 airfoil, Bradshaw suggests, subject to further experimentation, that  $\alpha' = 14$ . Subsequent to Bradshaw's paper, Meroney [9] reported on an experiment where convex curvature effects were studied with  $\delta^* / R = .01$ . Meroney measured skin friction with a Preston tube and the modified form of Clauser's chart presented above. Both techniques depend on a log region. With  $\alpha' = 14$ , he obtained good agreement. Based on the above evidence,  $\alpha' = 14$  was used to reduce the data of this experiment.

A modified Clauser chart and some plotted profiles from this experiment are presented in fig. 8A. For the profiles in mild pressure gradients, a log region is clearly present and  $c_f$  for that run is easily determined (e.g. Run 11). As  $p^*$  becomes larger, the log region shrinks in

extent and has vanished altogether when  $p^* = .104$  in Run 30. Even in larger pressure gradients, however, the profiles have a point of inflection for  $y u_\tau / v = y U_p \sqrt{c_f / 2} / v$  greater than about 30; the smallest value of the non-dimensional height for which the Log Law holds in a flat plate, zero pressure gradient profile [10]. The value of  $c_f$  at the point of inflection was taken as the local skin friction coefficient for runs subject to large pressure gradients. As noted in the introduction, the Log Law could be modified to include the case of large adverse pressure gradient. However, for this experiment neither the equipment nor the time was available to measure  $\tau / \tau_w$  and since boundary layer profiles must be measured at many  $x/c$  locations to numerically integrate I.5,  $\tau / \tau_w$  could not be calculated either. An alternate mixing length assumption was tried. In Sturek's paper [6], it is proposed that

$$\ell = C \delta \tanh \left( \frac{xy}{C \delta} \right) \quad (3.19)$$

where  $C = .09$ . Using this equation and assuming a constant shearing stress, the Law of the Wall becomes

$$\frac{u}{u_\tau} \left( 1 - \frac{5}{6} \frac{\alpha'}{R} y \right) = \frac{1}{K} \log_e \left( \frac{\sinh \left( \frac{xy}{C \delta} \right)}{\sinh \left( \frac{x \beta y}{C \delta u_\tau} \right)} \right) \quad (3.20)$$

Expanding  $\sinh$  in a Taylor's series and dropping terms of higher order than  $(\frac{xy}{C \delta})^3$  transforms 3.20 into

$$\frac{u}{u_\tau} \left( 1 - \frac{5}{6} \frac{\alpha'}{R} y \right) = \frac{1}{X} \log_e \left[ \frac{yu_\tau}{v} \left( 1 + \frac{1}{3!} \left( \frac{K}{C\delta} y \right)^2 \right) \right] - \frac{1}{X} \log_e \left[ \beta \left( 1 + \frac{1}{3!} \left( \frac{K\beta v}{C\delta u_\tau} y \right)^2 \right) \right]^{(3.21)} \quad 33$$

Unfortunately, this modification did not significantly improve the situation (see fig. 8B). The correction terms  $(\frac{1}{3!} (\frac{K}{C\delta} y)^2$  and  $\frac{1}{3!} (\frac{K\beta v}{C\delta u_\tau})^2$ ) are too small to correct for the effects of adverse pressure gradient.

After fruitlessly trying to modify the Law of the Wall, it was decided to use skin friction coefficients determined from the Clauser plots realizing that in the larger adverse pressure gradients, Clauser's technique would overpredict  $c_f$ . In addition, it was recognized that  $p^*$ , an important parameter for predicting  $c_f$  and analyzing a boundary layer, would also be in error (too small since  $p^* = \sqrt{\frac{dp}{dx}}/\rho (U_p \sqrt{c_f/2})^3$ ). This circular relationship between  $p^*$  and  $c_f$  is the key argument in favor of directly measuring the wall shear stress in later phases of this project.

Reducing the data was a straightforward but time consuming process which indicated that improvements be made to the zero height and skin friction determinations and to the procedure (see chapter 5).

CHAPTER IV  
DISCUSSION OF RESULTS

The outcome of this experiment could be described as encouraging and satisfying. The results are encouraging because the pressure data agrees with the findings of Phase 1 [1] and the boundary layer data is in accord with investigations performed over the last 30 years. The satisfaction is derived from fulfilling the goals of the experiment.

The pressure coefficient distributions about the airfoil for different ellipse orientations are presented in figs. 9-13.\* From these figures, values of  $U_p/U_\infty$  were calculated using the relation

$$\frac{U_p}{U_\infty} = \sqrt{1 - C_p} \quad (4.1)$$

$U_p/U_\infty$  at the two data taking positions, for each ellipse angle are catalogued in Table II. Noting the small differences in each figure and in the Table between low and high speed runs, it is apparent that Reynold's number effects are small.

From the  $C_p$  distributions,  $dc_p/dx$  was calculated for the two boundary layer measuring stations and the results are shown in fig. 14. The non-dimensional pressure gradient is more than twice as large at  $x/c = .9380$  than at the upstream position. Also  $dc_p/dx$  peaks at  $\alpha = 90^\circ$  at both data positions as would be expected from linear airfoil theory since both the effective angle of attack and effective camber of the equivalent cambered

\* RUN J was discarded due to equipment malfunction.

airfoil are maximized at this ellipse angle [ 11 ]. The two trends in  $dc_p/dx$  are clearly reflected in the boundary layer profiles to be discussed.

Conventional nondimensional plots of each boundary layer profile ie.  $u/U_p$  vs.  $y/\theta$  are presented in figs 15-32, and pertinent measured and calculated parameters for each profile appear in Tables IIIA-IIID. From the graphs and the Tables, each profile can be reconstructed dimensionally. A glance at each graph will show that the profiles are quite repeatable, helping to confirm the accuracy of the data taking equipment.

To further validate the results, the profiles in figs 15-32 should somehow be compared with theory and previous experiment. In reference [ 12 ], it is shown that if one assumes the Log-Law holds at  $y = \theta$  and the boundary layer velocity profile depends on  $y/\delta$  and  $H$  according to

$$\frac{u}{U_p} = \left( \frac{y}{\delta} \right)^{\frac{1}{2}(H-1)} \quad (4.2)$$

the following equation holds

$$\gamma = \frac{u_\theta}{U_p} = \left[ \frac{H-1}{(H+1)H} \right]^{\frac{1}{2}(H-1)} \quad (4.3)$$

In the same reference an empirical relation developed by Ludwieg and Tillman is presented

$$\gamma = 2.333 \times 10^{-0.398H} \quad (4.4)$$

These two relations and  $\gamma$  and  $H$  from the velocity profiles of this experiment are plotted in fig 33. There is scatter in the data, but agreement seems to be fair at low values of  $H$  and better at higher  $H$  values. The other data points on the graph are from Clausers' two equilibrium layers as presented in reference [ 13]. Considering the lack of agreement between the two equations for  $\gamma$  and the scatter in Clauser's data, the results from the present experiment appear reasonable.

The values of  $\theta$  used to normalize  $y$  can be found as noted in Table III and  $\theta$  vs ellipse angle  $\alpha$  is plotted in fig. 34. It is apparent in the figure that, except for the nearly separating flows of runs 20 and 30 (see page 37 ), the momentum thickness of the low and high speed runs at a given  $\alpha$  and  $x/c$  location, are nearly the same. At first thought,  $\theta$  should decrease with  $U_\infty$ , but the reason it does not is probably due to the fact that the point of transition to turbulence moves forward on an airfoil as  $U_\infty$  increases. In reference [ 14], Schlichting states as a rough guide that the point of instability for the Reynolds number in question ( $\frac{U_\infty c}{\nu} = 10^6$ ) is at  $c_p$  minimum for either surface of an airfoil. Further, he shows that the difference in  $Re = \frac{U_p \theta}{\nu}$  between the points of instability and transition decreases as

$$\frac{\theta^2}{\nu} \frac{dU_p}{dx} = - \frac{\theta^2}{\mu U_p} \frac{dp}{dx} = - \frac{1}{2} \frac{\theta^2}{\nu \sqrt{1 - c_p}} U_\infty \frac{dc_p}{dx} \quad (4.5)$$

becomes more negative. Qualitatively then, as  $U_\infty$  becomes larger the point of transition moves forward on the airfoil, enabling the boundary

layer to have a longer distance in which to grow.

To obtain an order of magnitude estimate of the phenomena, consider that on a flat plate  $\theta$  grows according to

$$\theta(x) = 0.972 \times Re_x^{-0.2} \quad [15] (4.6)$$

assuming  $U_2 = 2U_1$  and requiring  $\theta_2 = \theta_1$  leads to

$$x_2 = 1.19 x_1 \quad (4.7)$$

Letting  $x_1 = 10$  inches means that  $x_2 = 12$  inches. The point of transition only has to move 2 inches. Therefore it is reasonable that the boundary layer heights in question be the same.

The values of  $H = \delta^*/\theta$  that correspond to the profiles in figs. 15-32 are typical of turbulent boundary layers. Reference [16] states that for small pressure gradients  $H$  is about 1.4 while for separating flows,  $H$  rises rapidly to 1.8 to 2.6. This is just the range of  $H$  found in this experiment. In particular, runs 3 and 4 ( $x/c = .6875$ ,  $\alpha = 0^\circ$ ) with  $H = 1.44$  are examples of flows in mild adverse pressure gradients and runs 29 and 30 ( $x/c = .9380$ ,  $\alpha = 90^\circ$ ) with  $H = 1.86$  represent flows on the verge of separation.

In figs 35-44, the boundary layer data is replotted in modified Law of the Wall coordinates:  $\frac{u}{u_\tau} (1 - \frac{5}{6} \frac{\alpha'}{R} y)$  vs.  $\frac{yu_\tau}{v}$ . As long as  $p^*$  is less than about .02, a log region is distinguishable. For example, in fig 41, run 27 with  $p^* = .0182$  still posses a small log region but run 26 with

$p^* = .0262$  no longer obeys the log law (see also fig. 43). The extreme case is fig 41 where  $p^* = .104$  and clearly no log region exists. It is especially clear in this figure that a Clauser chart not developed using better shear stress and mixing assumptions will not predict  $c_f$  accurately. The resultant  $c_f$ 's will be too high in strong adverse pressure gradients.

The range of  $p^*$ 's encountered in this experiment was quite large. Values ranged from .0019 at the upstream data position with no ellipse and  $U_p = 157.9$  ft/sec to .104 at the downstream data position with  $\alpha = 90^\circ$  and  $U_p = 64.7$  ft/sec. For comparison purposes, in Clauser's first equilibrium layer  $p^*$  went from .0164 to .0077 and in his second layer,  $p^*$  varied from .063 to about .04. Of course for a flat plate,  $p^*$  equals zero and for a flow with zero skin friction,  $p^* = \infty$ . Before looking more closely at  $p^*$ , the skin friction coefficient will be investigated since these two parameters are interrelated.

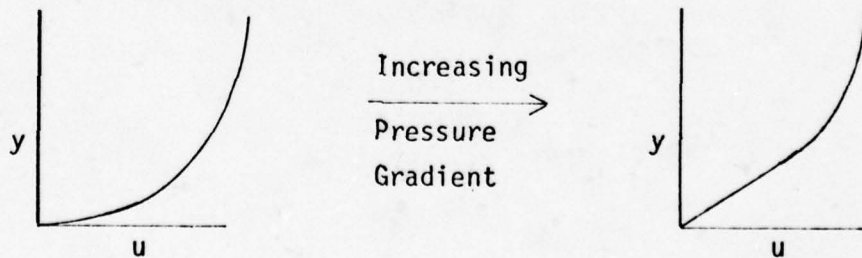
To check the accuracy of using Clauser plots to determine  $c_f$ , figure 45 presents the skin friction coefficients from this experiment plotted against the Ludwieg and Tillman empirical relation [17]

$$C_f = 0.246 \frac{Re_\theta^{-0.268} H^{-0.678}}{10} \quad (4.8)$$

with  $Re_\theta$  and  $H$  from the present experiment. In Ludwieg and Tillman's data base,  $Re_\theta$  went from  $10^3$  to  $4 \times 10^4$  and  $p^*$  varied from -.002 to .00575. The present data base includes:  $8.95 \times 10^2 \leq Re_\theta \leq 488 \times 10^3$  and  $.0019 \leq p^* \leq .1040$ . For the larger values of  $c_f$  (smaller values of  $p^*$ ), equation 4.8 and the present experiment are in good agreement with 4.8 slightly underpredicting

$c_f$ . For the smaller values of  $c_f$ , 4.18 overpredicts the present results as would be expected since the empirical correlation did not include the large values of  $p^*$  to which these  $c_f$ 's correspond. The best straight line fit, in the least squares sense, to the data points from the present experiment in fig. 45 would have a  $49^\circ$  slope instead of  $45^\circ$  and a "y" intercept of -.0005 instead of 0. Finally, several  $c_f$ 's from the same Clauser profiles that appeared in fig. 33 are shown here. The smallest value of  $p^*$  in Clauser's experiment was about .0077 which is higher than any values in Ludwieg's and Tillman's data base. Clauser's data and the empirical relation are in good agreement with some scatter. All in all, the  $c_f$  values from the present experiment look very reasonable.

The local skin friction coefficients are graphed vs.  $\alpha$  in fig. 46. In the figure,  $c_f$  is seen to decrease as the flow proceeds downstream and as  $\alpha$  increases up to  $\alpha = 90^\circ$ . One would expect such trends since, as already shown,  $dc_p/dx$  increases with respect to the above position and angle changes. In adverse pressure gradients (positive  $dc_p/dx$ ), boundary layer profiles are less full and  $H$  is larger (see below, compare figs 20, 27 and 27, 31 and compare values of  $p^*$  and  $H$  in Tables III) which causes  $du/dy$  wall to be smaller.



Since  $\mu \frac{du}{dy} = \tau_w$  and  $\tau_w \propto c_f$ ,  $c_f$  will be diminished in adverse pressure gradients.

Also evident in fig. 46 is an inverse relationship between  $c_f$  and  $Re_\theta$  and a tendency for this relationship to be more sensitive at  $x/c = .6875$  than at  $x/c = .9380$ . Writing the local skin friction coefficient as

$$C_f = \frac{\tau_w}{\frac{1}{2} \rho U_p^2} = \frac{\mu \frac{du}{dy} \text{WALL}}{\frac{1}{2} \rho U_p^2} \quad (4.9)$$

and using  $U_p/\theta$  as a rough approximation to  $\frac{du}{dy} \text{WALL}$  leads to

$$C_f \approx \frac{2 \nu}{U_p \theta} = \frac{2}{Re_\theta} \quad (4.10)$$

Equation 4.8 also shows that  $Re_\theta$  and  $c_f$  are inversely proportional.  $U_p$  was approximately doubled between low and high speed runs while  $\theta$  remained relatively unchanged (fig. 34). Therefore,  $c_f$  should decline\* with velocity and  $Re_\theta$ ; just the behaviour exhibited in fig. 46.

The reason for the greater sensitivity of  $c_f$  to  $Re_\theta$  changes at  $x/c = .6875$  can be traced to  $H$  using eq. 4.8 rewritten as the ratio

$$\frac{C_{f_{HS}}}{C_{f_{LS}}} = \left( \frac{Re_{\theta_{LS}}}{Re_{\theta_{HS}}} \right)^{0.268} / 10^{-0.678 (H_{LS} - H_{HS})} \quad (4.11)$$

\* The exception at  $\alpha = 90^\circ$ ,  $x/c = .9380$  is explained in the following discussion.

where HS stands for "high speed" and LS means "low speed". In general,  $H$  is relatively constant between low and high speed runs at  $x/c = .6875$  while at  $x/c = .9380$   $H$  varies quite a bit more.\* For example, the chart below is for  $\alpha = 45^\circ$

$\frac{x}{c}$	$U$	$Re_\theta$	$H$	$c_f$
.6875	73.2	13.8	1.43	.00365
.6875	147.6	26.6	1.43	.00298
.9380	75.1	22.7	1.62	.00235
.9380	148.1	48.8	1.54	.00200

At  $x/c = .6875$ ,  $H$  does not change at all with velocity, so  $c_{fHS}/c_{fLS}$  depends only on  $Re_\theta$ . At  $x/c = .9380$ ,  $H_{LS} > H_{HS}$  and the  $Re_\theta$  term of 4.11 is multiplied by a number greater than one, increasing  $c_{fHS}/c_{fLS}$ . Combining equation 4.11 and the values of  $Re_\theta$ ,  $H$  and  $c_f$  at  $\alpha = 45^\circ$  yields

$\frac{x}{c}$	$\frac{c_{fHS}}{c_{fLS}} \text{ from 4.11}$	$\frac{c_{fHS}}{c_{fLS}} \text{ from Clauser chart}$
.6875	.83	.82
.9380	.95	.85

The absolute values do not agree but the trend is correct. Therefore,  $c_f$  is more (less) sensitive to  $Re_\theta$  changes at the upstream (downstream) data station because  $H$  is not influenced (influenced) by these changes in  $Re_\theta$  due to the mild (not so mild) pressure gradient.\*\*

\* From previous discussion,  $H$  changes more rapidly in larger pressure gradients. In this experiment, larger can be interpreted as downstream

\*\*This also explains why at  $x/c = .9380$  and  $\alpha = 90^\circ$ , the low speed  $c_f$  is smaller than the high speed value. Doubling  $Re$  caused  $H$  to decrease from 1.87 to 1.65, a large change. From equation 4.11,  $c_{fHS}/c_{fLS} = 1.3$ . The ratio of  $c_f$ 's from Clauser's chart is  $c_{fHS}/c_{fLS} = 1.3$ .

Fig. 47 also exhibits  $p^*$ 's dependence on  $Re_{\theta}$  and  $H$  through  $c_f$ . To see how, equation 4.12 will be written as a ratio using equation 4.1 to eliminate  $U_p$ .

$$\frac{P_{LS}^*}{P_{HS}^*} = \frac{U_{\infty HS}}{U_{\infty LS}} \left( \frac{c_{f_{HS}}}{c_{f_{LS}}} \right)^{3/2} \quad (4.12)$$

$U_{\infty HS}/U_{\infty LS}$  is always about 2 and  $c_{f_{HS}}/c_{f_{LS}}$  from previous discussion is a larger number at  $x/c = .9830$  than at  $x/c = .6875$ . Therefore  $P_{LS}^*/P_{HS}^*$  should be greater at the downstream position, which is the case. For example, at  $\alpha = 45^\circ$ ,  $P_{LS}^*/P_{HS}^*|_{.9380} = 1.5$  and  $P_{LS}^*/P_{HS}^*|_{.6875} = 1.4$  and for  $\alpha = 135^\circ$   $P_{LS}^*/P_{HS}^*|_{.9380} = 1.7$  and  $P_{LS}^*/P_{HS}^*|_{.6875} = 1.1$

To show  $p^*$ 's dependence on  $Re_{\theta}$  and  $H$ , 4.12 can be rewritten using 4.11 which leads to

$$\frac{P_{LS}^*}{P_{HS}^*} = \frac{U_{\infty HS}}{U_{\infty LS}} \left( \frac{Re_{\theta LS}}{Re_{\theta HS}} \right)^{0.402} 10^{1.017(H_{LS} - H_{HS})} \quad (4.13)$$

$H$  decreases with velocity in the larger adverse pressure gradients at the downstream data position which makes  $P_{LS}^*/P_{HS}^*$  larger. Using values of  $U_{\infty}$ ,  $Re_{\theta}$  and  $H$  for  $\alpha = 45^\circ$  and  $135^\circ$  from Table 3 in equation 4.12 gives the following results.

$\alpha$	$\frac{x}{c}$	$\frac{P_{LS}^*}{P_{HS}^*}$ eq. 4.12	$\frac{P_{LS}^*}{P_{HS}^*}$ fig. 47
$45^\circ$	.6875	1.6	1.4
$45^\circ$	.9380	1.8	1.5
$135^\circ$	.6875	1.1	1.1
$135^\circ$	.9380	1.8	1.7

The agreement is good.

Note that the discussion has made a circle.  $H$  affects  $c_f$  which affects the nondimensional pressure gradient which influences  $H$ . The ratio of displacement and momentum thicknesses,  $H$ , can be calculated from boundary layer velocity profiles. To calculate  $p^*$  accurately,  $c_f$  must be accurately determined which is not possible in large adverse pressure gradients (large  $p^*$ ) using a Clauser chart. Therefore, it would be advantageous to directly measure  $c_f$ .

Velocity defect plots,  $(U_p - u)/u$  vs  $Y/\Delta$ , are presented in figs. 48-66. The defect plot of fig. 66 is not from this experiment but is the Outer Law for the turbulent boundary layer on a flat plate as measured in Phase I.  $\Delta$  is used in place of  $\delta$  in these graphs because  $\Delta/\delta$  is a constant for any equilibrium layer and  $\Delta$  is more accurately known. Each graph shows the boundary layer profiles at the upstream and downstream data positions for the same values of  $\alpha$  and for roughly the same free stream velocity. None of these figures contain similar or equilibrium profiles. This deduction could also be made by noting in Tables III that the values of  $G$  and  $\Delta/\delta$  for each pair of flows, as presented in figs. 47-64, are different.  $G$  and  $\Delta/\delta$  at each streamwise station of an equilibrium layer are the same. The zero velocity point,  $U_p/u_\tau$ , is listed in each figure because it is often so large it could not be plotted.

To show the relationship between equilibrium layers, Clauser [2] made a graph of  $\Delta/\delta$  vs.  $G$ . This graph, including the data points from the present experiment, appears in fig 67\*. There is scatter in the data due

\* To obtain more consistent values of  $\delta$ , the height at which  $u = .99 U_p$  was used to plot the data from this experiment.

in part to the uncertainty in determining  $\delta$  but it is clear that a wide range of dissimilar profiles were produced in this experiment.

The results of this experiment are in agreement with past studies in terms of measured pressure distributions and boundary layer developments. Several important trends germane to future work have been identified and the accuracy of the data taking equipment has been verified.

## CHAPTER V

CONCLUSIONS AND RECOMMENDATIONS

The following conclusions can be drawn from the present study:

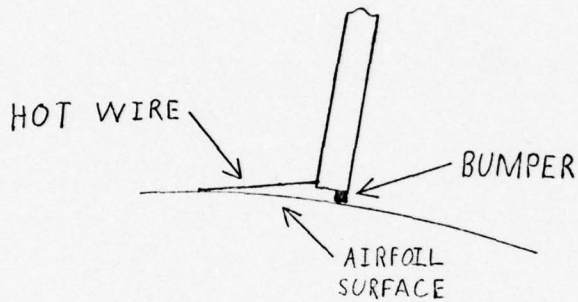
1. The boundary layer probe was successful in meeting its design requirements.
2. The boundary layer over the airfoil for different ellipse orientations and wind speeds was measured and the results are consistent with previous investigations.
3. Clauser plots can be used to determine the skin friction coefficient as long as  $p^*$  is less than about .02.
4. Clauser plots are inaccurate in determining  $c_f$  for some values of  $p^*$  encountered in this experiment. The worst case occurs at low speeds when  $\alpha = 90^\circ$ .
5. Problems in the experiments design and procedure have been identified. In particular, the zero height system is inadequate and the procedure should be modified to eliminate tempurature changes during runs.

The following recommendations are made in regard to future work:

1. Based on the confidence gained in the experiment's design during this study, it is recommended that the dynamic measurements be made.
2. Develop an alternate method, preferably independent of  $p^*$ , for determining the local skin friction coefficient. Two possibilities are:
  - A. Measure  $\tau_w$  directly (this is the best alternative)
  - B. Measure  $\tau_w$  using a skin friction fence. In the laminar sub-

layer, flow accelerations are small so  $\tau_w$  will only depend on  $p^*$  and  $y u_\tau / v$ .  $u_\tau$  for the first iteration can be measured with Clauser plots.

- Redesign the zero height system to eliminate probe vibrations close to the wind. Perhaps a rubber bumper at the bottom of the probe would be effective.



- Determine the point of laminar to turbulent transition through calculation or measurement.
- Design the procedure for the dynamic measurements so that the wind speed remains constant for an extended period of time to allow the air to come to an equilibrium temperature. A technique developed by Mangelsdorf [19] can be used to estimate the equilibrium temperature.

If one assumes that

$$T(t) = A + B e^{-kt} \quad (5.1)$$

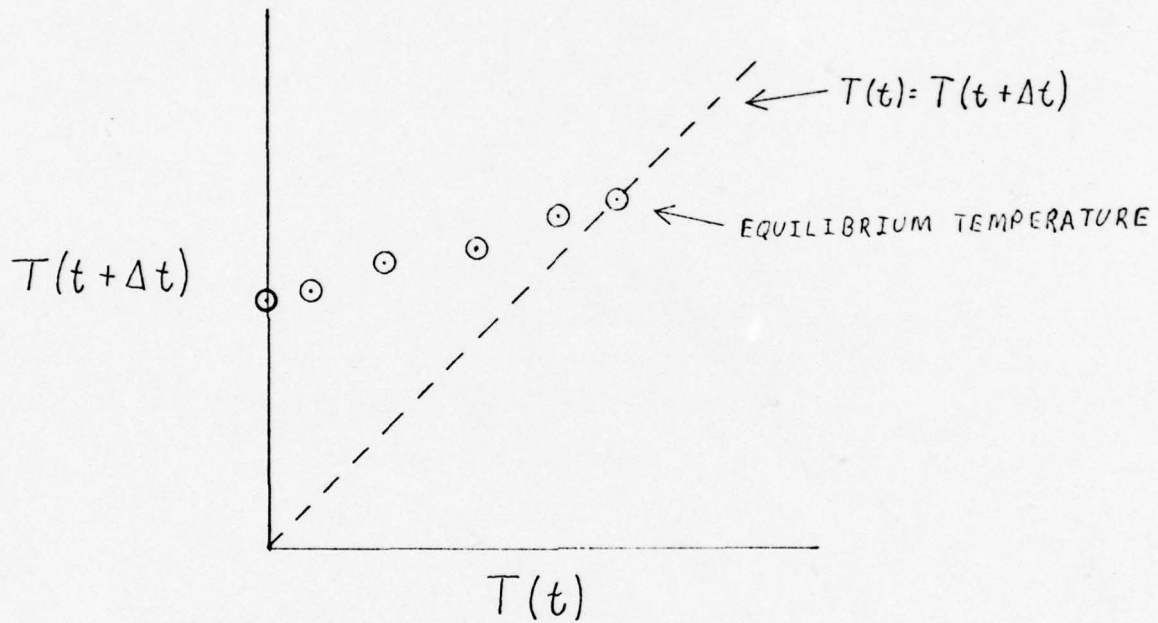
where A, B and k are constants and the temperature T depends on time (t) then the temperature at  $t + \Delta t$  is

$$T(t + \Delta t) = A + B e^{-k(t + \Delta t)} \quad (5.2)$$

or

$$T(t + \Delta t) = A(1 - e^{-k\Delta t}) + T(t) e^{-k\Delta t} \quad (5.3)$$

(5.3 was obtained by combining 5.1 and 5.2.) Measuring  $T$  at time intervals of  $\Delta t$  and then plotting  $T(t+\Delta t)$  vs.  $T(t)$  will result in a straight line which will intercept the line  $T(t) = T(t+\Delta t)$  at approximately the equilibrium temperature (see below).



When analyzing data, one must have at least an order of magnitude estimate of the experimental error. To obtain such an estimate, the errors in the present experiment were propagated in the rather simple but useful way described by example below.

Reference (19) presents the following equation for calculating the square of the standard deviation (ie the variance) of the mean of a function  $Q = Q(a, b, c,)$ :

$$(SD_Q)^2 = \left(\frac{\partial Q}{\partial a}\right)^2 (SD_{ma})^2 + \left(\frac{\partial Q}{\partial b}\right)^2 (SD_{mb})^2 + \left(\frac{\partial Q}{\partial c}\right)^2 (SD_{mc})^2 \quad (A.1)$$

where  $ma$  etc. stands for the mean of the variance of "a" and a normal error distribution has been assumed. The first example will use this equation to calculate the standard deviation in the pressure coefficient:  $c_p = (V-V_o) C/delh$ , where  $C$  is the transducer constant. From eq A.1.1

$$(SD_{c_p})^2 = \left(\frac{C(V-V_o)}{delh^2}\right)^2 (SD_{delh})^2 + \left(\frac{C}{delh}\right)^2 (SD_V)^2 + \left(\frac{C}{delh}\right)^2 (SD_{V_o})^2 + \left(\frac{V-V_o}{delh}\right)^2 (SD_C)^2 \quad (A.2)$$

Assuming the following values for the worst case:  $C=9.097$  in of al./volt,  $V-V_o=.2$  volts,  $delh=1.5$  in of al.,  $SD_{delh}=.03$  in of al  $SD_V=SD_{V_o}=.005$  volts and  $SD_C \approx 0$ . leads to  $SD_{c_p}=.049$ . For the best case:  $C=6.669$ ,  $V-V_o=.5$ ,  $delh=6.0$ ,  $SD_{delh}=SD_V=SD_{V_o}=.005$  and  $SD_{c_p}=.008$

49

For a second example, the standard deviation in  $U_\infty$  will be calculated

$$U_\infty = \sqrt{2q_\infty/\rho} \quad (A.3)$$

$$(SD_{U_\infty})^2 = \frac{1}{2\rho q_\infty} (SD_{q_\infty})^2 \quad (A.4)$$

The typical error is ( $\rho = 0.00234 \text{ slugs/ft}^3$ ,  $q_\infty = 6.01 \text{ lb/ft}^2$ ,  $SD_{q_\infty} = 0.12 \text{ lb/ft}^2$  ( $= 0.02 q_\infty$ , see p. 26)),  $SD_{U_\infty} = 72 \text{ ft/sec}$  or 1% of the velocity. The error is the same at all velocities because  $SD_{q_\infty}/q_\infty$  is in constant ratio.

Using the standard deviations in  $c_p$  and  $U_\infty$ ,  $SD_{U_p}$  can now be evaluated from  $U_p = U_\infty \sqrt{1 - c_p}$

$$(SD_{U_p})^2 = (1 - c_p)(SD_{U_\infty})^2 + \frac{U_\infty^2}{4(1 - c_p)} (SD_{c_p})^2 \quad (A.5)$$

Using  $SD_{c_p} = 0.049$ ,  $SD_{U_\infty} = 0.10$ ,  $c_p = 0.25$  (largest value of  $c_p$  at either data station) and  $U_\infty = 75$  gives  $SD_{U_p} = 2.1 \text{ ft/sec}$ . This is the worst case. The least error occurs at high speeds. Letting  $U_\infty = 150$ ,  $c_p \approx 0$  and  $SD_{c_p} = 0.008$ , leads to  $SD_{U_p} = 0.60 \text{ ft/sec}$ .

As a final example, the standard deviation in  $u/U_p$  will be found.

$$(SD_{u/U_p})^2 = \left(\frac{1}{U_p}\right)^2 (SD_u)^2 + \left(\frac{U}{U_p^2}\right)^2 (SD_{U_p})^2 \quad (A.6)$$

It will be assumed there is a 3% error in  $u$ . The smallest velocity measured in the boundary layer was about 20 ft/sec at  $U_p = 75 \text{ ft/sec}$

With  $SD_{U_p} = 2.1$ ,  $SD_u/U_p = .01$ . At the edge of the boundary layer,  $SDu/U_p$  is always about .03 because of the assumption above for  $u$ .

In using  $u/U_p$  to calculate the displacement, momentum and Clauser thicknesses, one must remove all systematic errors in  $u/U_p$  or these errors will add in the summation used to calculate  $\delta^*$ ,  $\theta$  and  $\Delta$ . Therefore if  $u/U_p$  was within 3% of unity at  $y = \delta$ , the whole profile was multiplied by a constant so  $u/U_p$  would equal 1.

## CALCULATING COORDINATES OF PROBE MOUNTING HOLES

## FOR GIVEN AXIAL MEASURING STATION

To make a boundary layer traverse or measure the angle of attack at a particular axial position, the location of the probe's mounting holes in the sideboards must be calculated. The pertinent equations are presented below.

$$h_t = 12(0.29690\sqrt{x} - 0.1260x - 0.35160x^2 + 0.28430x^3 - 0.10150x^4) \quad (B.1)$$

$$\frac{dh_t}{dx} = 12(0.14845x^{-\frac{1}{2}} - 0.12600 - 0.70320x - 0.85290x^2 - 0.40600x^3) \quad (B.2)$$

$$\eta = \tan^{-1}\left(\frac{dh_t}{dx}\right) \quad (B.3)$$

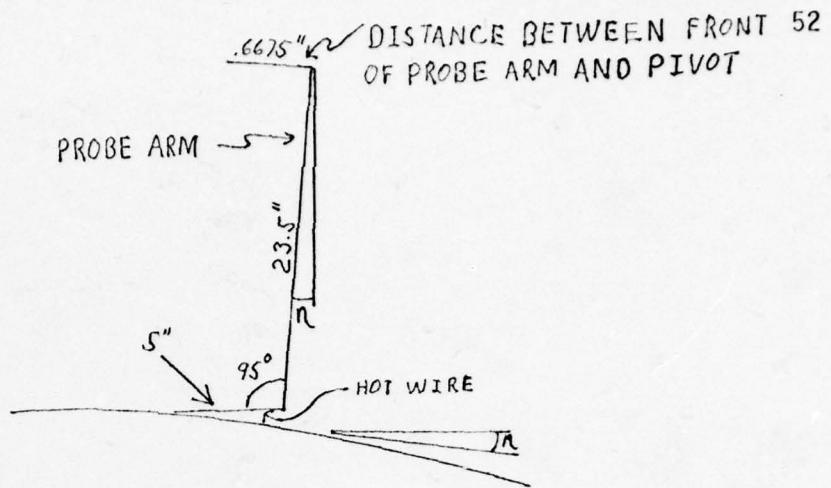
Where  $h_t$  is one-half the thickness of the airfoil in inches,  $\eta$  is the airfoils slope in degrees and  $x$  is inches along the chord from the leading edge. B.1 was taken from ref. (1).

## Boundary Layer Measurements

$$x_m = 20x/c + 5\cos(\lvert\eta\rvert - 5^\circ) + 23.5\sin\lvert\eta\rvert - .6675\cos\lvert\eta\rvert \quad (B.4)$$

$$h_m = 20h_t - 5\sin(\lvert\eta\rvert - 5^\circ) + 23.5\cos\lvert\eta\rvert + .6675\sin\lvert\eta\rvert \quad (B.5)$$

$x_m$  and  $h_m$  in inches.

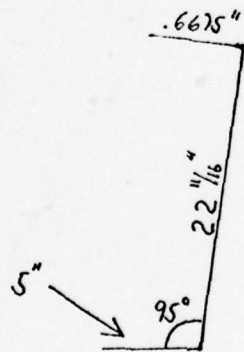


#### Angle of Attack Measurements

$$\alpha_m = 20 \alpha/c + 6.31 \quad (B.6)$$

$$h_m = 22.66 \quad (B.7)$$

$x_m$  and  $h_m$  in inches.



1. Kanevsky, A.R., "Comparison of the Pressure Distribution for Circulation Generated by Angle of Attack with that Generated by Trailing Edge Perturbation", Master of Science thesis at the Massachusetts Institute of Technology, February, 1978.
2. Clauser, F.H., "Turbulent Boundary Layers in Adverse Pressure Gradients", Journal of the Aeronautical Sciences, Vol.21, No.2, pp. 91-108, Feb.1954.
3. Duncan, W.J., Thom, A.S. and Young,A.D., Mechanics of Fluids 2nd ed., American Elsevier Publishing Co., Inc., New York, 1970. p.306.
4. Patel, V.C., "Calibration of the Preston Tube and Limitations on its Use in Pressure Gradients", J.Fluid Mech., Vol.23, Sept.,1965, pp. 185-208.
5. Galbraith, R.A.McD, Sjolander S., and Head, M.R., "Mixing Length in the Wall Region of a Turbulent Boundary Layer", Aero. Quat., Vol.28, Part 2, May 1977, pp.97-110.
6. Sturek, W.B., Dwyer, H.A., Kayser, L.D., Nietubicz, C.J., Reklis, R.P., Opalka, K.O., "Computations of Magnus Effects for a Yard, Spinning Body or Revolution", AIAA Journal, Vol. 16, No. 7, July, 1978, p 687-692.
7. Duncan, op.cit., p.301.
8. Bradshaw, P., "Effects of Streamline Curvature on Turbulent Flow", AGARDograph NO. 169. Aug. 1973.
9. Meroney, R.N., "Measurements of Turbulent Boundary Layer Growth Over a Longitudinally Curved Surface", Project THEMIS, Tech.Re No. 25, Fluid Mechanics and Diffusion Lab., Colorado State University, Jan. 1974.
10. Duncan, op.cit., p.306.
11. Kanevsky, op.cit., p.73.
12. Duncan, op.cit., p.340.
13. Proceedings: Computation of Turbulent Boundary Layers- 1968, Coles, D.E. and Hirst, E.A. Editors, Thermosciences Division, Department of Mechanical Engineering, Stanford University, Stanford, Ca. Vol. 2, pp.198-221.
14. Schlichting,H., Boundary Layer Theory, McGraw Hill Inc., 6th Edition, 1968, pp.479-483.

15. Duncan, op.cit., p.318.
16. Ibid, pp.334, 337.
17. Ibid, p.344.
18. Abbott, I.A. and von Doenfsoff, A., Theory of Wing Sections, McGraw Hill Book Co., Inc., 1949, p.321.
19. Young, H.D., Statistical Treatment of Experimental Data, McGraw Hill Inc. 1962.

TABLE I PROCEDURE AND RUN SCHEDULE

This listing summarizes how the data was taken. All measurements were made at two wind speeds and the boundary layer measurements were made twice at each wind speed. High speed data was taken at about  $q_{\infty} = 25.211 \text{ lb/ft}^2$  or  $U_{\infty} = 146.7 \text{ ft/sec}$  (100 mph). Low speed data was taken at about  $q = 6.311 \text{ lb/ft}^2$  or  $U = 73.3 \text{ ft/sec}$  (50 mph). The exact values of  $q_{\infty}$  and  $U_{\infty}$  appear in tables II and III. Several runs are missing due to equipment malfunction or wind tunnel air temperature changes of 3 degrees centigrade or more.

## STATIC PRESSURE DISTRIBUTION MEASUREMENTS

RUN	DATE(1978)	SPEED	$\alpha$ (DEGREES)
A	5/16	LOW	NO
B	5/16	HIGH	NO
C	5/18	LOW	0
D	5/18	HIGH	0
E	5/20	LOW	45
F	5/20	HIGH	45
G	5/26	LOW	90
I	5/26	HIGH	135
J	5/26	LOW	135

## BOUNDARY LAYER VELOCITY PROFILE MEASUREMENTS

56

RUN	DATE(1978)	SPEED	x/c	$\alpha$ (DEGREES)
2	5/16	HIGH	.6875	NO
3	5/16	LOW	.6875	NO
4	5/17	LOW	.6875	NO
7	5/18	LOW	.6875	0
8	5/18	LOW	.6875	0
9	5/18	LOW	.6875	45
10	5/18	LOW	.6875	45
11	5/18	HIGH	.6875	45
12	5/18	HIGH	.6875	45
13	5/20	LOW	.6875	90
14	5/22	LOW	.6875	90
17	5/23	LOW	.6875	135
18	5/23	LOW	.6875	135
20	5/23	HIGH	.6875	135
21	5/24	LOW	.9380	0
22	5/24	LOW	.9380	0
24	5/24	HIGH	.9380	0
25	5/25	LOW	.9380	45
26	5/25	LOW	.9380	45
27	5/25	HIGH	.9380	45
28	5/25	HIGH	.9380	45
29	5/25	LOW	.9380	90
30	5/25	LOW	.9380	90
32	5/25	HIGH	.9380	90
33	5/25	HIGH	.9380	135
34	5/25	HIGH	.9380	135
35	5/25	LOW	.9380	135
36	5/25	LOW	.9380	135
37	5/26	LOW	.9380	NO
38	5/26	LOW	.9380	NO
39	5/26	HIGH	.9380	NO

BOUNDARY LAYER VELOCITY PROFILE MEASUREMENTS  
CONTINUED

57

RUN	DATE(1978)	SPEED	x/c	$\alpha$ (DEGREES)
-----	------------	-------	-----	--------------------

40	5/26	HIGH	.9380	NO
----	------	------	-------	----

RUN	$q_\infty$ LB/FT <sup>2</sup>	$\alpha$ DEGREES	$U / U_p$	
			x/c = .6875	x/c = .9380
A	6.84	NO	1.065	.974
B	25.55	NO	1.067	.976
C	6.37	0	1.080	.990
D	25.38	0	1.087	.999
E	6.37	45	1.093	.981
F	26.07	45	1.097	.984
G	6.39	90	1.032	.872
I	26.20	135	1.060	.935
J	6.20	135	1.053	.932

TABLE II THE RATIO OF POTENTIAL VELOCITY  
 AT THE AIRFOIL SURFACE TO FREE STREAM  
 VELOCITY AS A FUNCTION OF ELLIPSE ANGLE  
 FOR THE BOUNDARY LAYER MEASURING STATIONS

RUN	$x/c$	$\alpha$	$\rho$	$U_\infty$	$U_p$	$u_\tau$	$\theta$	$\Delta$	$\nu$
		DEGREES	LB-SEC FT <sup>4</sup>	FT/SEC $\times 10^{-3}$	FT/SEC	FT/SEC	FT $\times 10^{-3}$	FT $\times 10^{-3}$	FT <sup>2</sup> /SEC $\times 10^{-6}$
2	.6875	NO	2.38	148.0	157.9	6.37	1.99	72.5	154
3	.6875	NO	2.39	73.5	78.3	3.63	1.96	60.7	155
4	.6875	NO	2.39	74.7	79.5	3.77	1.74	52.6	155
7	.6875	0	2.41	73.6	79.5	3.79	1.83	52.6	152
8	.6875	0	2.41	73.2	79.1	3.77	1.85	52.8	152
9	.6875	45	2.41	73.2	80.0	3.42	2.63	88.3	152
10	.6875	45	2.41	73.2	80.0	3.48	2.60	85.8	152
11	.6875	45	2.37	147.6	161.3	6.23	2.59	96.0	157
12	.6875	45	2.35	147.5	161.2	6.12	2.65	102.9	158
13	.6875	90	2.27	74.9	79.0	3.25	3.13	113.5	166
14	.6875	90	2.27	78.6	81.1	3.47	3.07	107.9	169
17	.6875	135	2.23	75.7	80.2	3.69	2.30	74.3	178
18	.6875	135	2.22	75.8	80.3	3.69	2.24	72.4	178
20	.6875	135	2.15	153.4	162.6	6.25	2.33	98.5	189

TABLE III A CHARACTERISTIC BOUNDARY LAYER PARAMETERS AND  
DIMENSIONALIZING DATA

RUN#	x/c	$C_f$	P*	$\delta^*$	H	G	$Re_\theta$	$\gamma$	$\Delta/\delta$
		DEG- REES		FT $\times 10^{-3}$			$\times 10^2$		
2	.6875	NO	.00325	.0019	2.92	1.47	7.91	20.4	.652
3	.6875	NO	.00430	.0025	2.81	1.44	6.54	9.9	.674
4	.6875	NO	.00450	.0023	2.50	1.44	6.40	8.9	.679
7	.6875	0	.00455	.0021	2.51	1.37	5.64	9.5	.696
8	.6875	0	.00455	.0021	2.52	1.39	5.57	9.6	.706
9	.6875	45	.00365	.0036	3.77	1.43	7.08	13.8	.651
10	.6875	45	.00378	.0034	3.73	1.43	6.94	13.7	.658
11	.6875	45	.00298	.0025	3.70	1.43	7.83	26.6	.639
12	.6875	45	.00288	.0027	3.91	1.47	8.44	27.0	.632
13	.6875	90	.00338	.0073	4.66	1.49	8.01	14.9	.625
14	.6875	90	.00350	.0072	4.51	1.47	7.67	14.7	.643
17	.6875	135	.00423	.0037	3.42	1.48	7.09	10.3	.665
18	.6875	135	.00423	.0037	3.33	1.48	7.09	10.1	.666
20	.6875	135	.00295	.0033	3.78	1.63	10.02	20.1	.606

TABLE III B CHARACTERISTIC BOUNDARY LAYER PARAMETERS AND  
DIMENSIONALIZING DATA

RUN#	x/c	$\alpha$	$\rho$	$U_\infty$	$U_p$	$u_\tau$	$\theta$	$\Delta$	$v$	
									DEGREES	$\frac{\text{LB-SEC}}{\text{FT}^4}$
					$\times 10^{-3}$				$\times 10^{-3}$	$\times 10^{-3}$
										$\times 10^{-6}$
21	.9380	0	2.30	74.2	74.1	3.00	3.71	136		167
22	.9380	0	2.30	74.2	74.1	3.03	3.74	135		167
24	.9380	0	2.32	147.6	147.5	4.89	3.72	176		163
25	.9380	45	2.33	75.1	73.9	2.53	4.93	233		161
26	.9380	45	2.33	75.1	73.9	2.58	5.05	231		161
27	.9380	45	2.31	148.1	145.7	4.71	5.50	267		164
28	.9380	45	2.30	148.1	145.7	4.49	5.25	269		164
29	.9380	90	2.34	74.2	64.7	1.69	6.63	474		160
30	.9380	90	2.34	74.2	64.7	1.69	6.54	448		160
32	.9380	90	2.29	149.8	130.6	3.92	4.74	261		166
33	.9380	135	2.29	150.6	140.8	4.51	4.99	242		166
34	.9380	135	2.28	150.5	140.7	4.45	5.02	247		168
35	.9380	135	2.31	74.5	69.7	2.41	4.67	221		167
36	.9380	135	2.33	74.5	69.7	2.41	4.54	213		166
37	.9380	NO	2.33	74.4	72.4	3.05	2.90	104		164
38	.9380	NO	2.33	74.4	72.4	3.05	2.82	101		164
39	.9380	NO	2.30	150.3	146.4	5.28	3.23	143		168
40	.9380	NO	2.29	150.3	146.4	5.18	3.28	144		169

TABLE III C CHARACTERISTIC BOUNDARY LAYER PARAMETERS AND  
DIMENSIONALIZING DATA

RUN#	x/c	$\alpha$	$C_f$	P*	$\delta^*$	H	G	$Re_0$	$\gamma$	$\Delta/\delta$
		DEG- REES			FT $\times 10^{-3}$			$\times 10^2$		
21	.9380	0	.00335	.0129	5.55	1.50	8.11	16.5	.631	4.4
22	.9380	0	.00335	.0129	5.53	1.48	7.90	16.6	.630	3.8
24	.9380	0	.00220	.0119	5.85	1.57	10.96	33.6	.589	6.6
25	.9380	45	.00235	.0277	7.98	1.62	11.14	22.7	.565	6.0
26	.9380	45	.00243	.0262	8.05	1.59	10.70	23.3	.582	6.0
27	.9380	45	.00200	.0182	8.46	1.54	11.07	48.8	.579	4.5
28	.9380	45	.00190	.0197	8.31	1.58	11.94	46.6	.571	5.8
29	.9380	90	.00136	.1040	12.36	1.86	17.78	26.9	.455	12.2
30	.9380	90	.00136	.1040	12.27	1.88	17.07	26.5	.458	11.3
32	.9380	90	.00180	.0352	7.83	1.65	13.73	37.3	.547	9.0
33	.9380	135	.00205	.0210	7.75	1.55	11.13	42.3	.578	6.7
34	.9380	135	.00200	.0220	7.80	1.55	11.26	42.2	.576	5.4
35	.9380	135	.00240	.0374	7.66	1.64	11.27	19.5	.549	7.0
36	.9380	135	.00240	.0373	7.37	1.62	11.06	19.1	.557	6.8
37	.9380	NO	.00355	.0124	4.37	1.51	7.99	12.8	.624	4.7
38	.9380	NO	.00355	.0124	4.25	1.51	7.98	12.5	.627	4.7
39	.9380	NO	.00260	.0101	5.10	1.58	10.26	28.1	.606	6.4
40	.9380	NO	.00250	.0108	5.10	1.55	10.09	28.3	.601	6.4

TABLE III D CHARACTERISTIC BOUNDARY LAYER PARAMETERS AND  
DIMENSIONALIZING DATA

## FIGURES

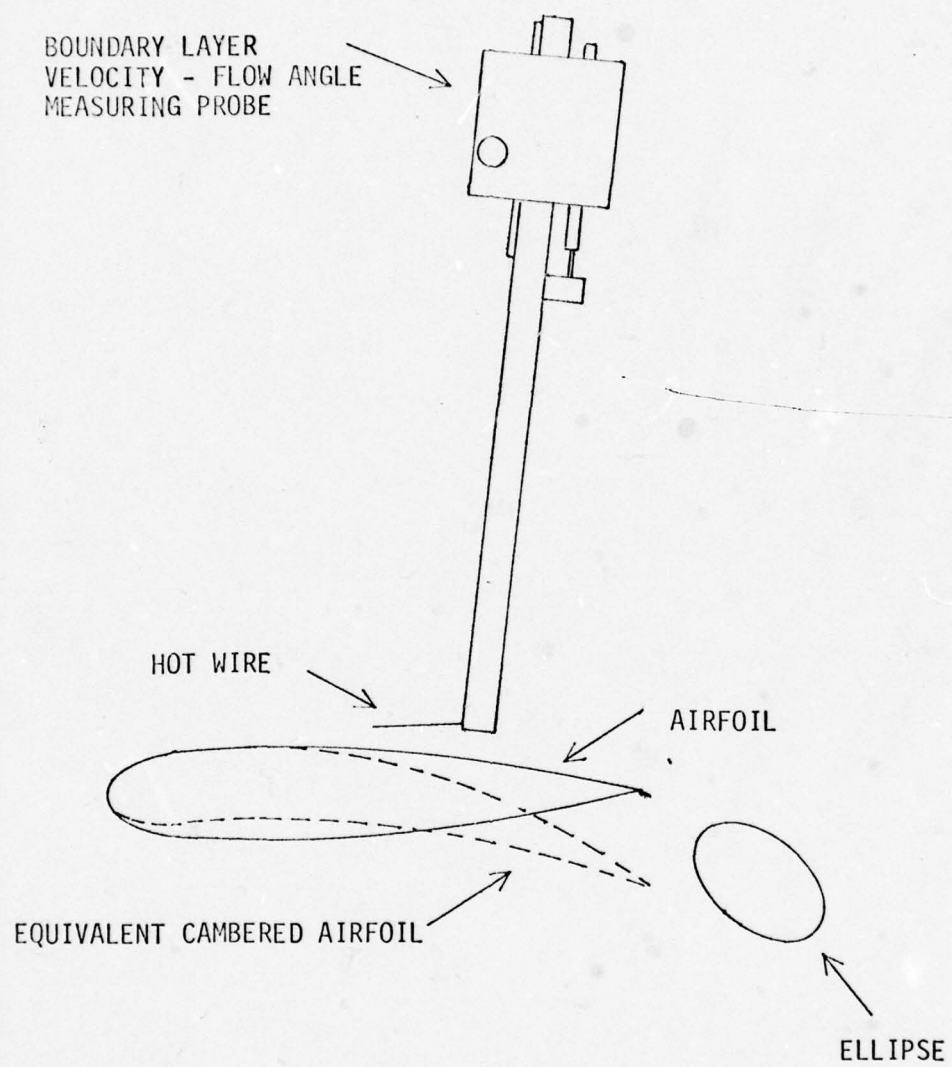


FIG. 1 SCHEMATIC DIAGRAM OF THE EXPERIMENT

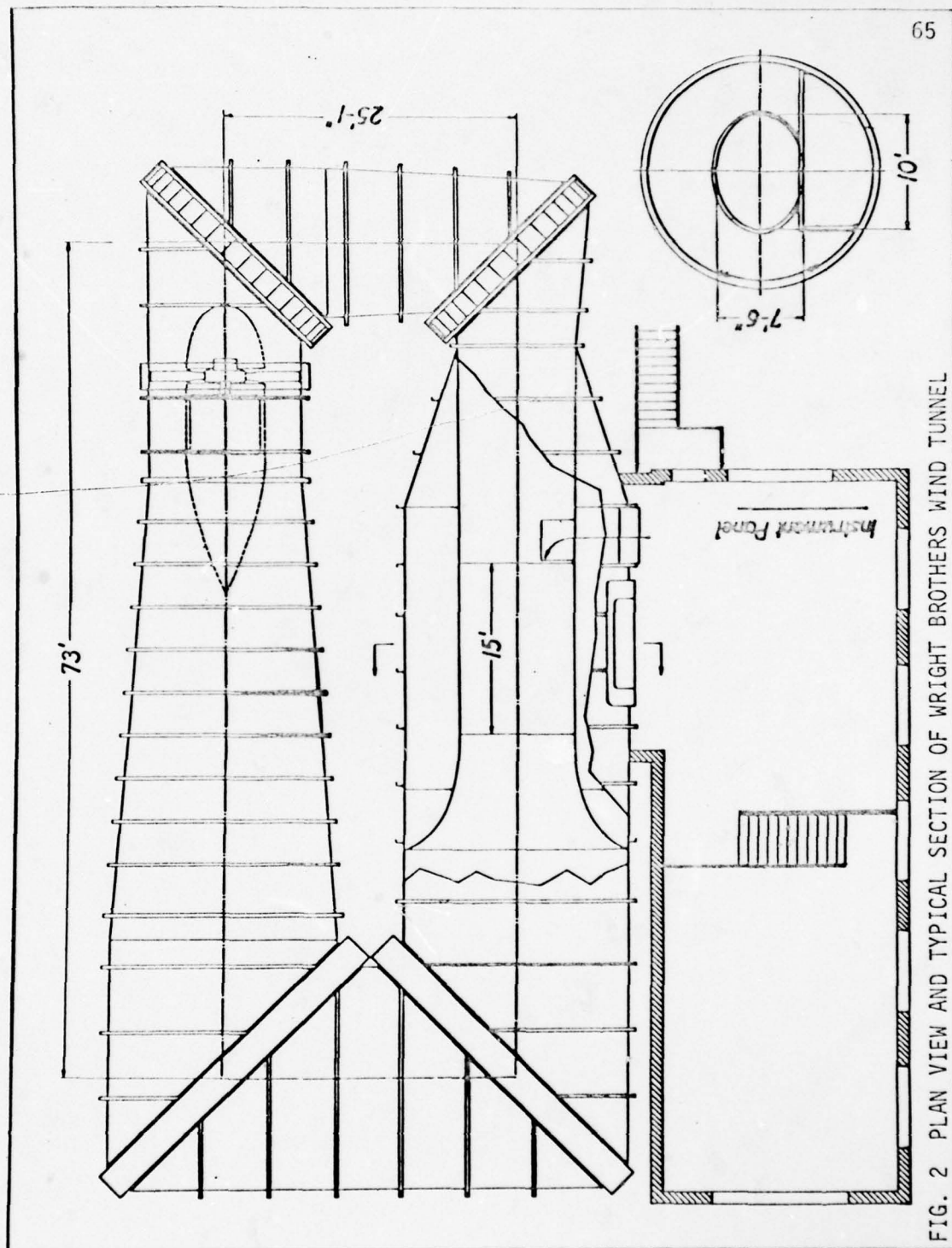


FIG. 2 PLAN VIEW AND TYPICAL SECTION OF WRIGHT BROTHERS WIND TUNNEL



- ◻ ELLIPSE
- ◻ AIRFOIL
- ◻ SIDEBOARDS

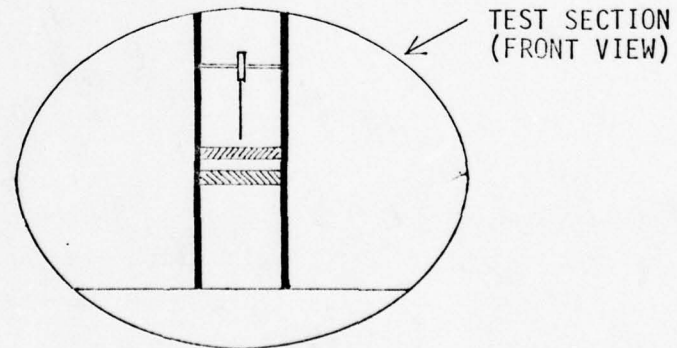


FIG. 3 DIFFERENT VIEWS OF THE AIRFOIL, ELLIPSE, PROBE AND SIDEBOARDS

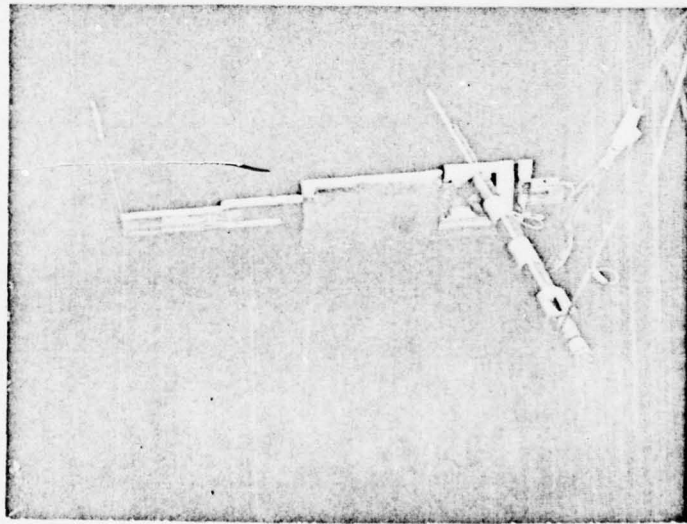
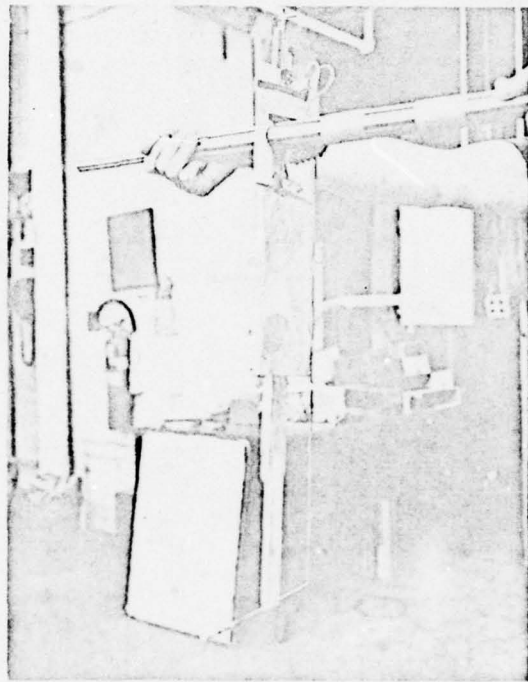


FIG. 4a THE BOUNDARY LAYER VELOCITY-FLOW ANGLE MEASURING PROBE

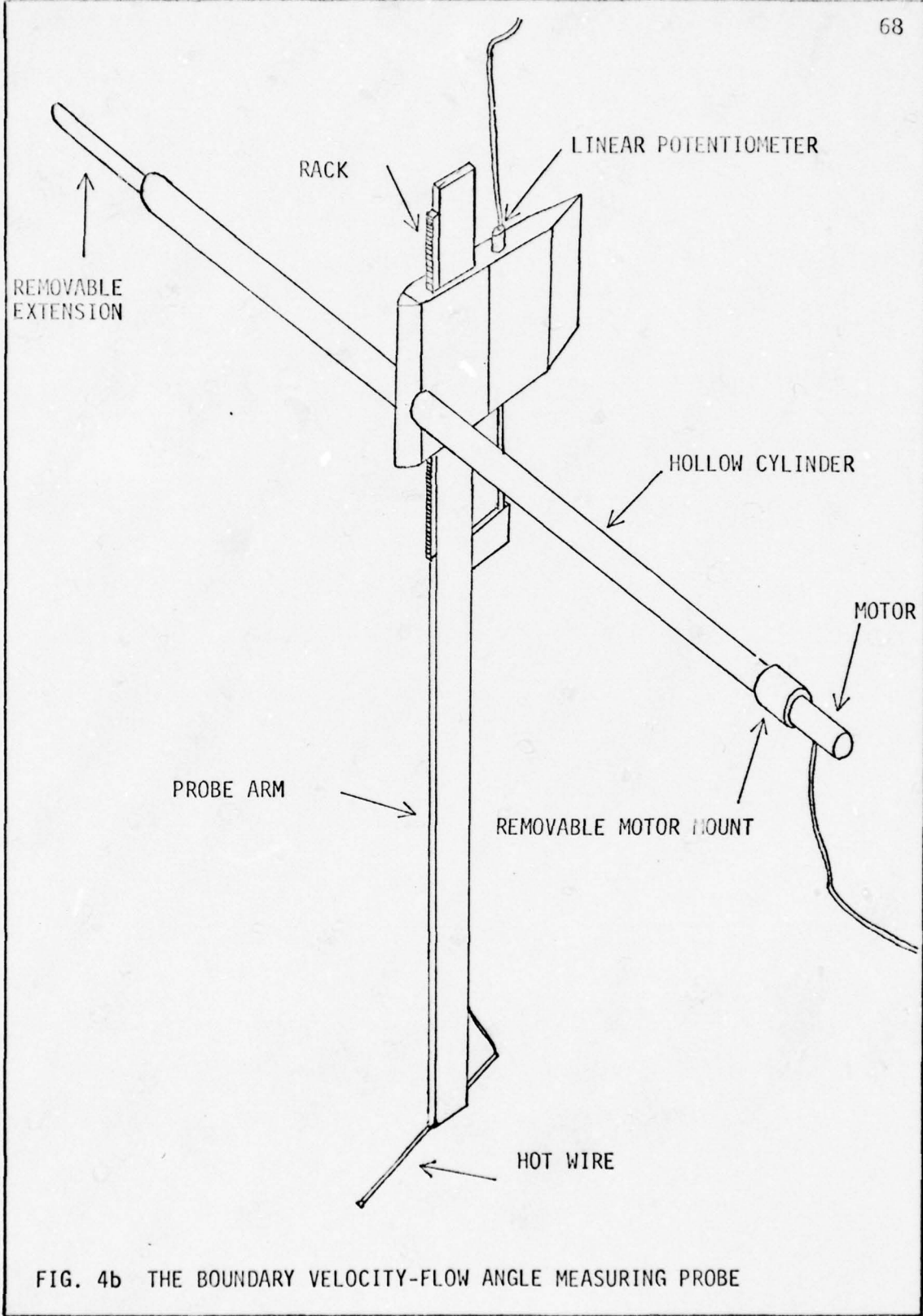


FIG. 4b THE BOUNDARY VELOCITY-FLOW ANGLE MEASURING PROBE

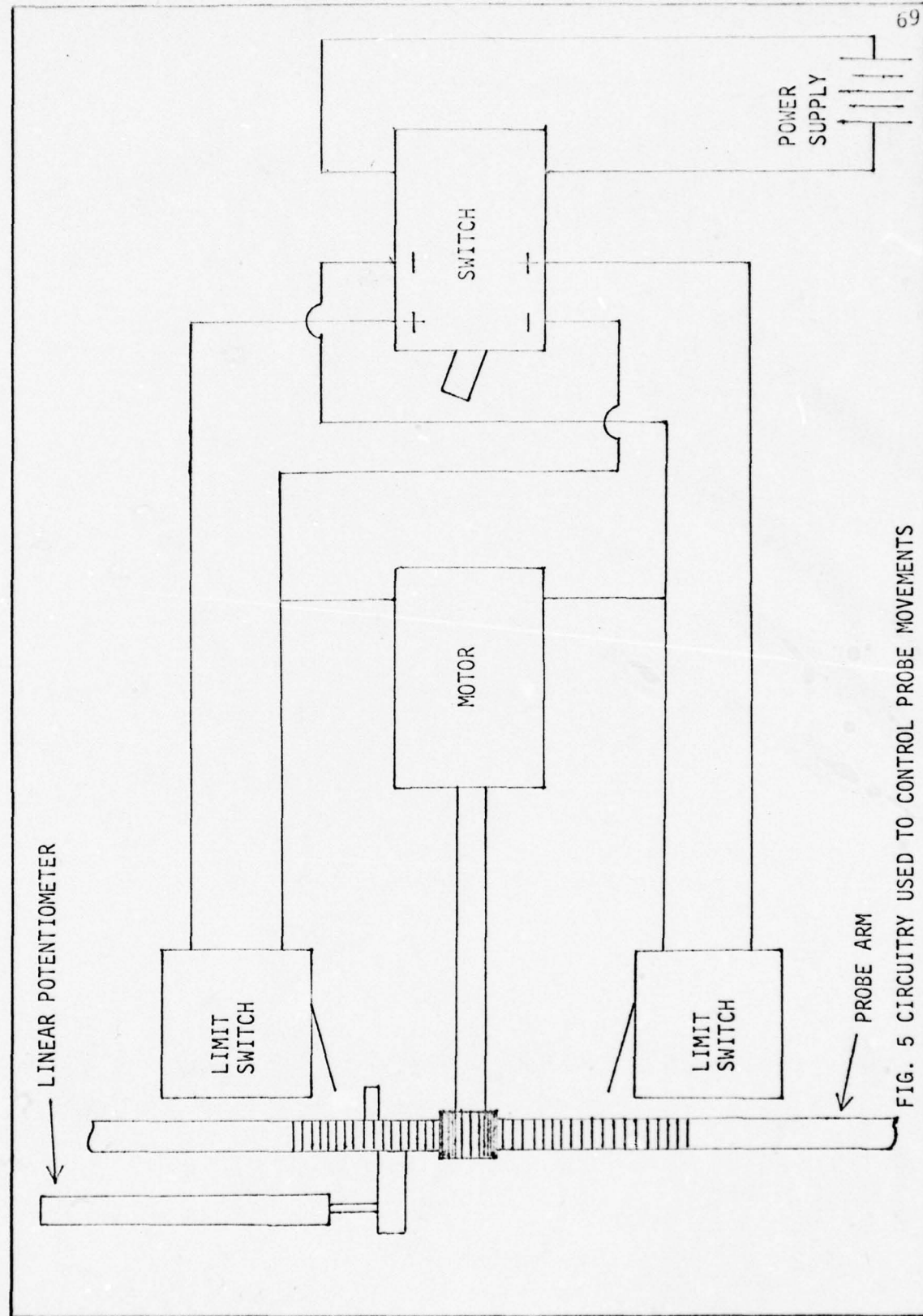


FIG. 5 CIRCUITRY USED TO CONTROL PROBE MOVEMENTS

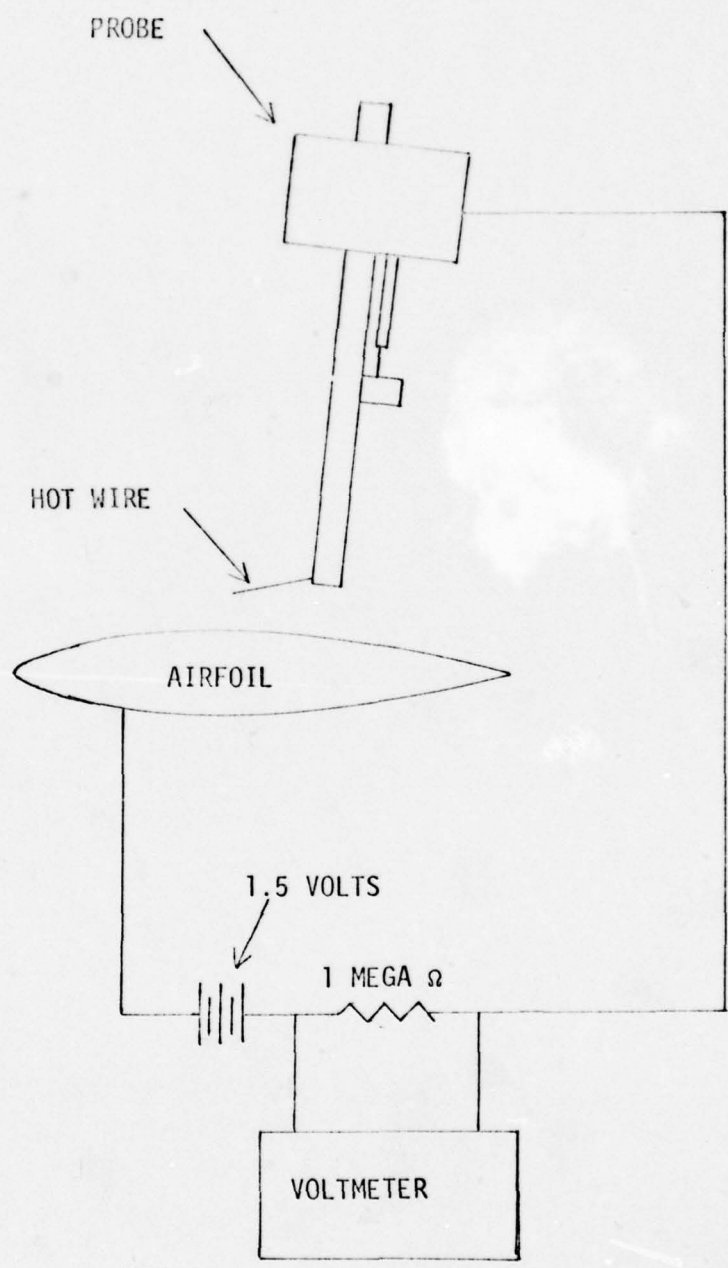


FIG. 6 CIRCUITRY USED TO FIND THE AIRFOIL SURFACE (ZERO HEIGHT)

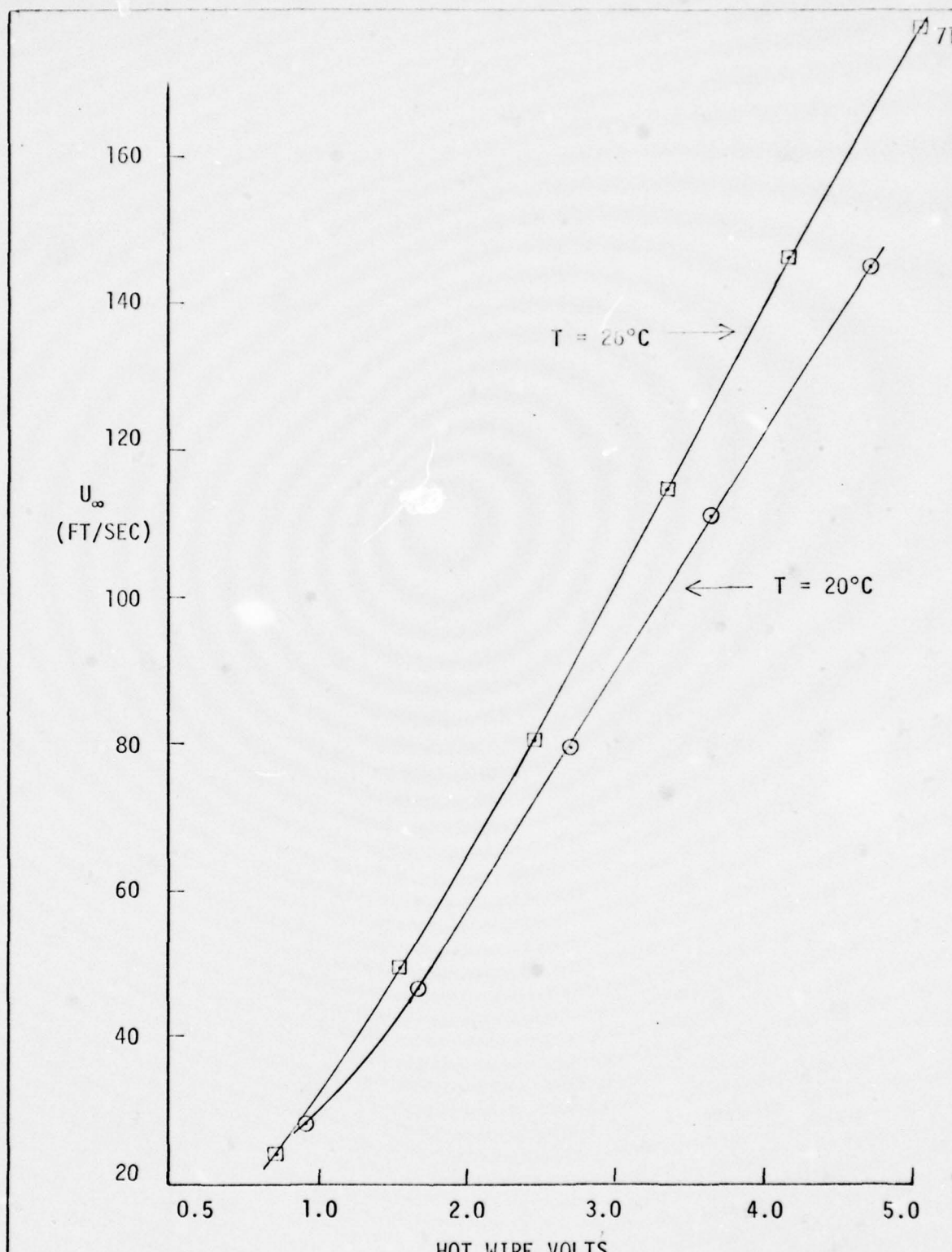
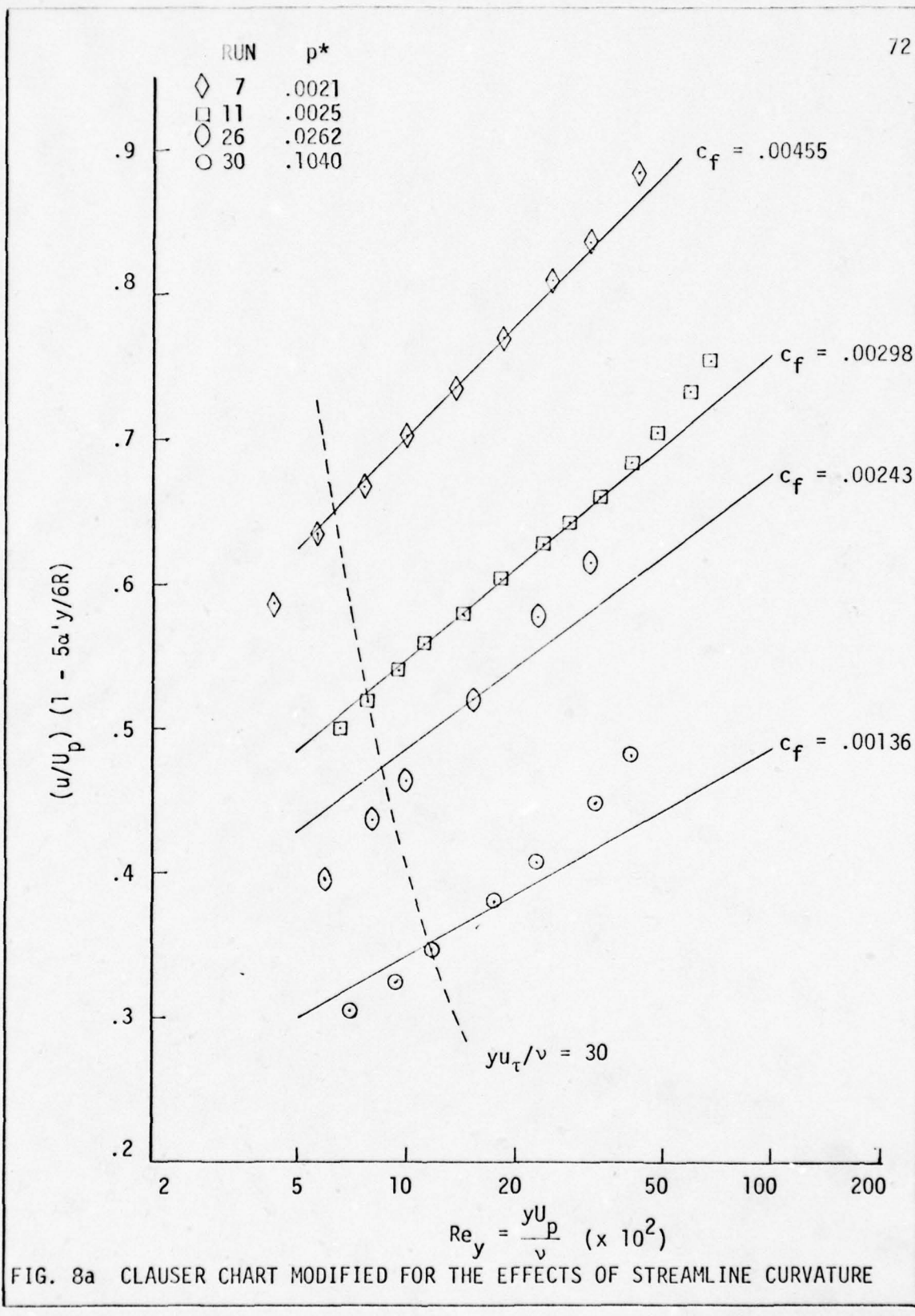


FIG. 7 VELOCITY VS HOT WIRE VOLTS: HOT WIRE CALIBRATION CURVES FOR ONE DAYS RUNS (5/25/78)



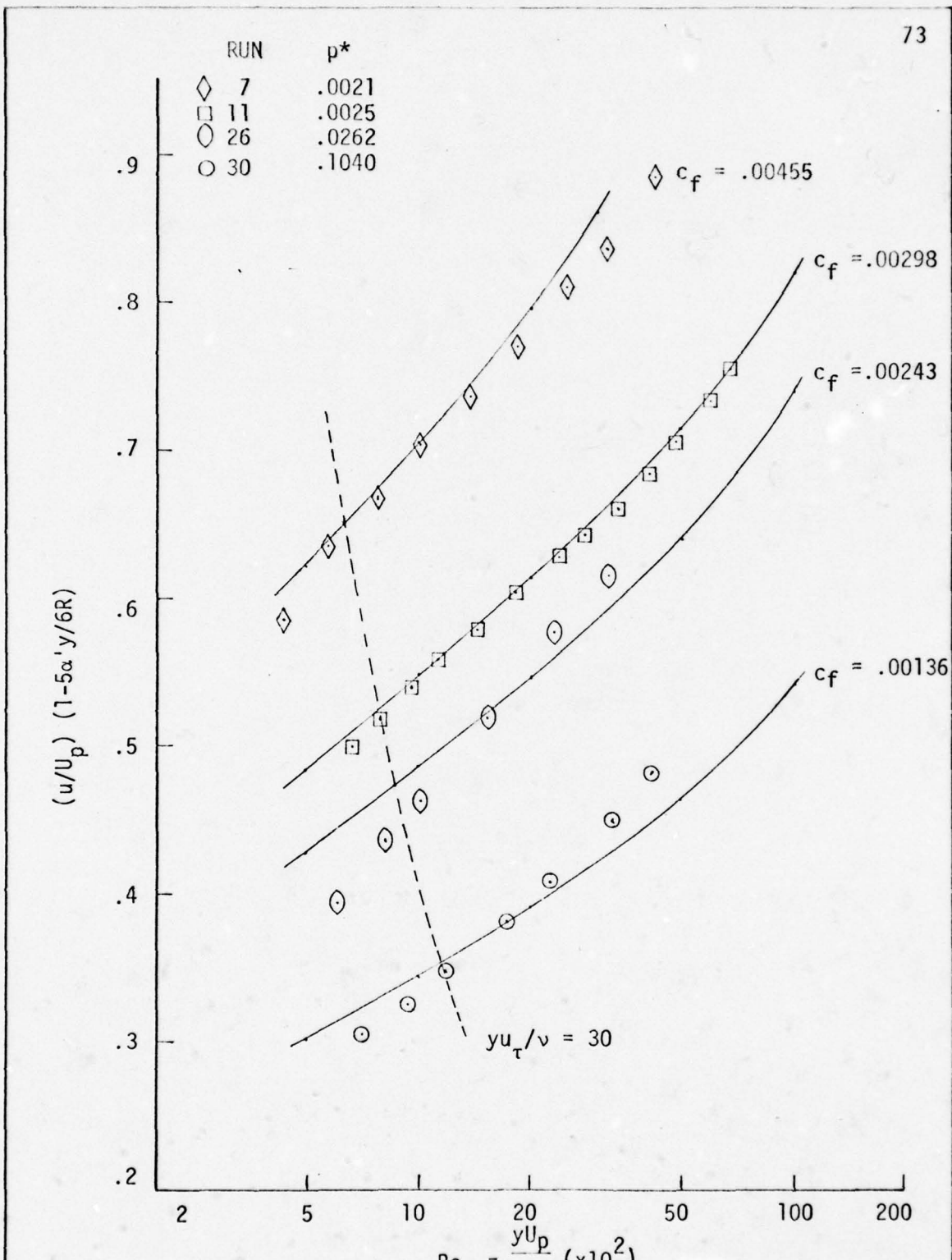


FIG. 8b CLAUSER CHART FURTHER MODIFIED WITH STUREK'S MIXING LENGTH ASSUMPTION

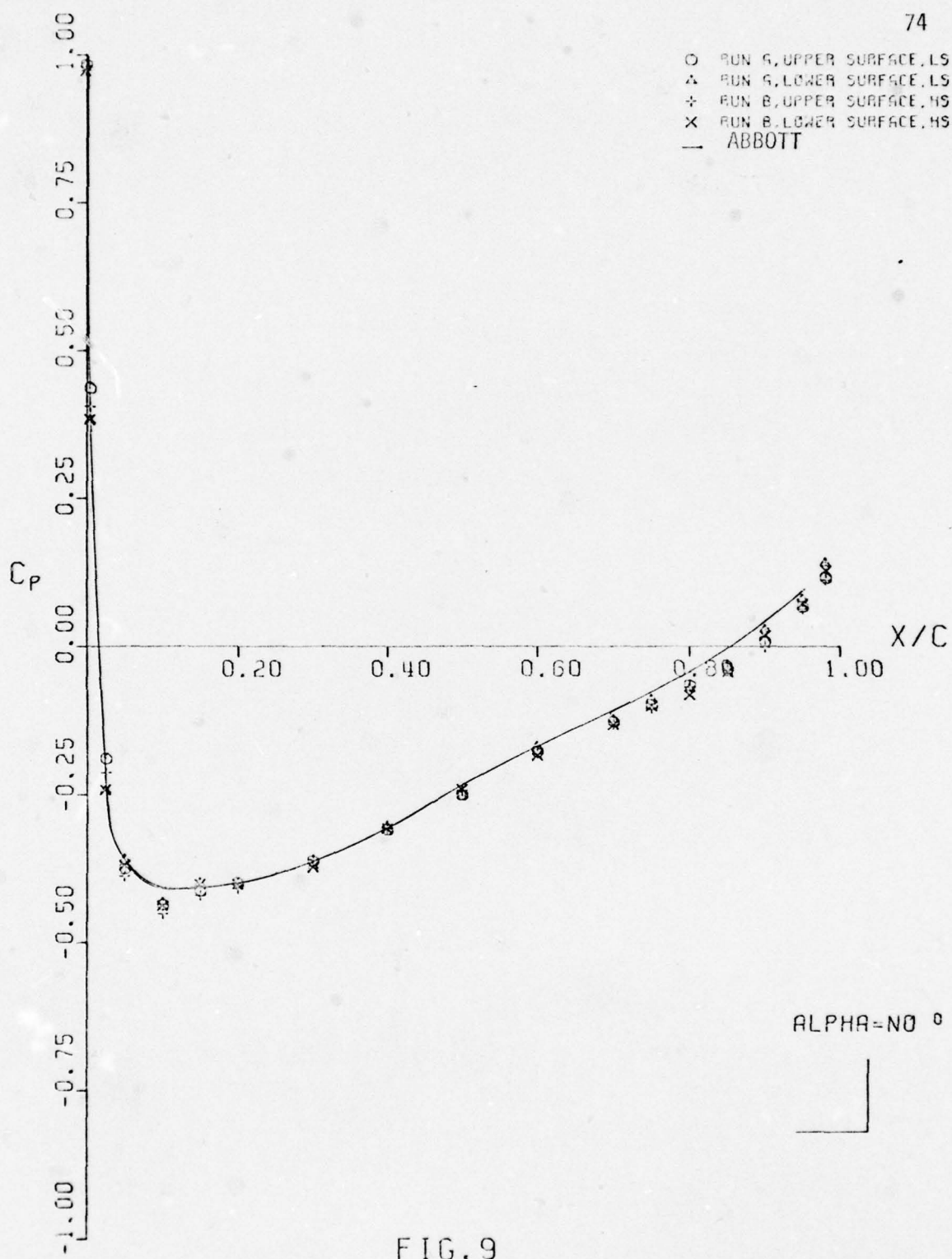
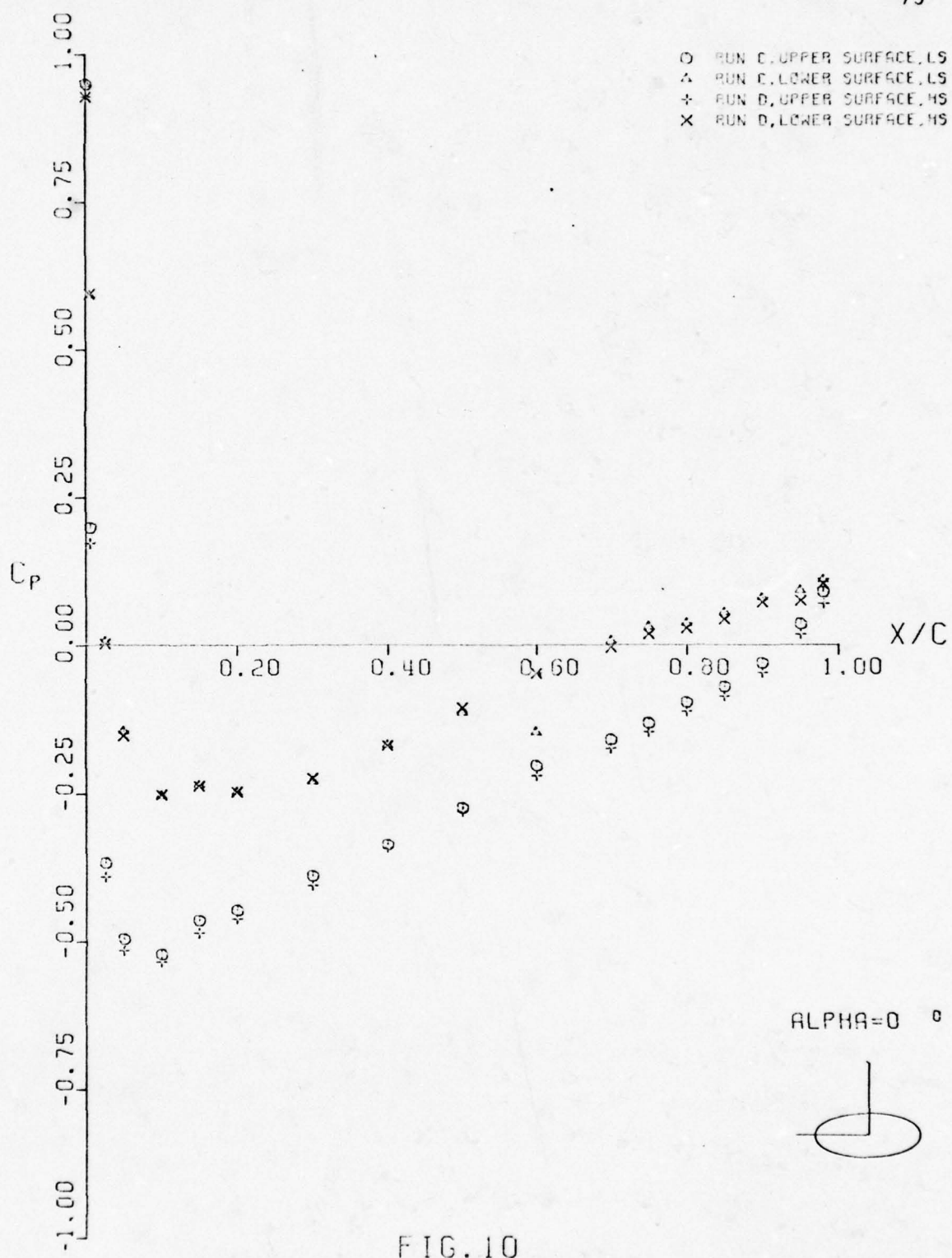


FIG. 9  
PRESSURE COEFFICIENT VS. NONDIMENSIONAL CHORD

FIG. 10  
PRESSURE COEFFICIENT VS. NONDIMENSIONAL CHORD

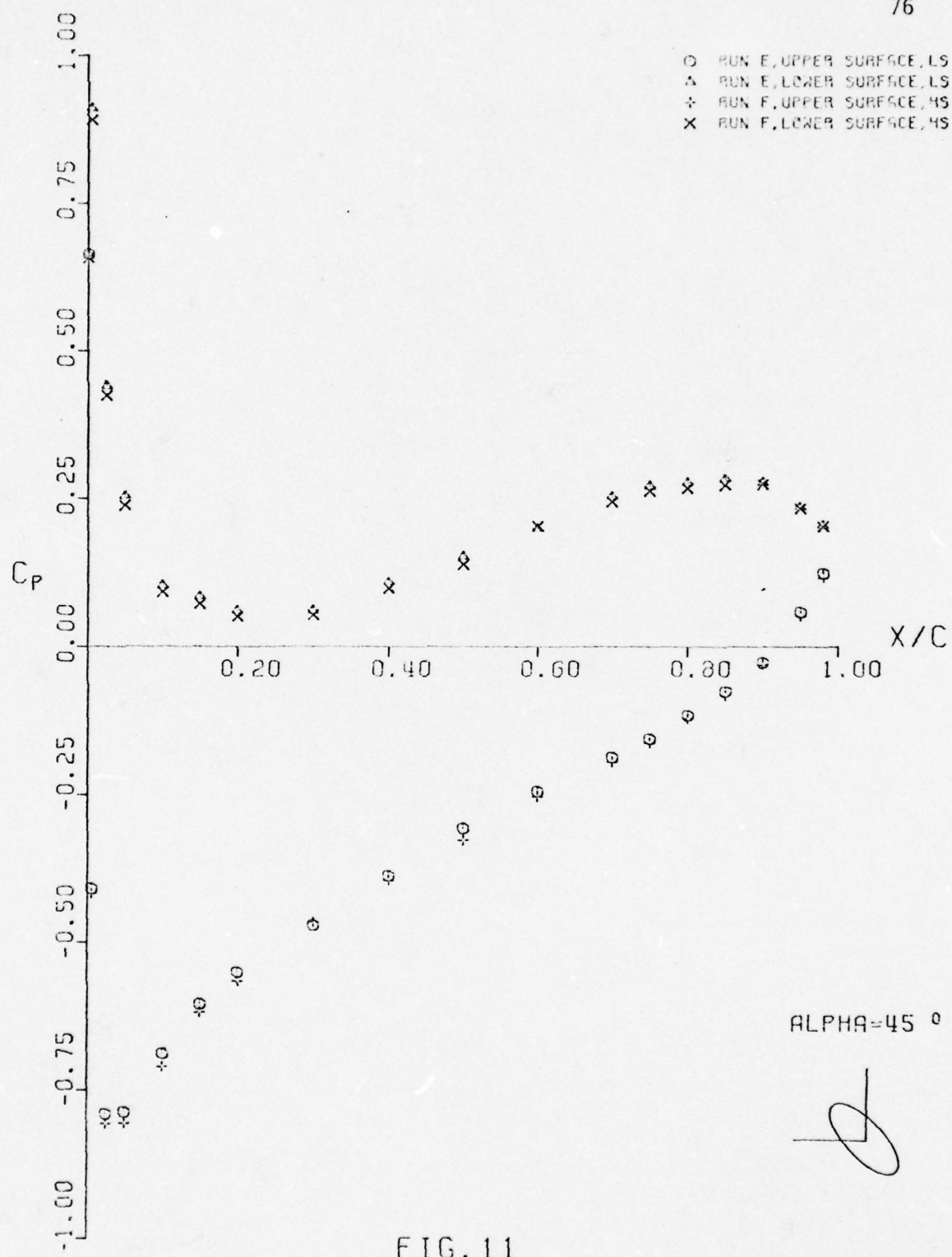


FIG. 11  
PRESSURE COEFFICIENT VS. NONDIMENSIONAL CHORD

RUN G, UPPER SURFACE, LS  
RUN G, LOWER SURFACE, LS

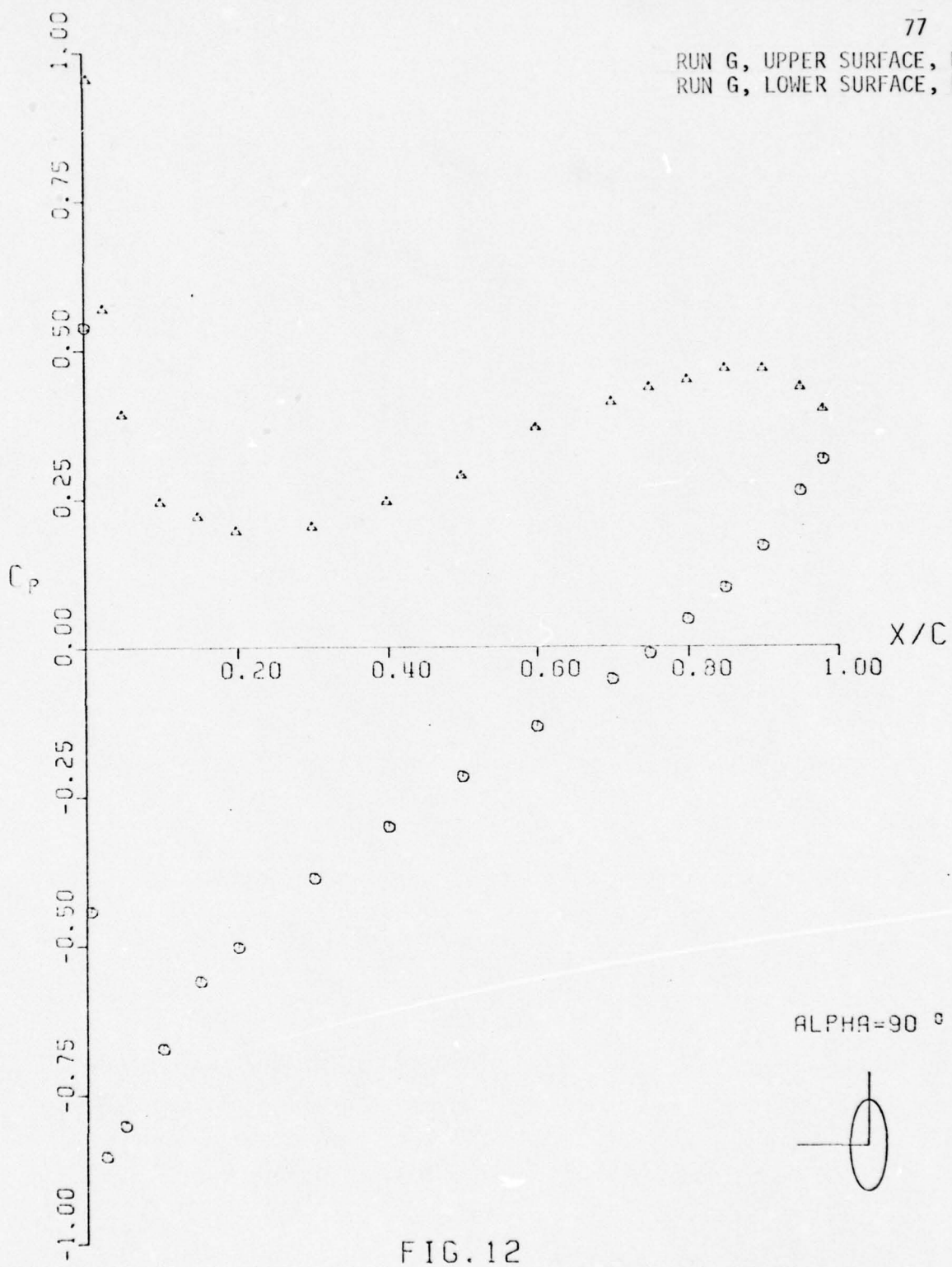
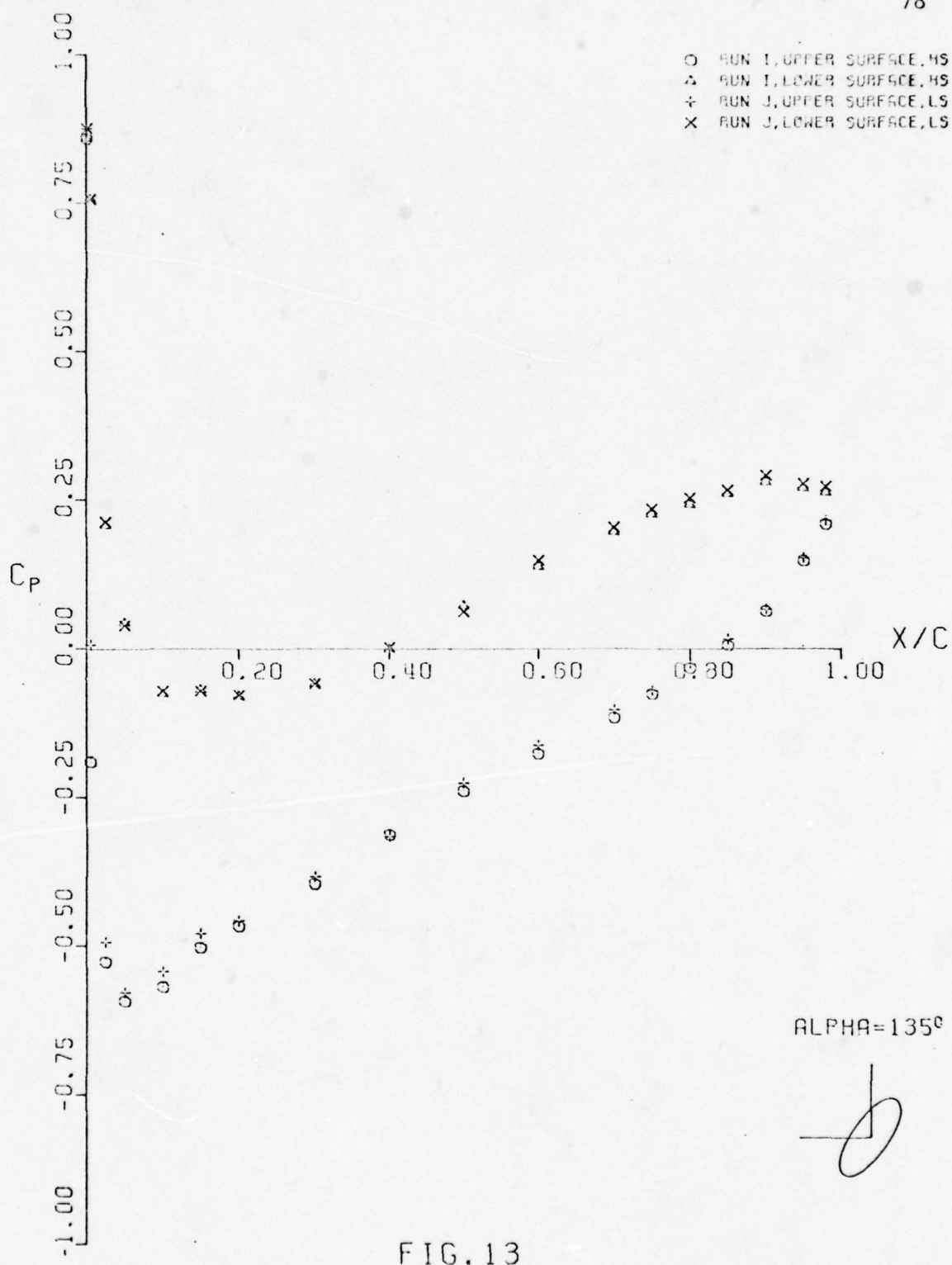


FIG. 12

PRESSURE COEFFICIENT VS. NONDIMENSIONAL CHORD

FIG. 13  
PRESSURE COEFFICIENT VS. NONDIMENSIONAL CHORD

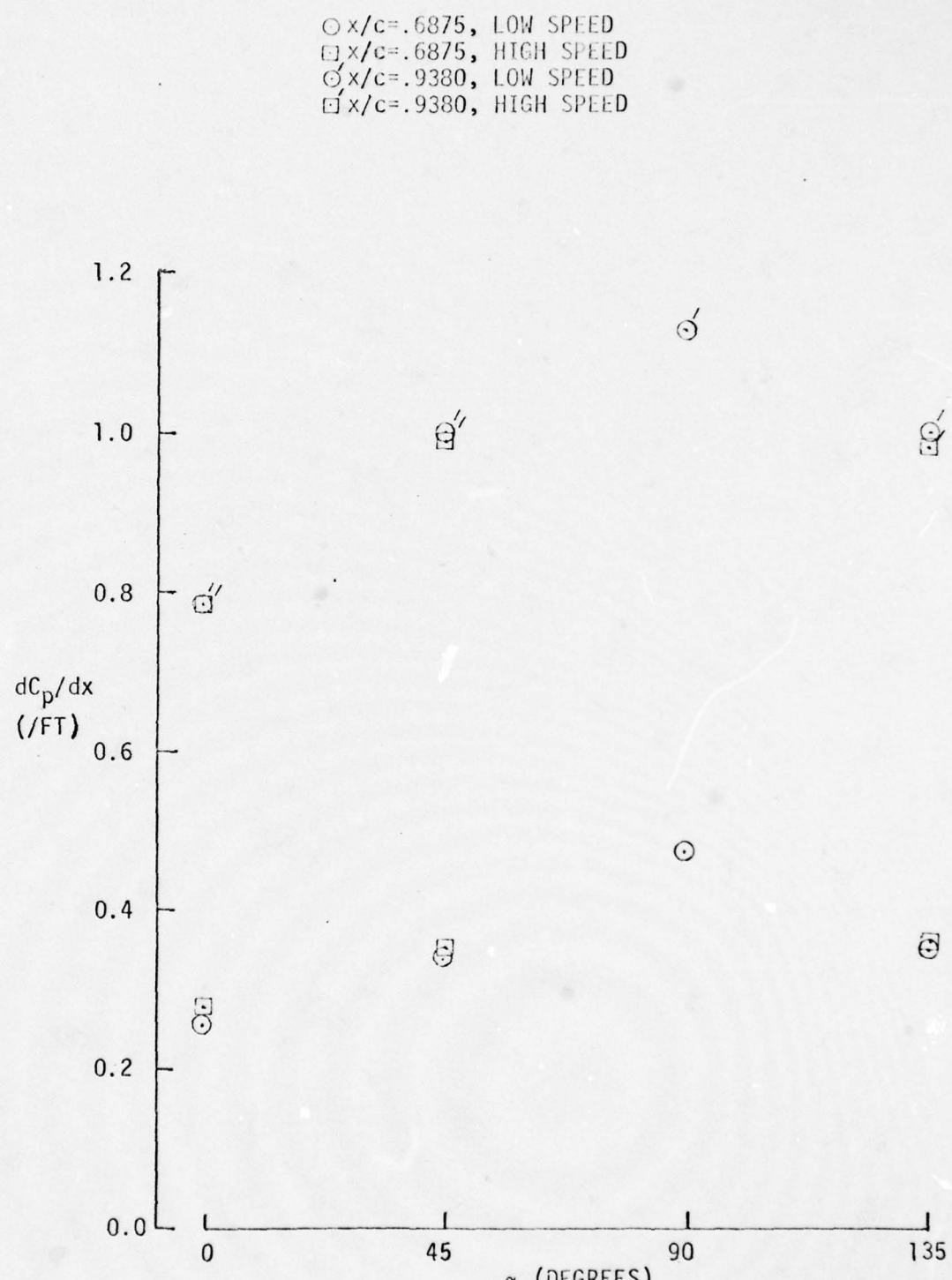


FIG.14 AXIAL PRESSURE COEFFICIENT GRADIENT VS. ELLIPSE ANGLE

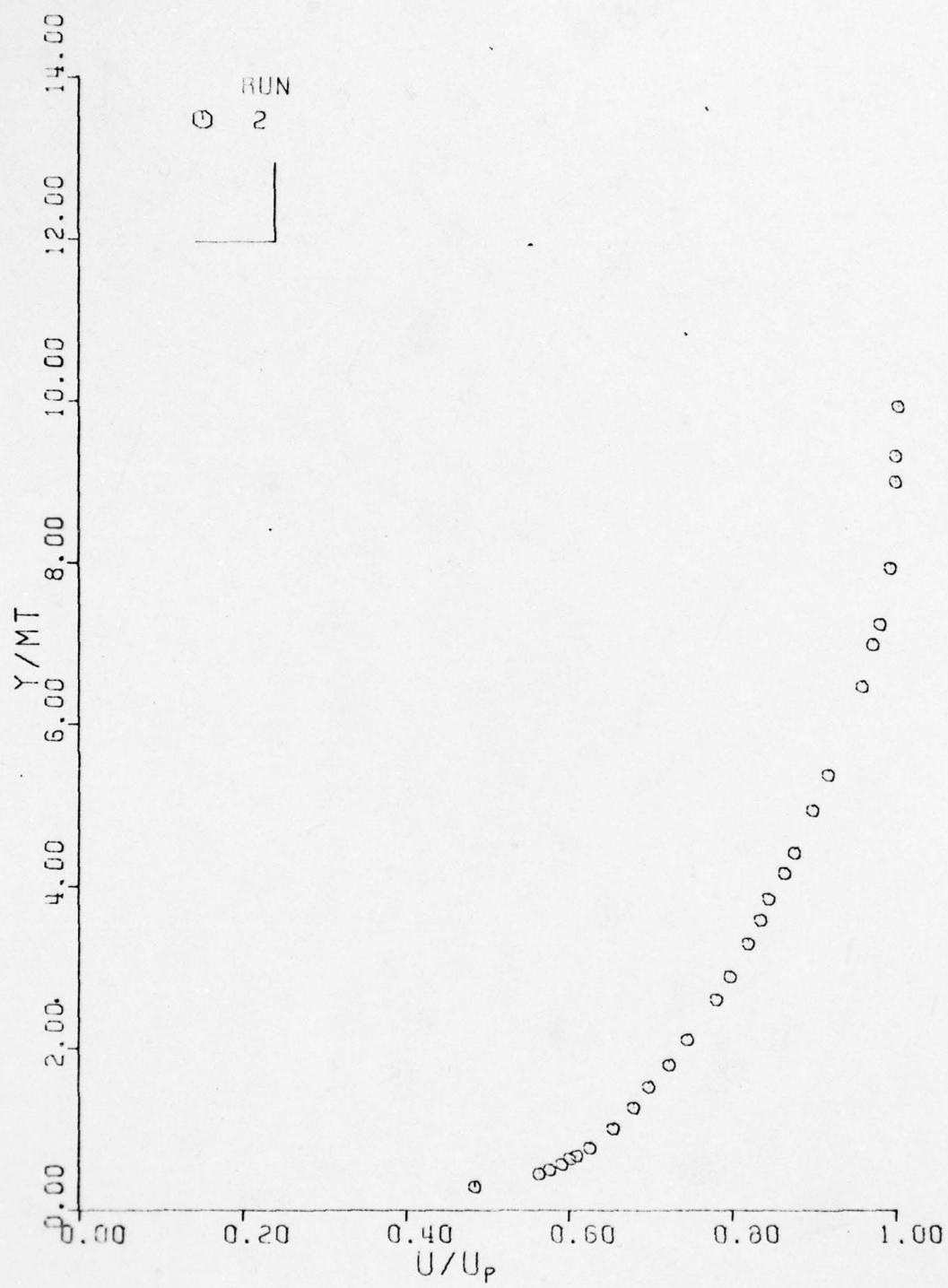


FIG.15  
NONDIMENSIONAL BOUNDARY LAYER PROFILES  
 $X/C=0.6875$     $\text{ALPHA}=0^\circ$

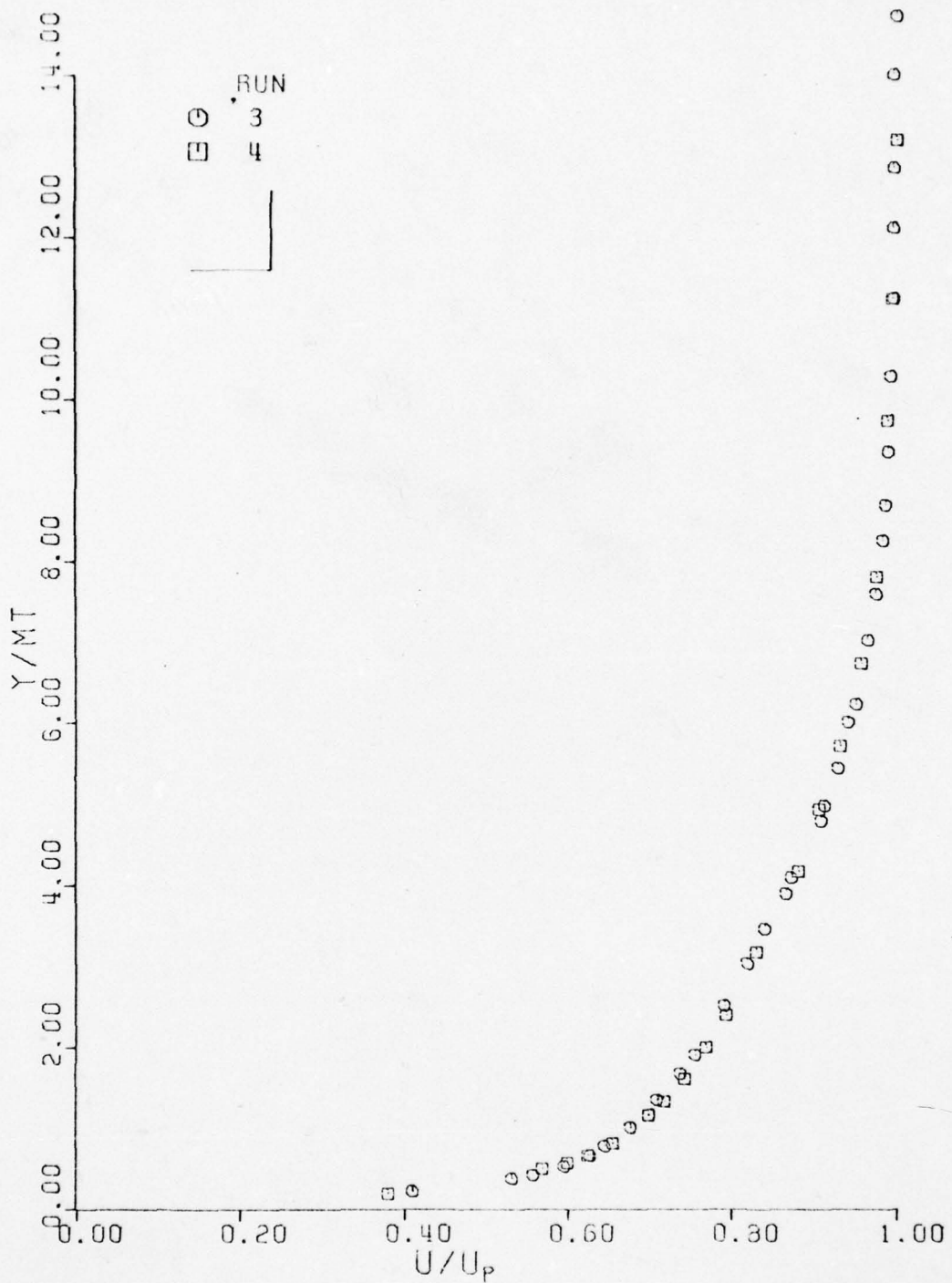


FIG. 16  
NONDIMENSIONAL BOUNDARY LAYER PROFILES  
 $X/C = 0.6875$        $\text{ALPHA} = 0^\circ$

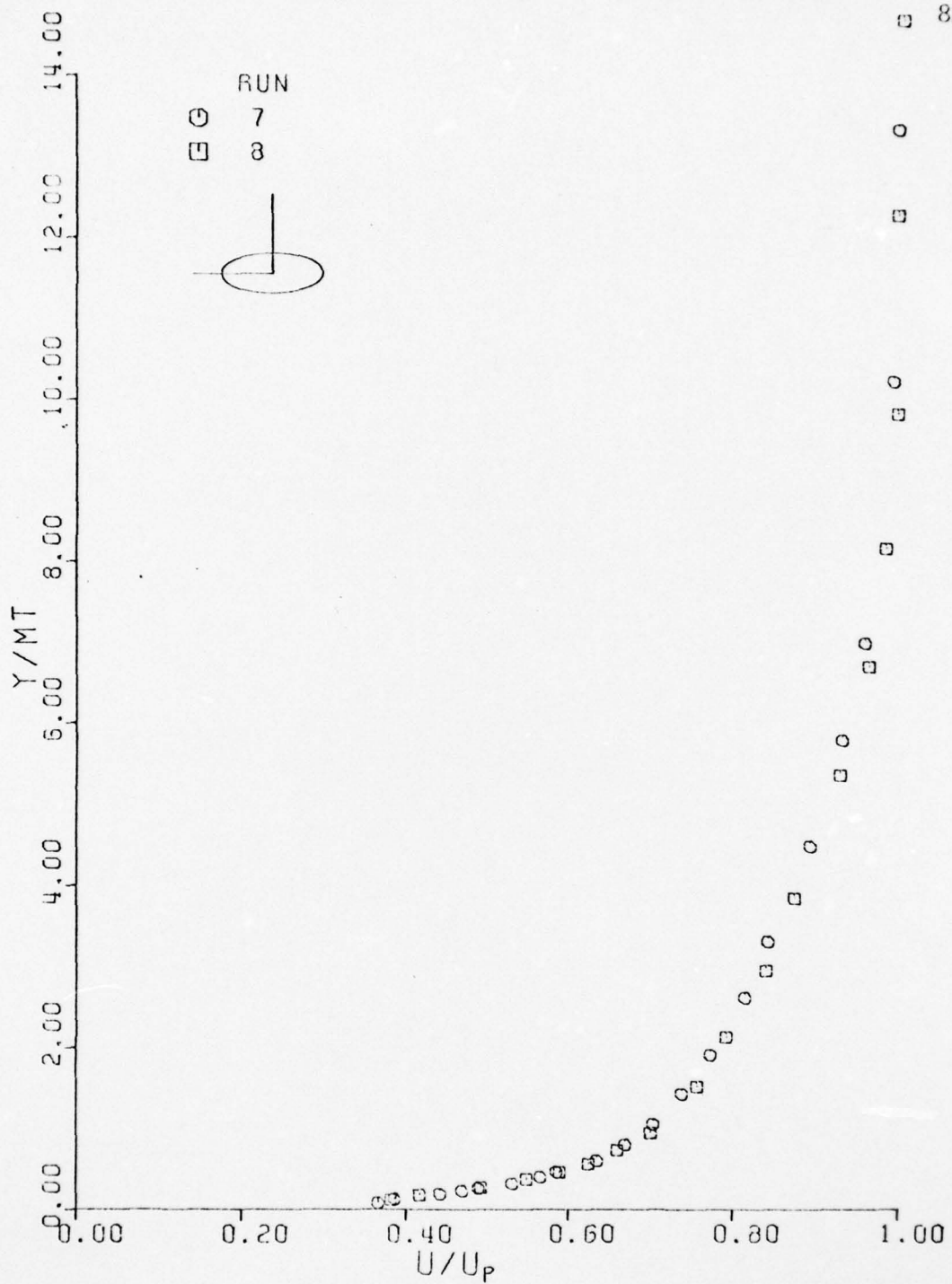


FIG.17  
NONDIMENSIONAL BOUNDARY LAYER PROFILES  
 $X/C=0.6875$        $\text{ALPHA}=0^\circ$

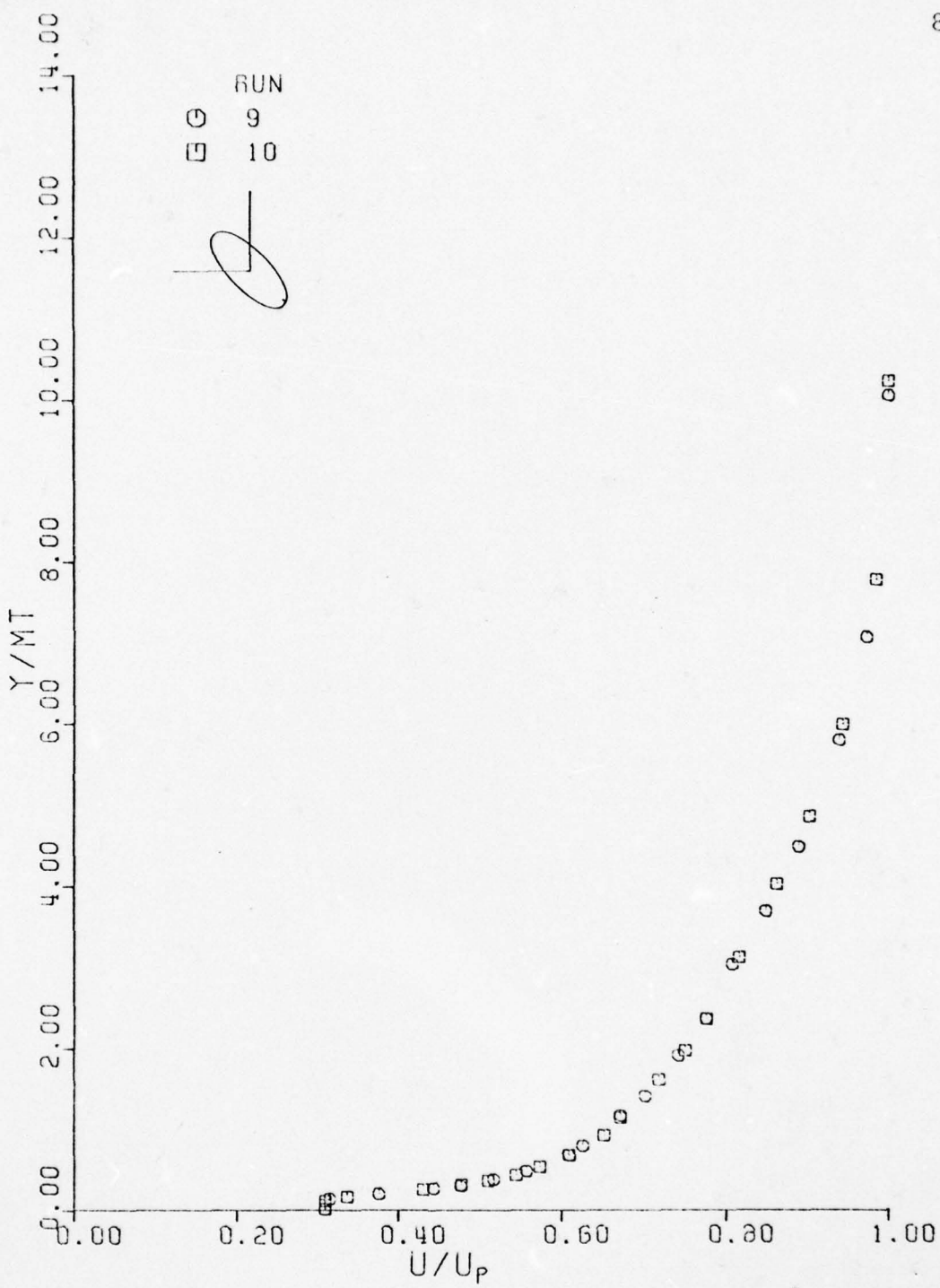


FIG. 18  
NONDIMENSIONAL BOUNDARY LAYER PROFILES  
 $X/C = 0.6875$        $\text{ALPHA} = 45^\circ$

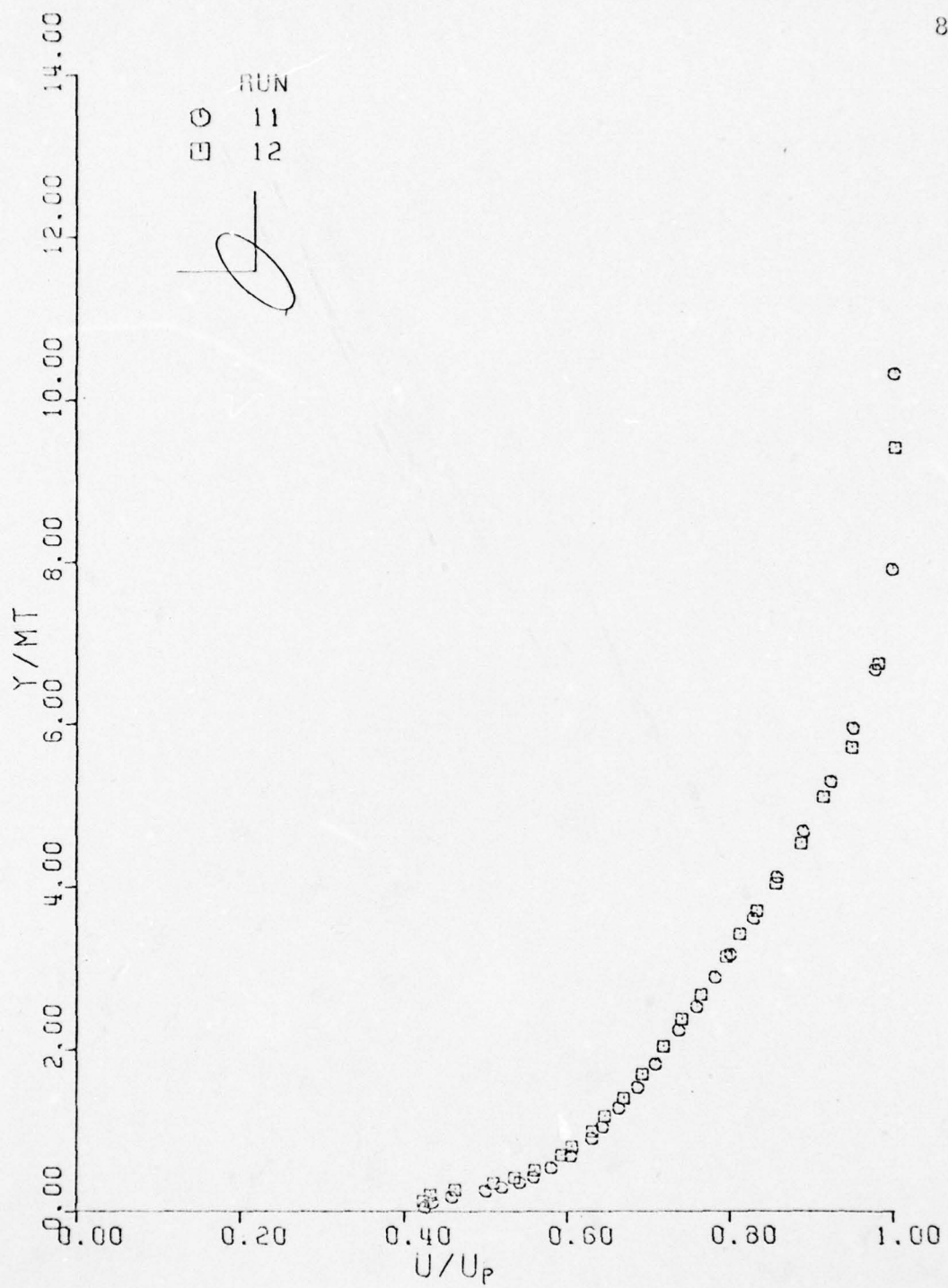


FIG. 19  
NONDIMENSIONAL BOUNDARY LAYER PROFILES  
 $X/C = 0.6875$        $\text{ALPHA} = 45^\circ$

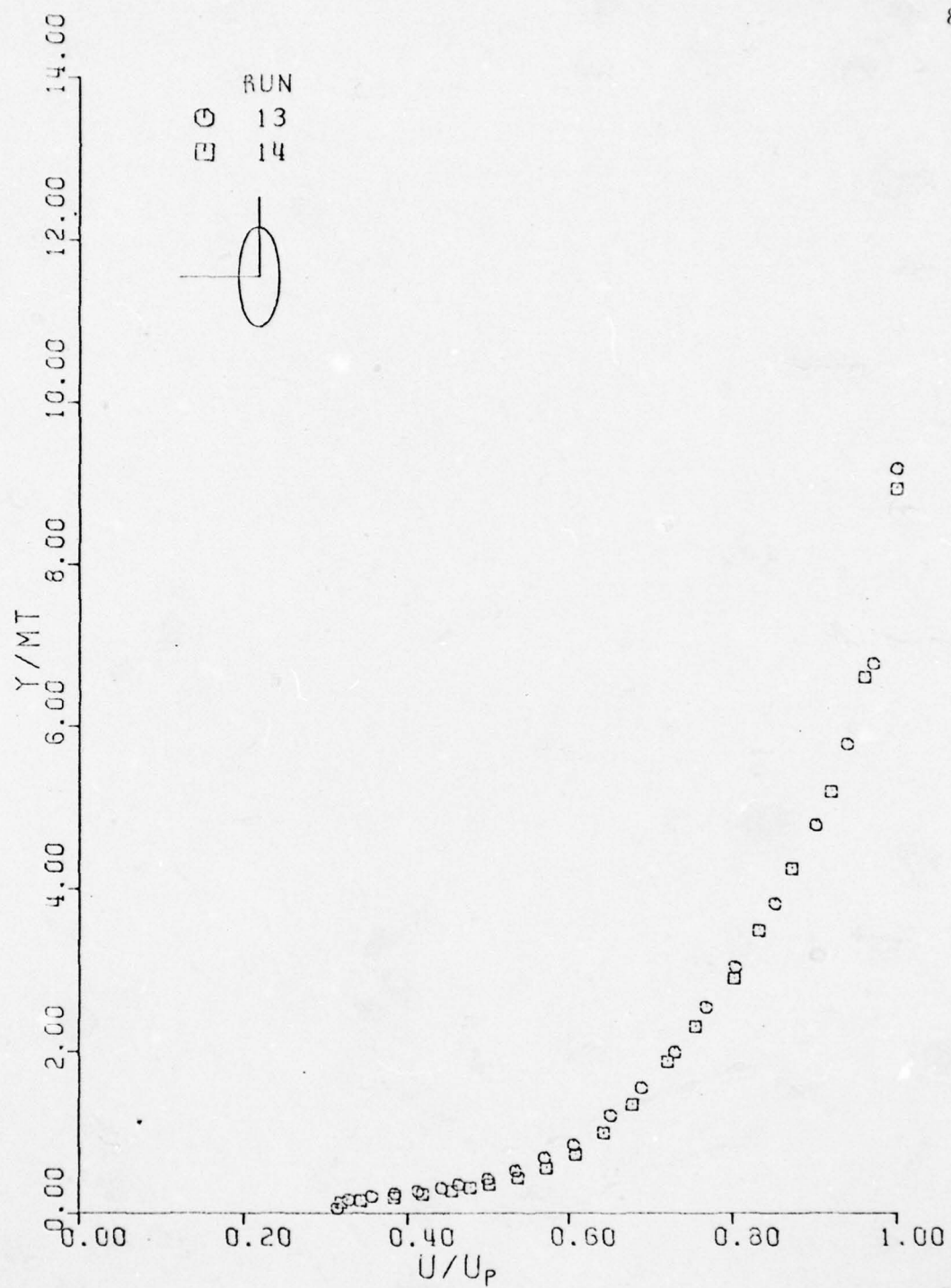


FIG. 20  
NONDIMENSIONAL BOUNDARY LAYER PROFILES  
 $X/C = 0.6875$        $\text{ALPHA} = 90^\circ$

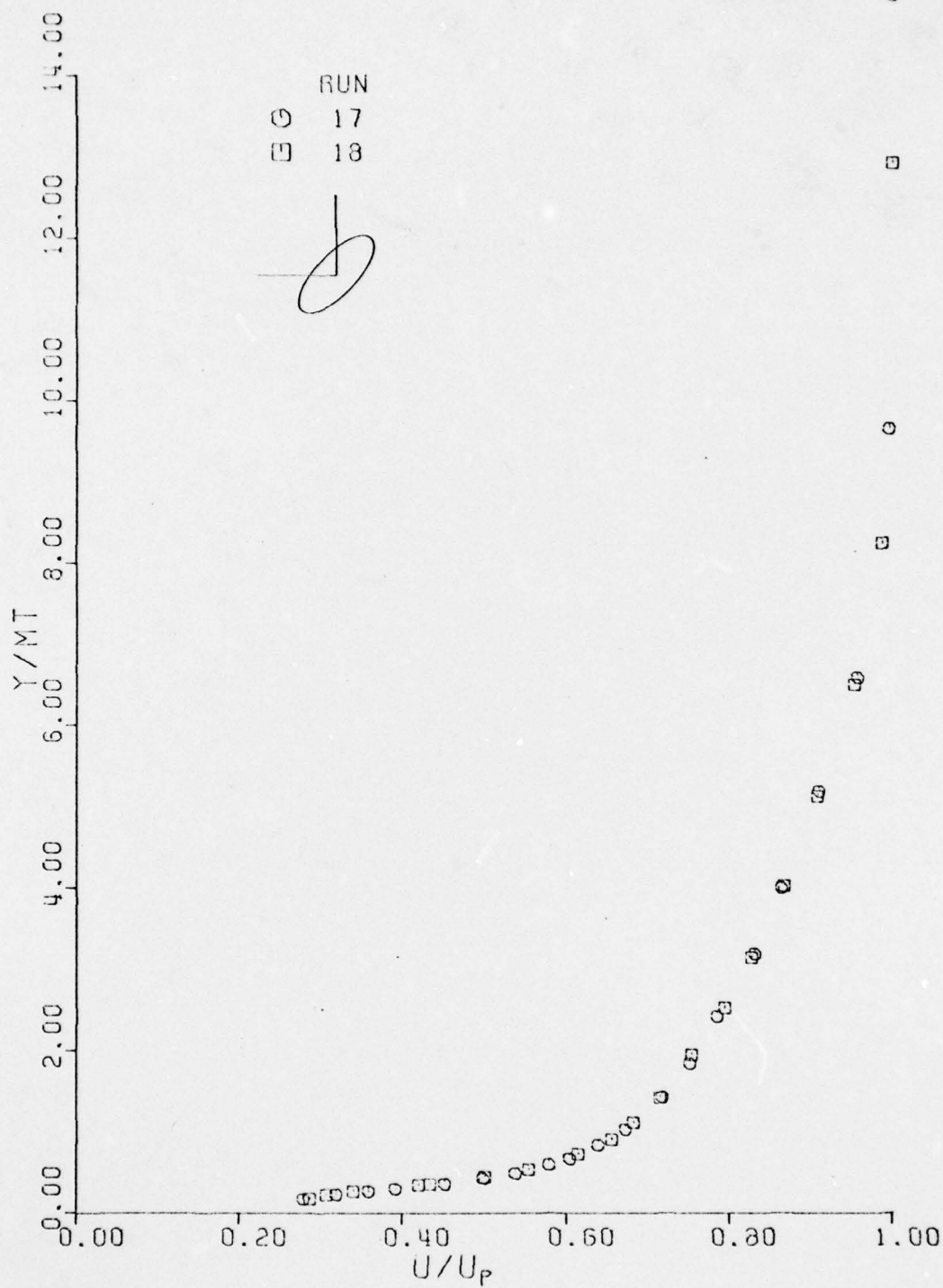


FIG. 21  
NONDIMENSIONAL BOUNDARY LAYER PROFILES  
 $X/C = 0.6875$        $\text{ALPHA} = 135^\circ$

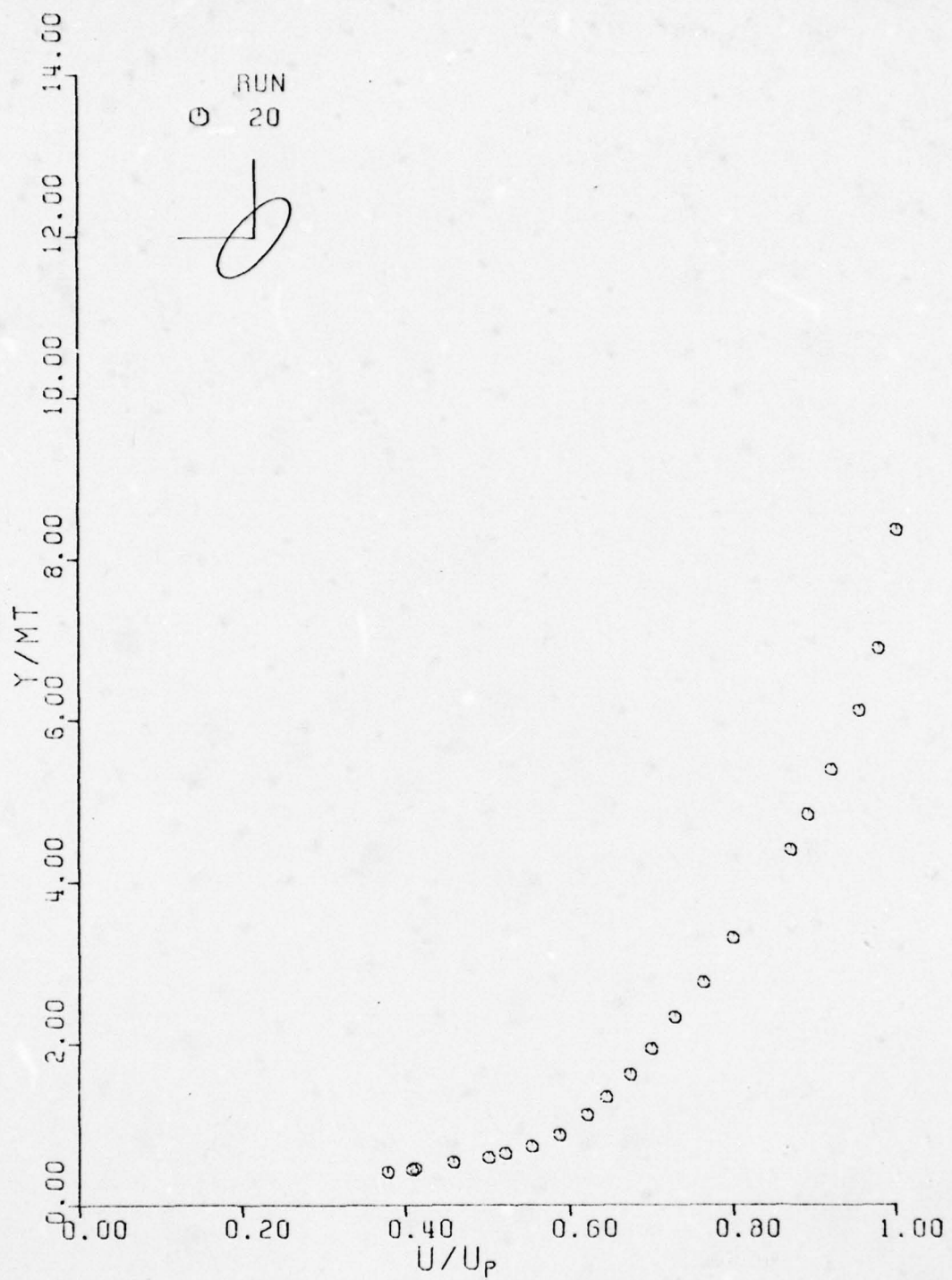


FIG. 22  
NONDIMENSIONAL BOUNDARY LAYER PROFILES  
 $X/C=0.6875$        $\text{ALPHA}=135^\circ$

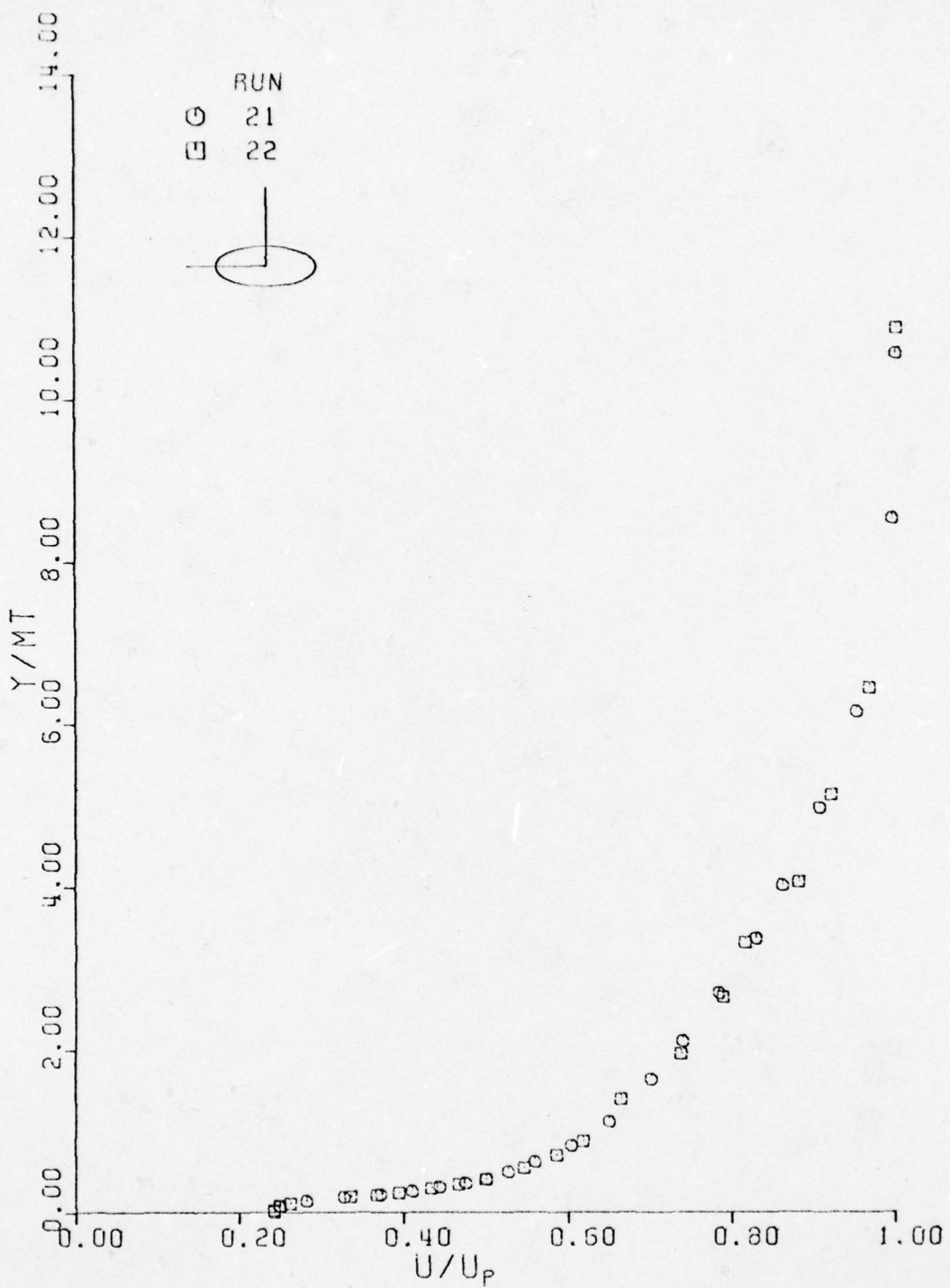


FIG. 23  
NONDIMENSIONAL BOUNDARY LAYER PROFILES  
 $X/C = 0.9380$     $\text{ALPHA} = 0^\circ$

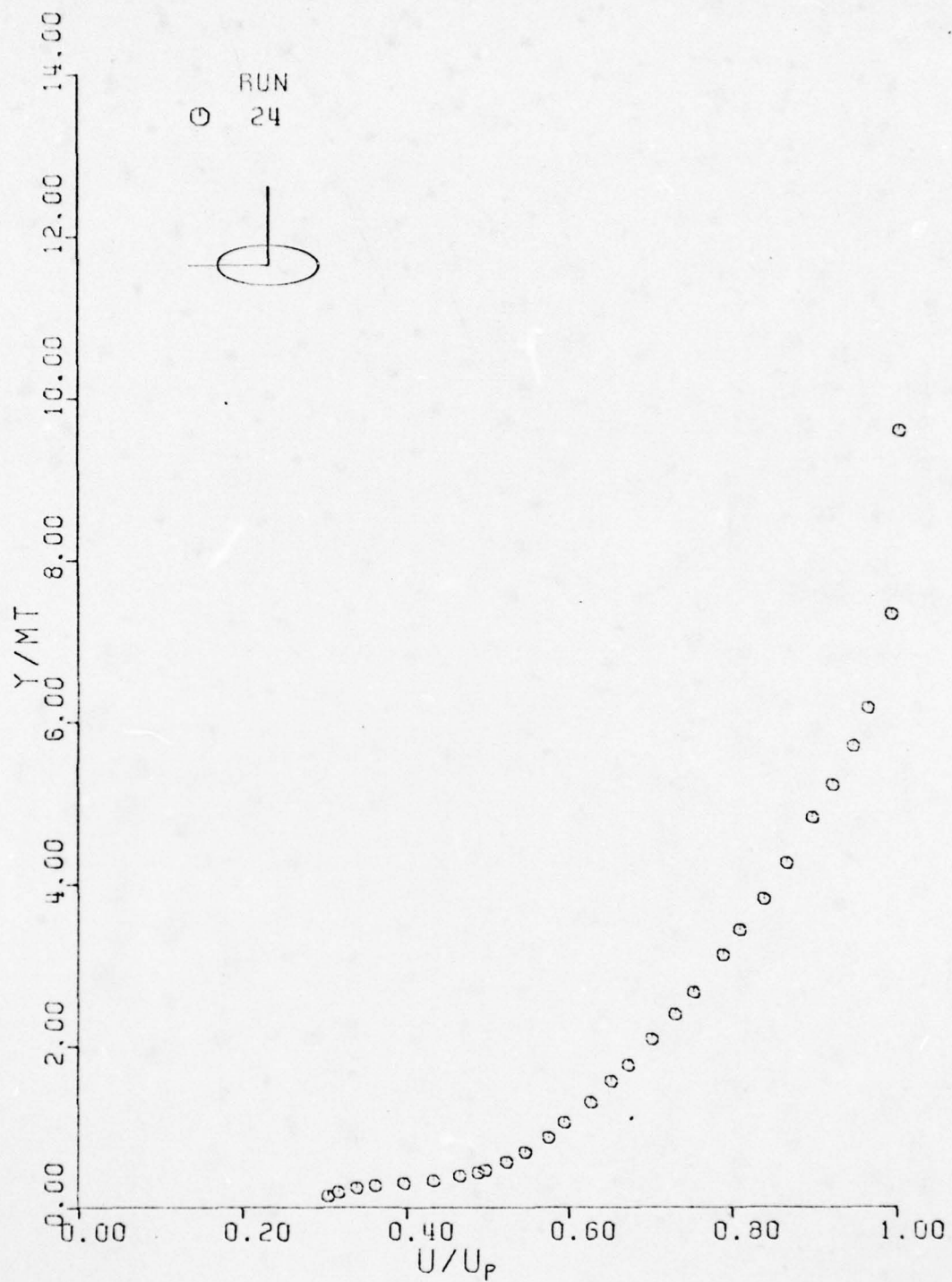


FIG. 24  
NONDIMENSIONAL BOUNDARY LAYER PROFILES  
 $X/C = 0.9380$        $\text{ALPHA} = 0^\circ$

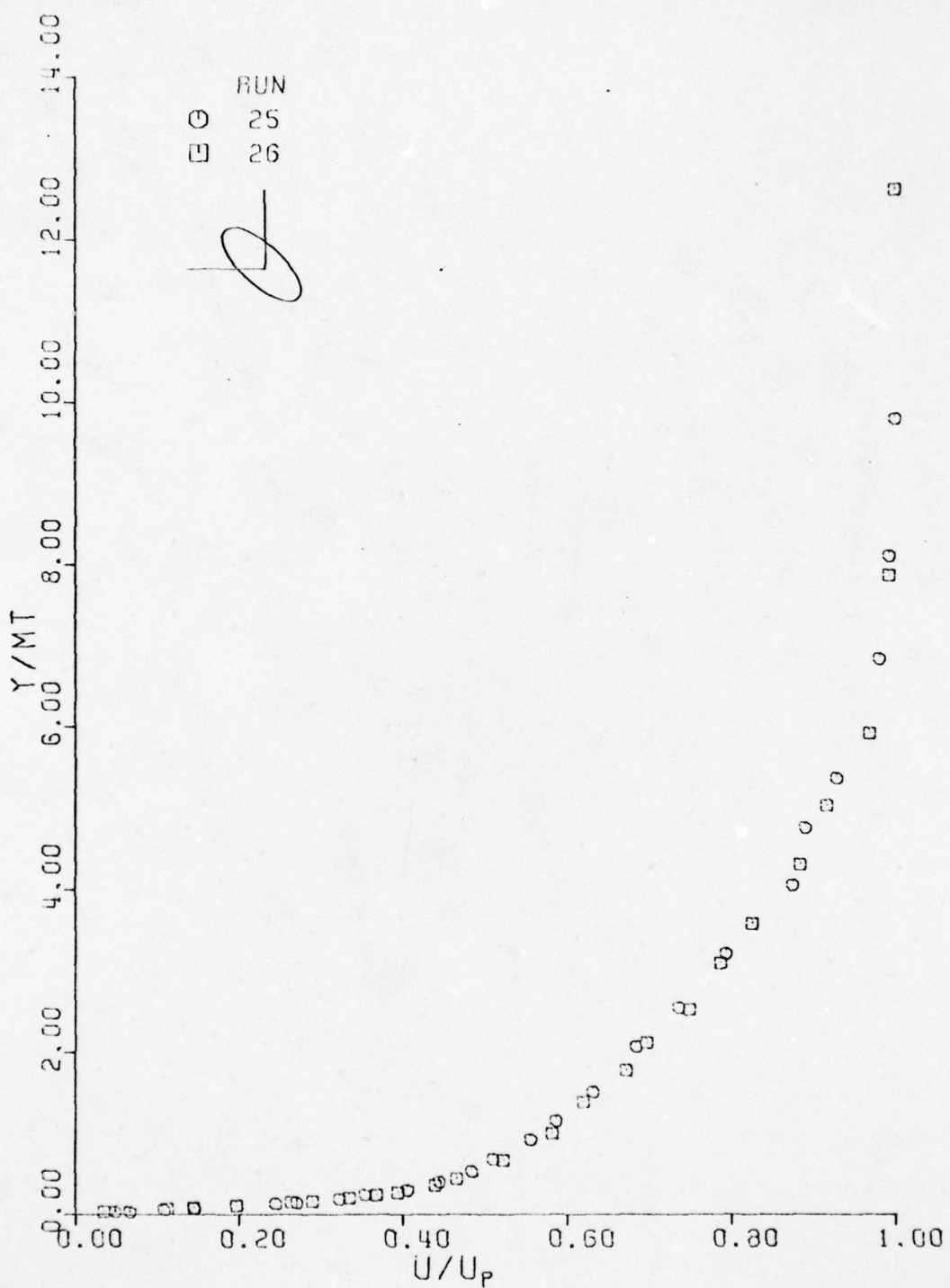


FIG. 25  
NONDIMENSIONAL BOUNDARY LAYER PROFILES  
 $X/C = 0.9380$        $\text{ALPHA} = 45^\circ$

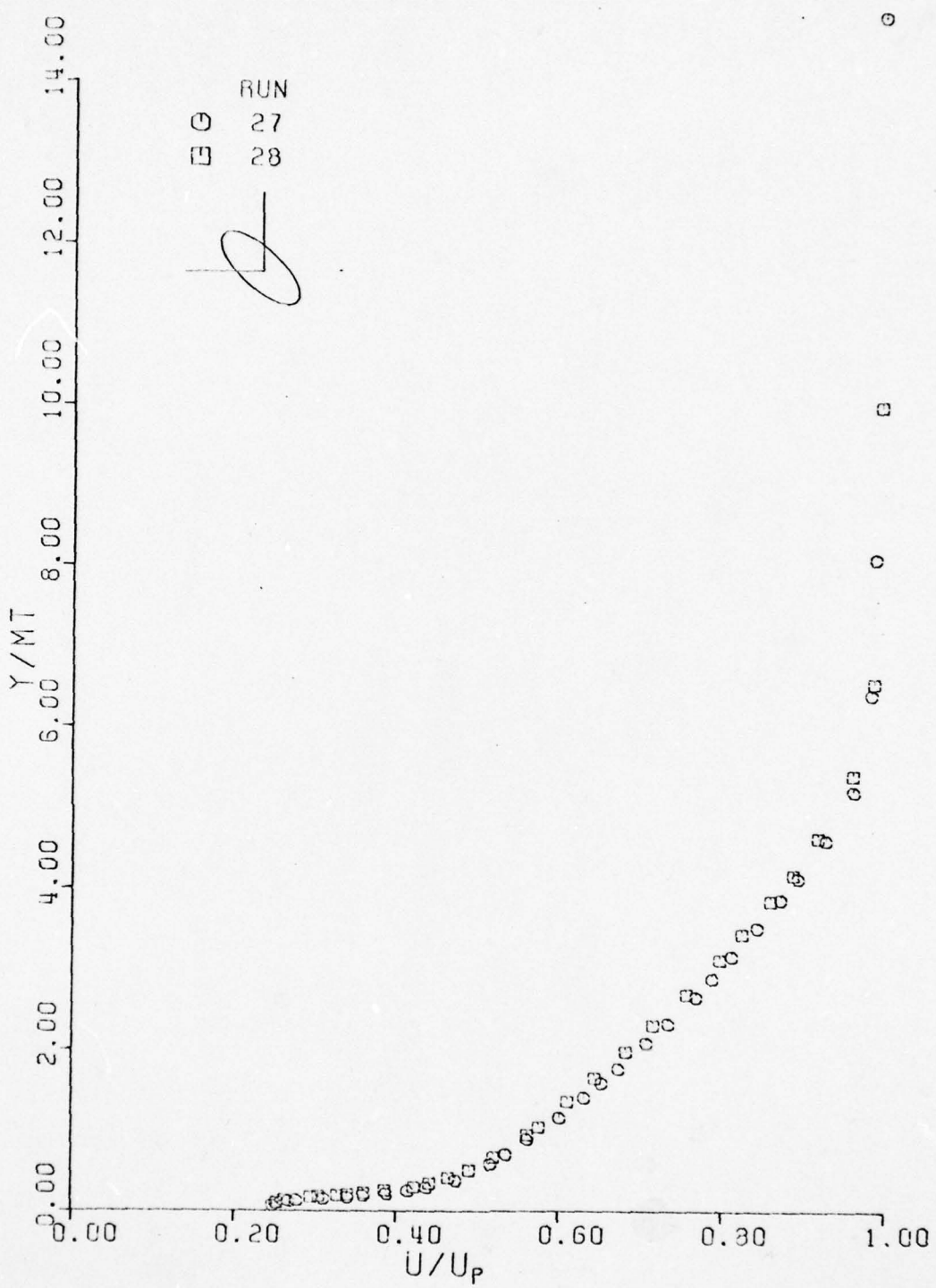


FIG. 26  
NONDIMENSIONAL BOUNDARY LAYER PROFILES  
 $X/C = 0.9380$        $\text{ALPHA} = 45^\circ$

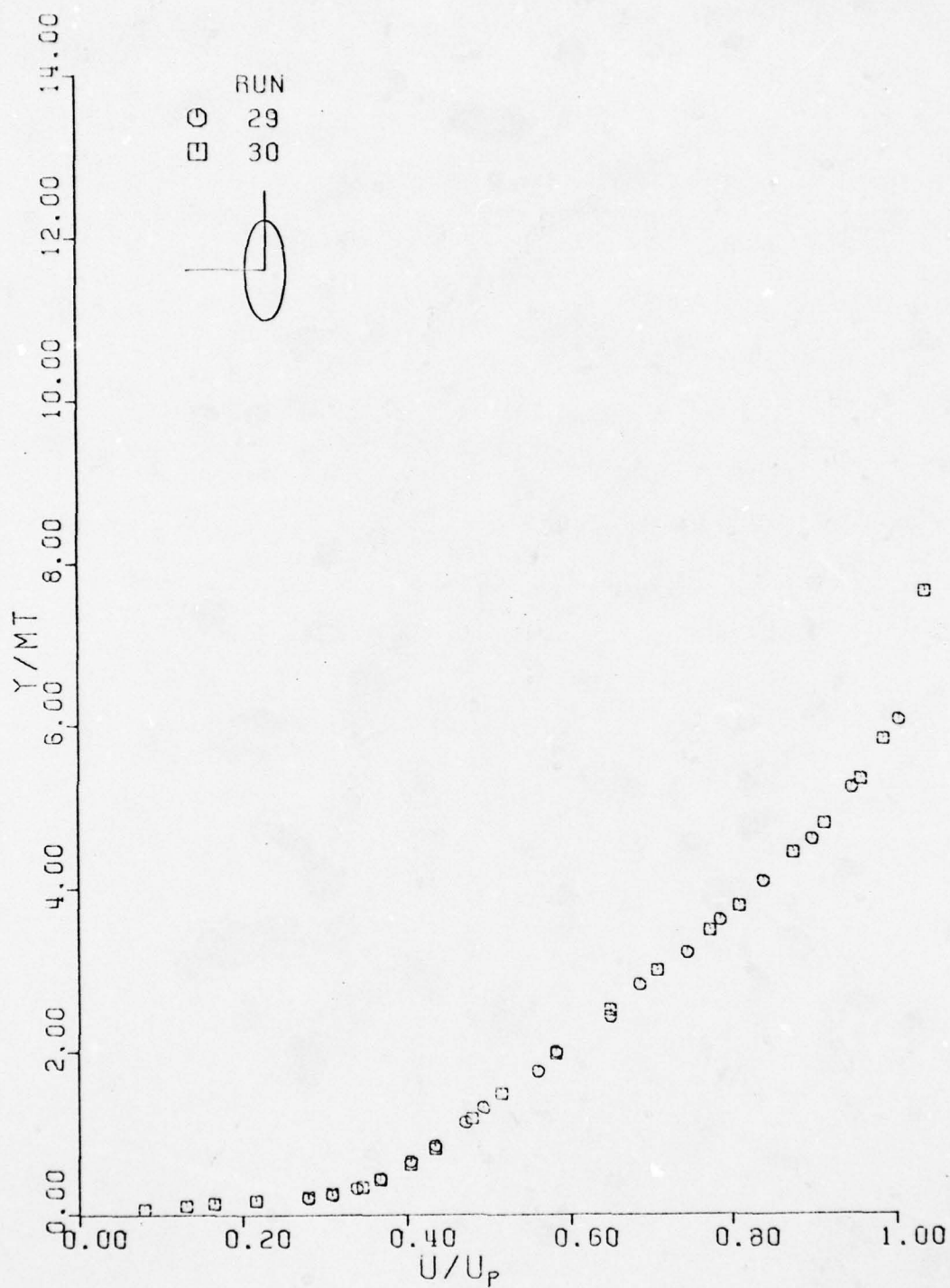


FIG. 27  
NONDIMENSIONAL BOUNDARY LAYER PROFILES  
 $X/C=0.9380$        $\text{ALPHA}=90^\circ$

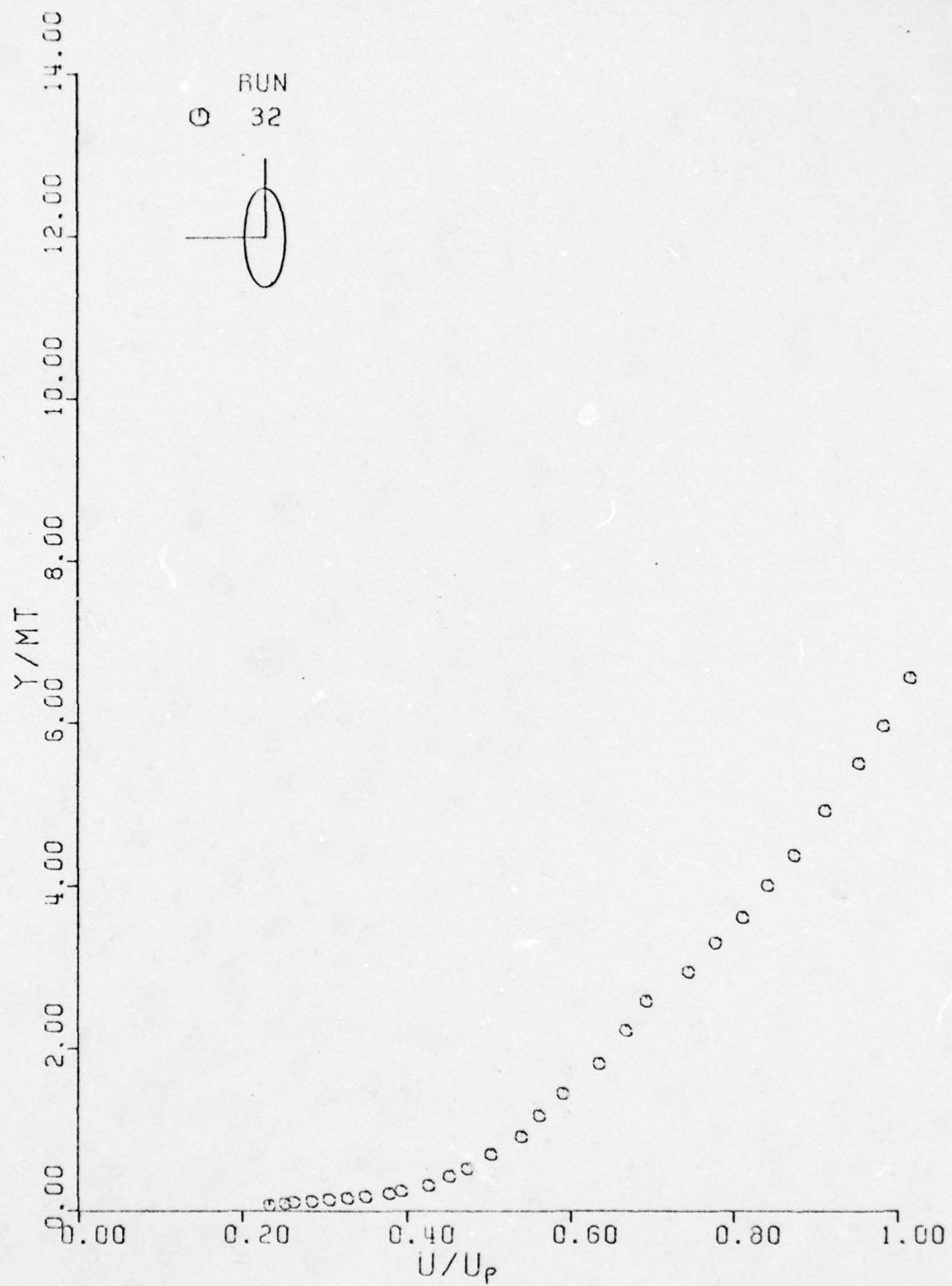


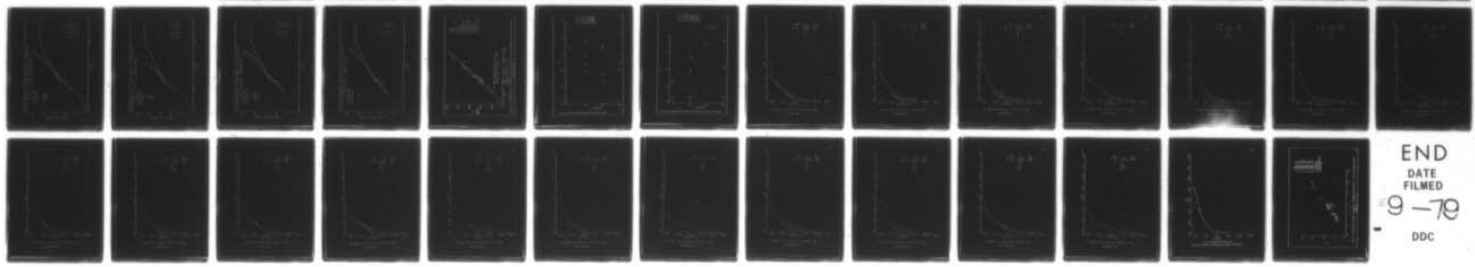
FIG. 28  
NONDIMENSIONAL BOUNDARY LAYER PROFILES  
X/C=0.9380      ALPHA=90 °

AD-A072 839

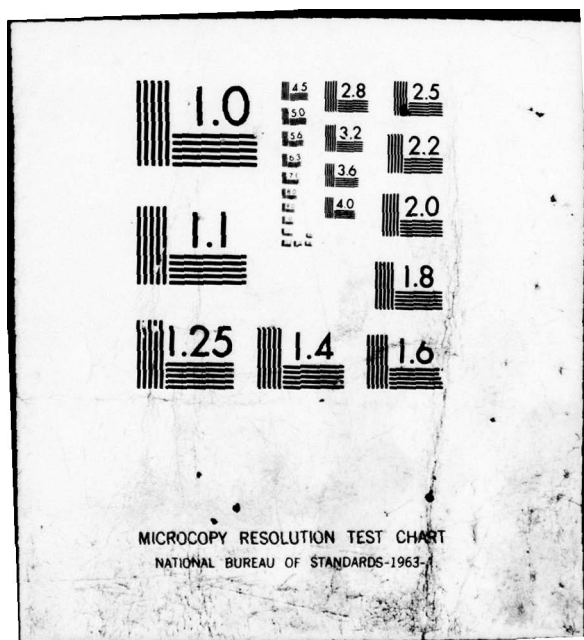
MASSACHUSETTS INST OF TECH CAMBRIDGE AEROPHYSICS LAB F/G 20/4  
TURBULENT BOUNDARY LAYERS ON AN AIRFOIL IN SEVERAL ADVERSE PRES--ETC(U)  
AUG 78 R T CERVISI F49620-77-C-0031  
MIT-TR-203 AFOSR-TR-78-1450 NL

UNCLASSIFIED

2 OF 2  
AD  
A072839  
REC  
100%



END  
DATE  
FILMED  
9-78  
DDC



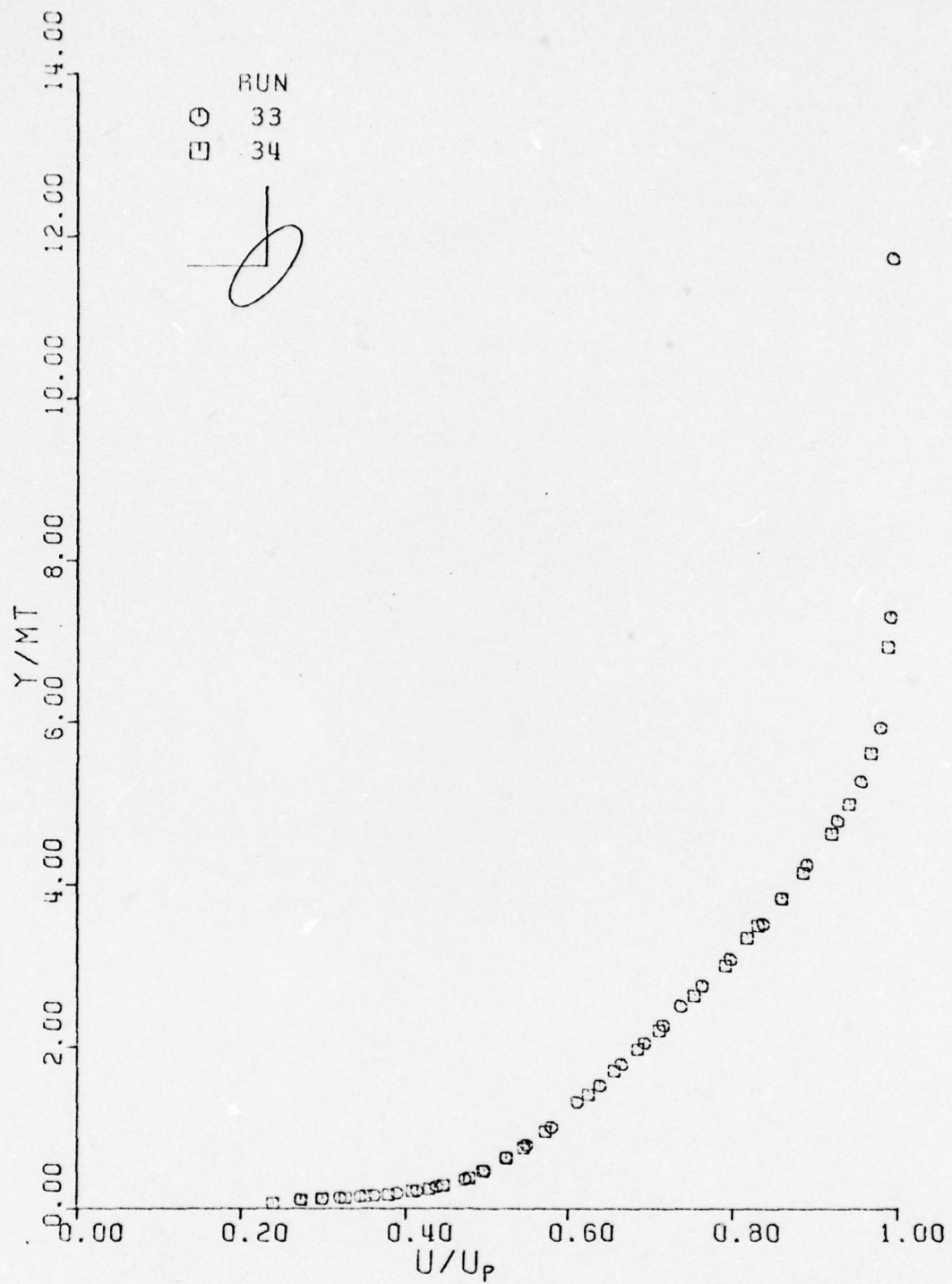


FIG. 29  
NONDIMENSIONAL BOUNDARY LAYER PROFILES  
 $X/C = 0.9380$      $\text{ALPHA} = 135^\circ$

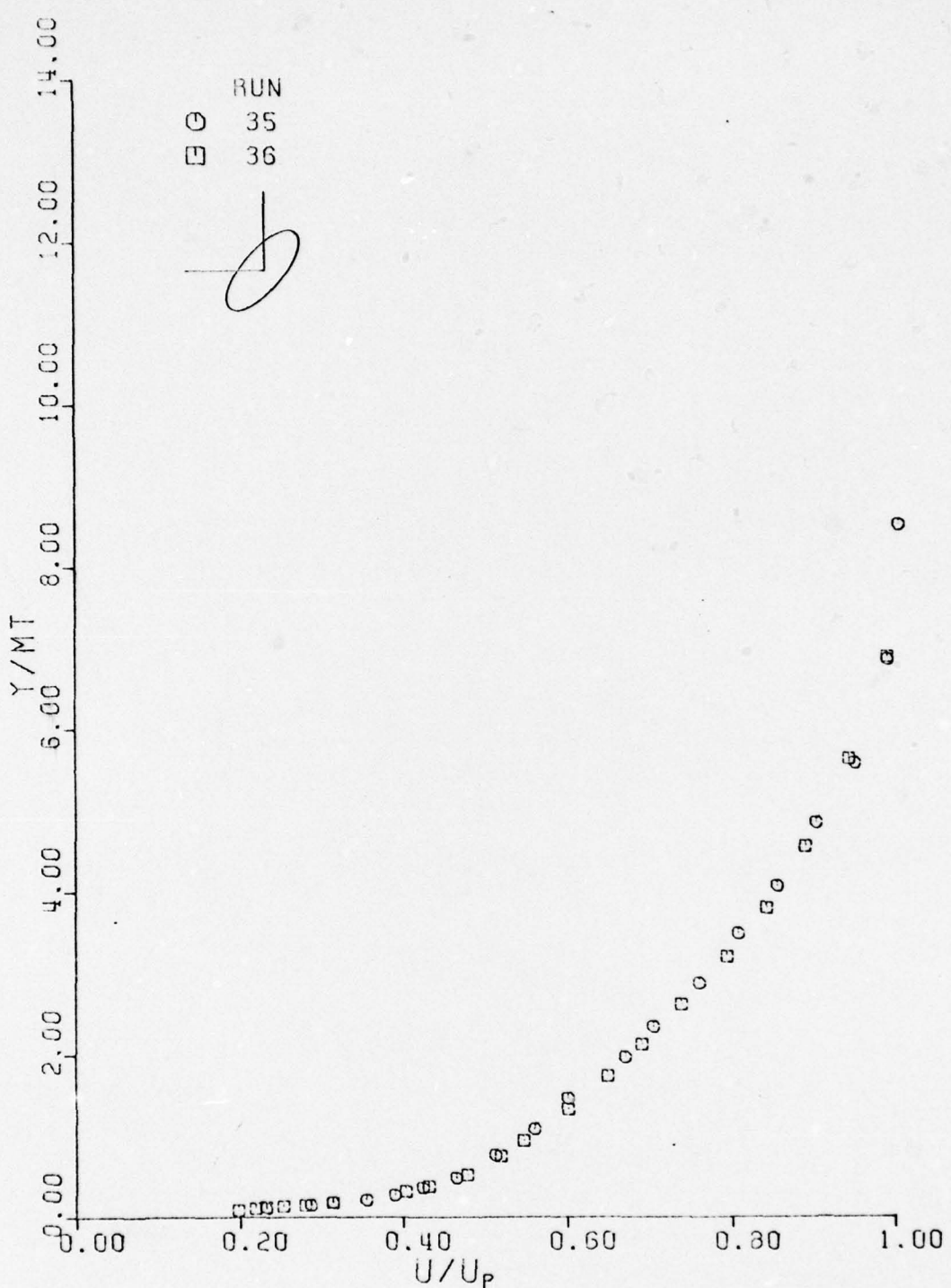


FIG.30

NONDIMENSIONAL BOUNDARY LAYER PROFILES

$X/C = 0.9380$        $\text{ALPHA} = 135^\circ$

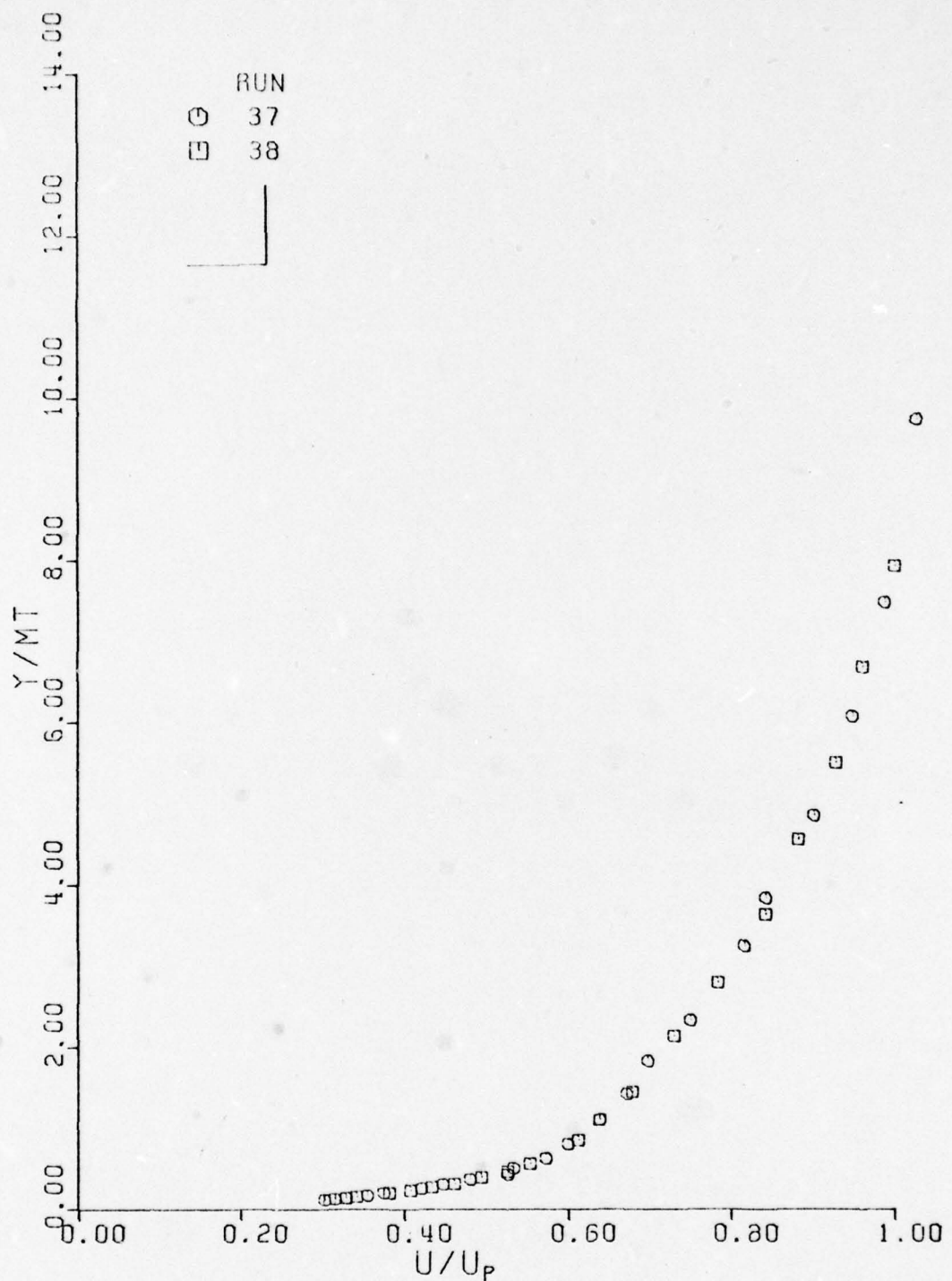


FIG.31

NONDIMENSIONAL BOUNDARY LAYER PROFILES

$X/C = 0.9380$        $\text{ALPHA} = 0^\circ$

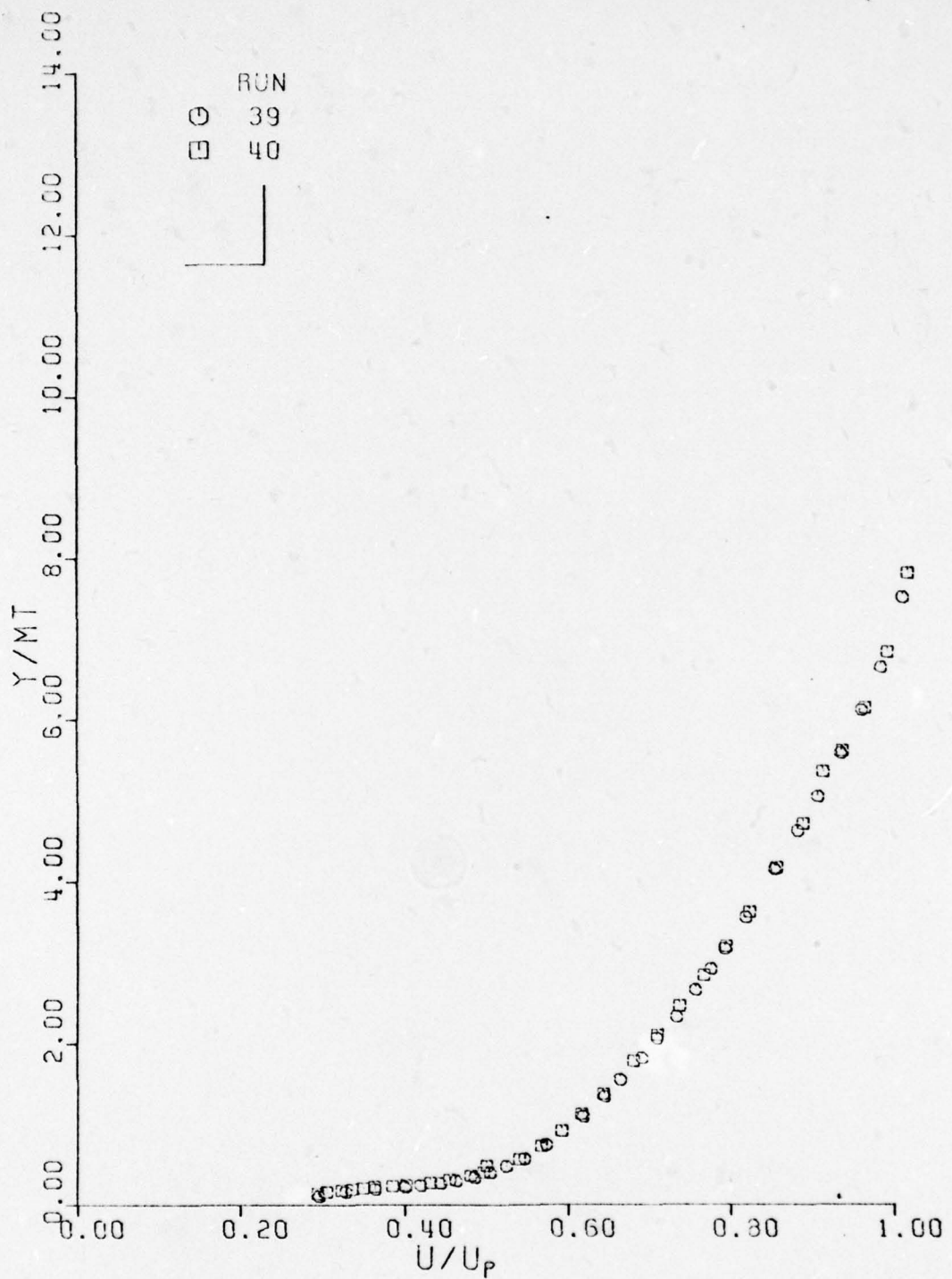


FIG.32  
NONDIMENSIONAL BOUNDARY LAYER PROFILES  
 $X/C=0.9380$        $\text{ALPHA}=NO^{\circ}$

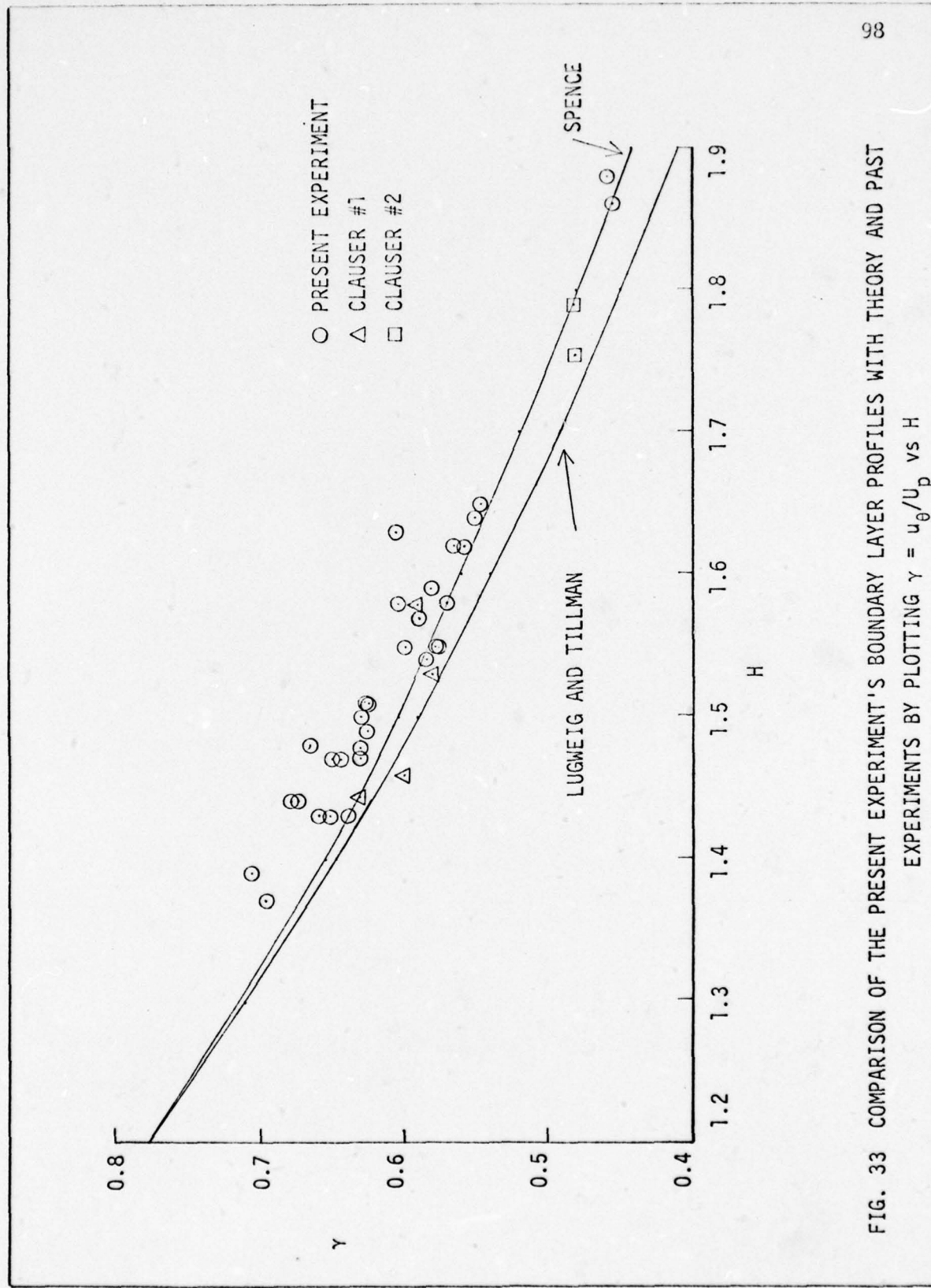


FIG. 33 COMPARISON OF THE PRESENT EXPERIMENT'S BOUNDARY LAYER PROFILES WITH THEORY AND PAST EXPERIMENTS BY PLOTTING  $\gamma = u_\theta / U_p$  vs  $H$

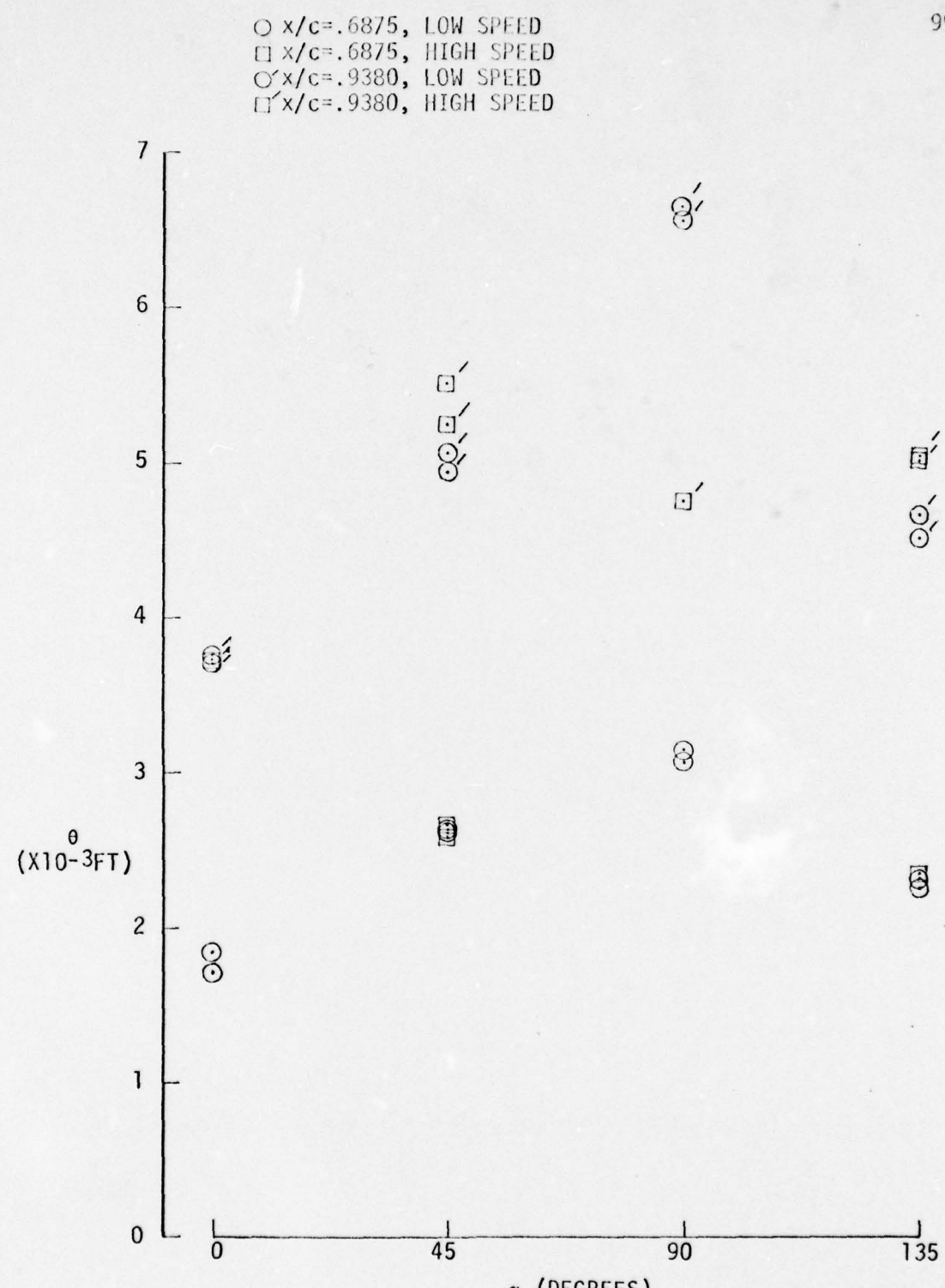


FIG. 34 MOMENTUM THICKNESS VS. ELLIPSE ANGLE

FIG.35 BOUNDARY LAYER PROFILES IN MODIFIED  
LAW OF THE WALL COORDINATES

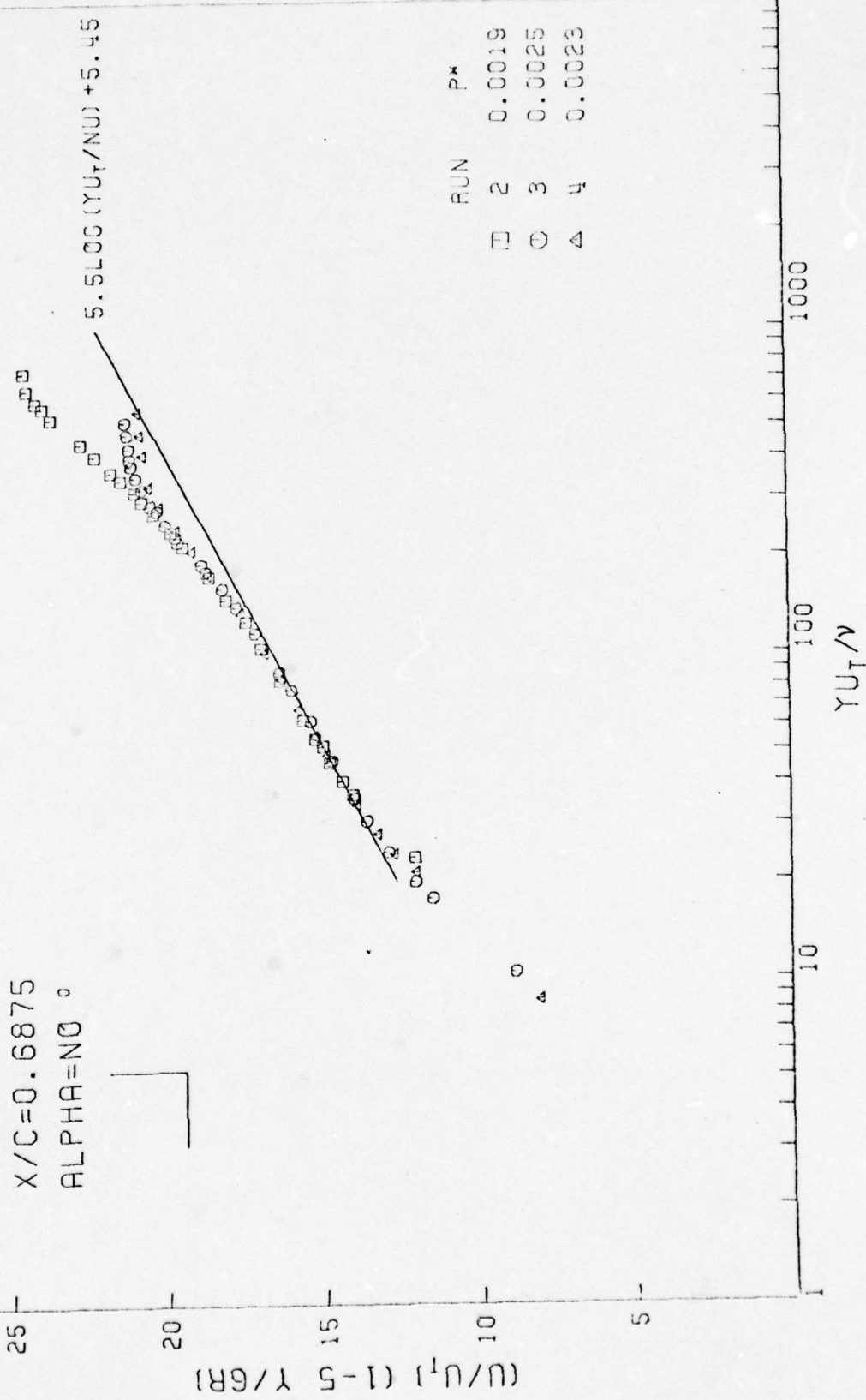


FIG. 36 BOUNDARY LAYER PROFILES IN MODIFIED  
LAW OF THE WALL COORDINATES

$X/C = 0.6875$   
 $\alpha = 0$

$$S = SUG (\gamma u_t / \nu) + 5.45$$

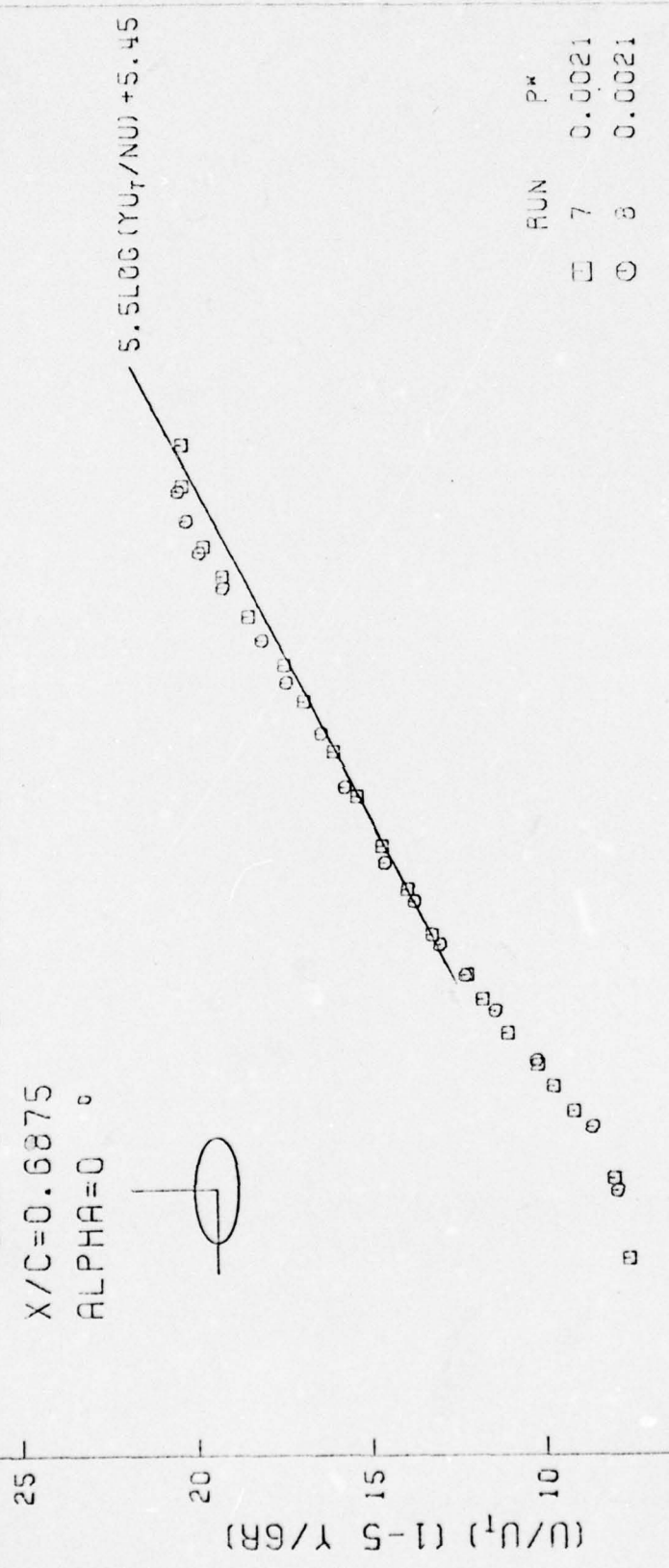


FIG. 37 BOUNDARY LAYER PROFILES IN MODIFIED  
LAW OF THE WALL COORDINATES

$X/C = 0.6875$   
 $\text{ALPHA} = 45^\circ$

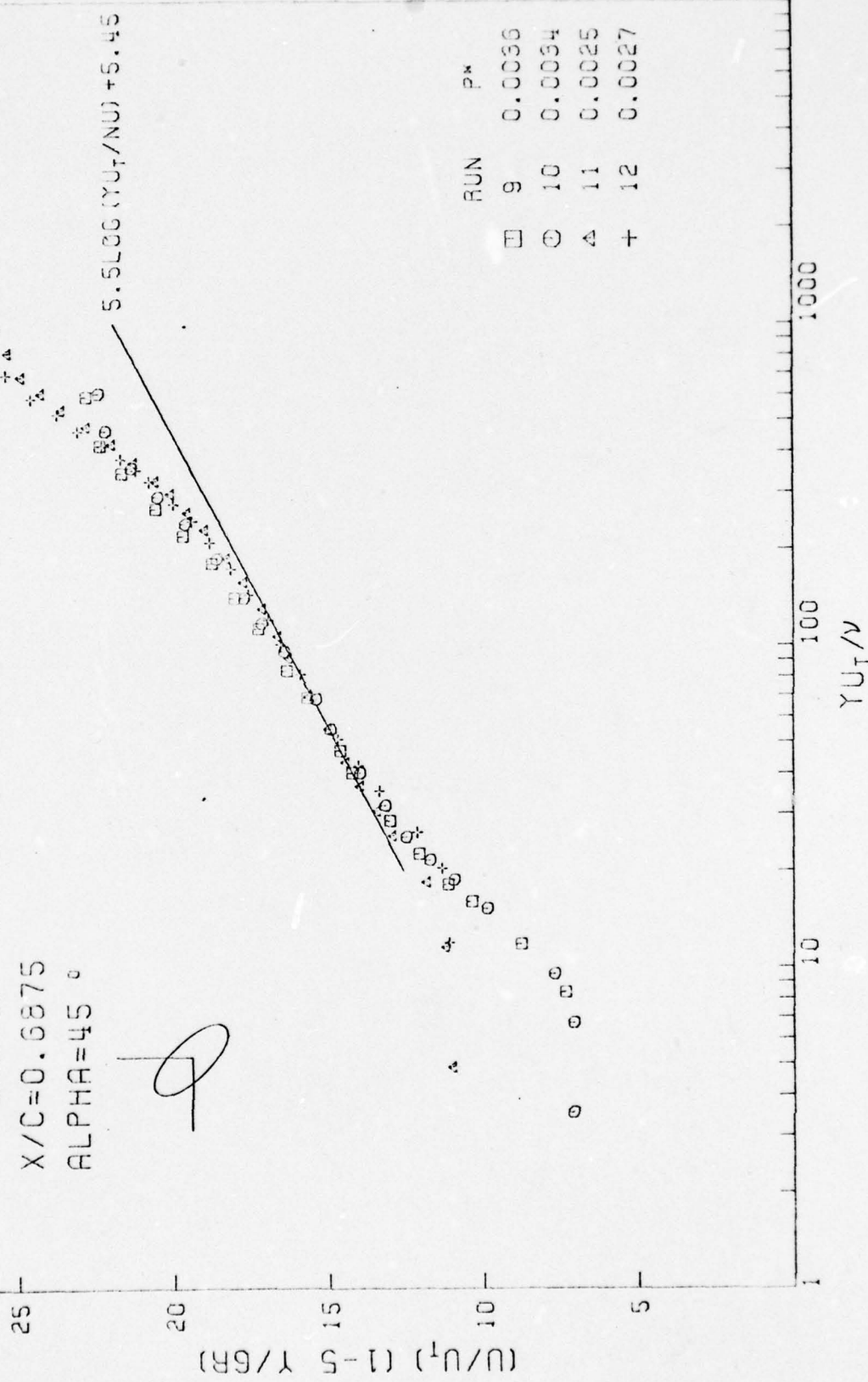
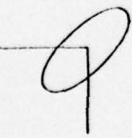


FIG. 38 BOUNDARY LAYER PROFILES IN MODIFIED  
LAW OF THE WALL COORDINATES

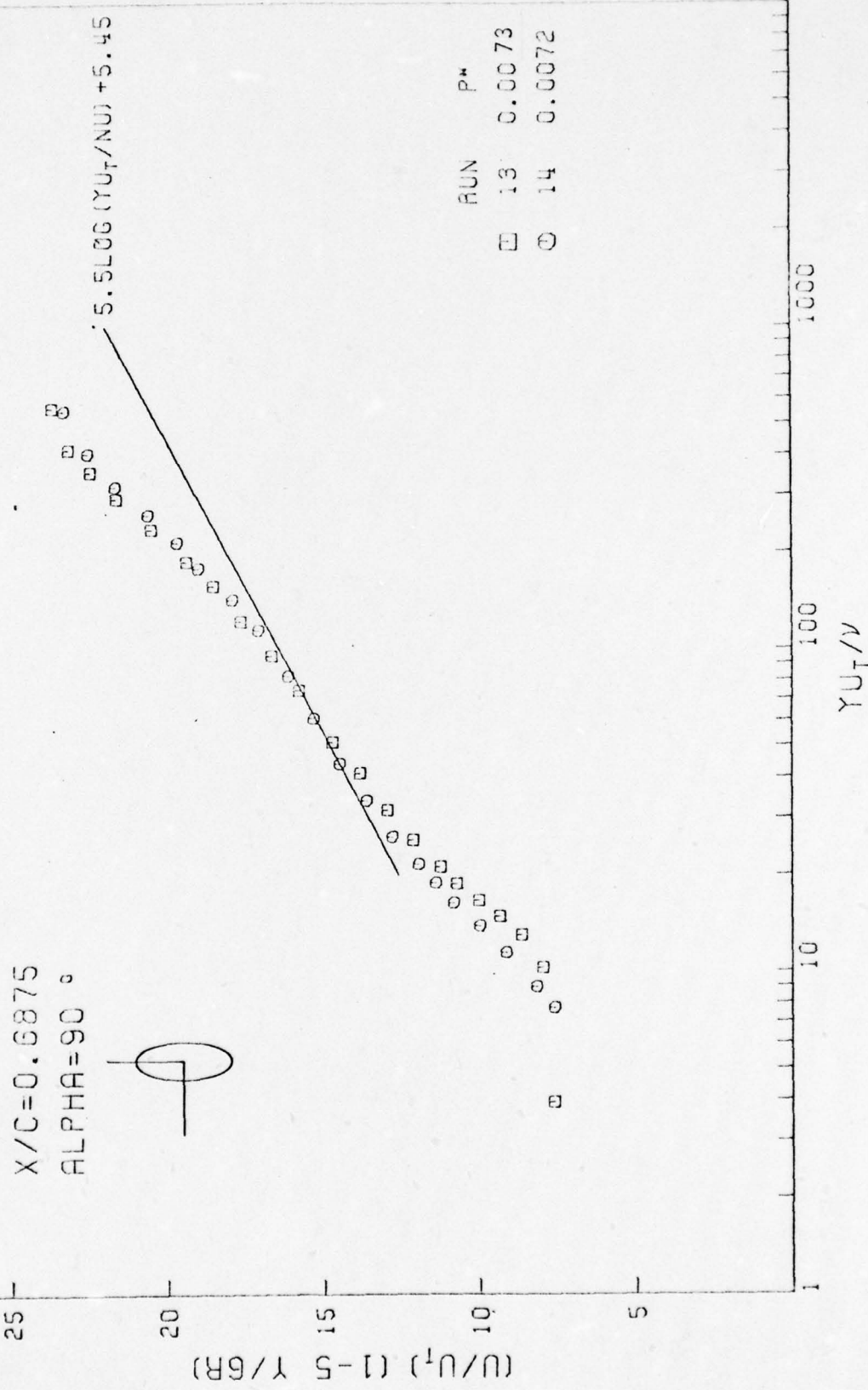


FIG.39 BOUNDARY LAYER PROFILES IN MODIFIED  
LAW OF THE WALL COORDINATES

$X/C = 0.6875$

$\text{ALPHA} = 135^\circ$

5. SLUG ( $YU_T/V$ ) + 5.45



25

$(U/U_T) (1 - 5 Y/CR)$

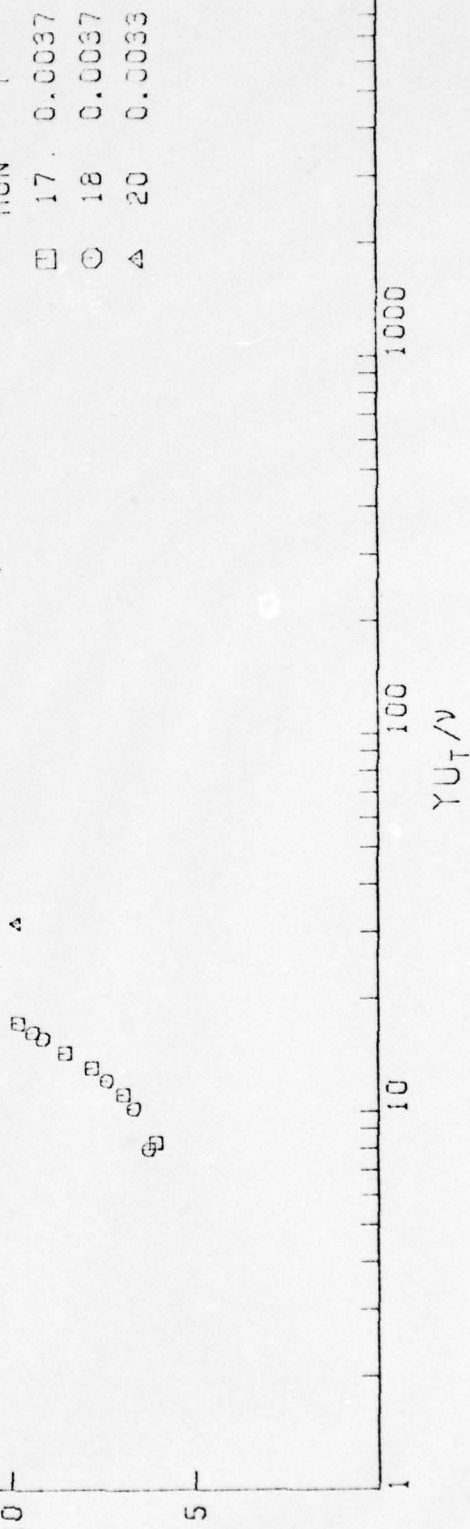


FIG.40 BOUNDARY LAYER PROFILES IN MODIFIED  
LAW OF THE WALL COORDINATES

$X/C = 0.9380$   
 $\alpha = 0^\circ$

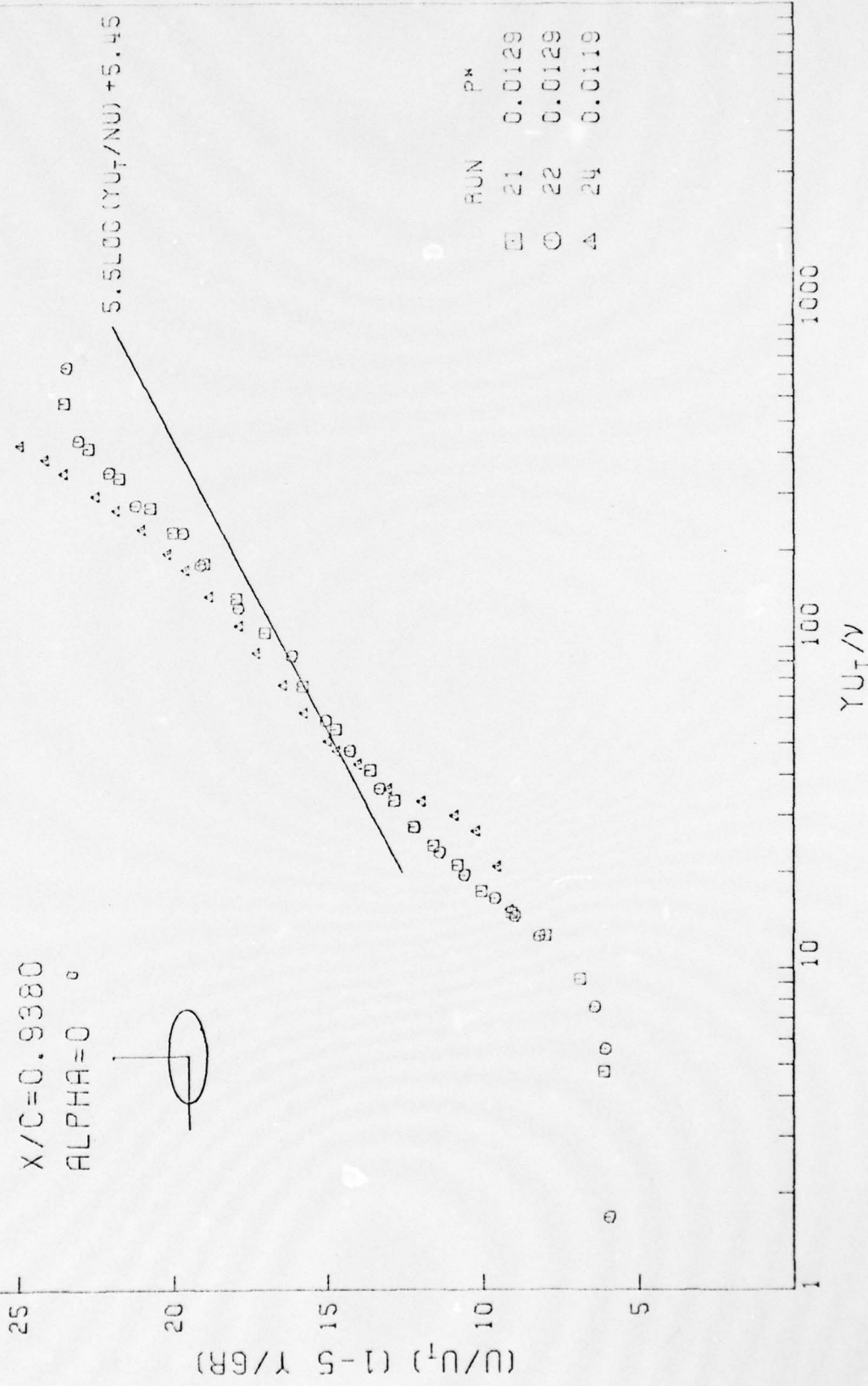
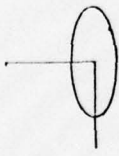


FIG.41 BOUNDARY LAYER PROFILES IN MODIFIED  
LAW OF THE WALL COORDINATES

$X/C = 0.9380$

$\text{ALPHA} = 45^\circ$

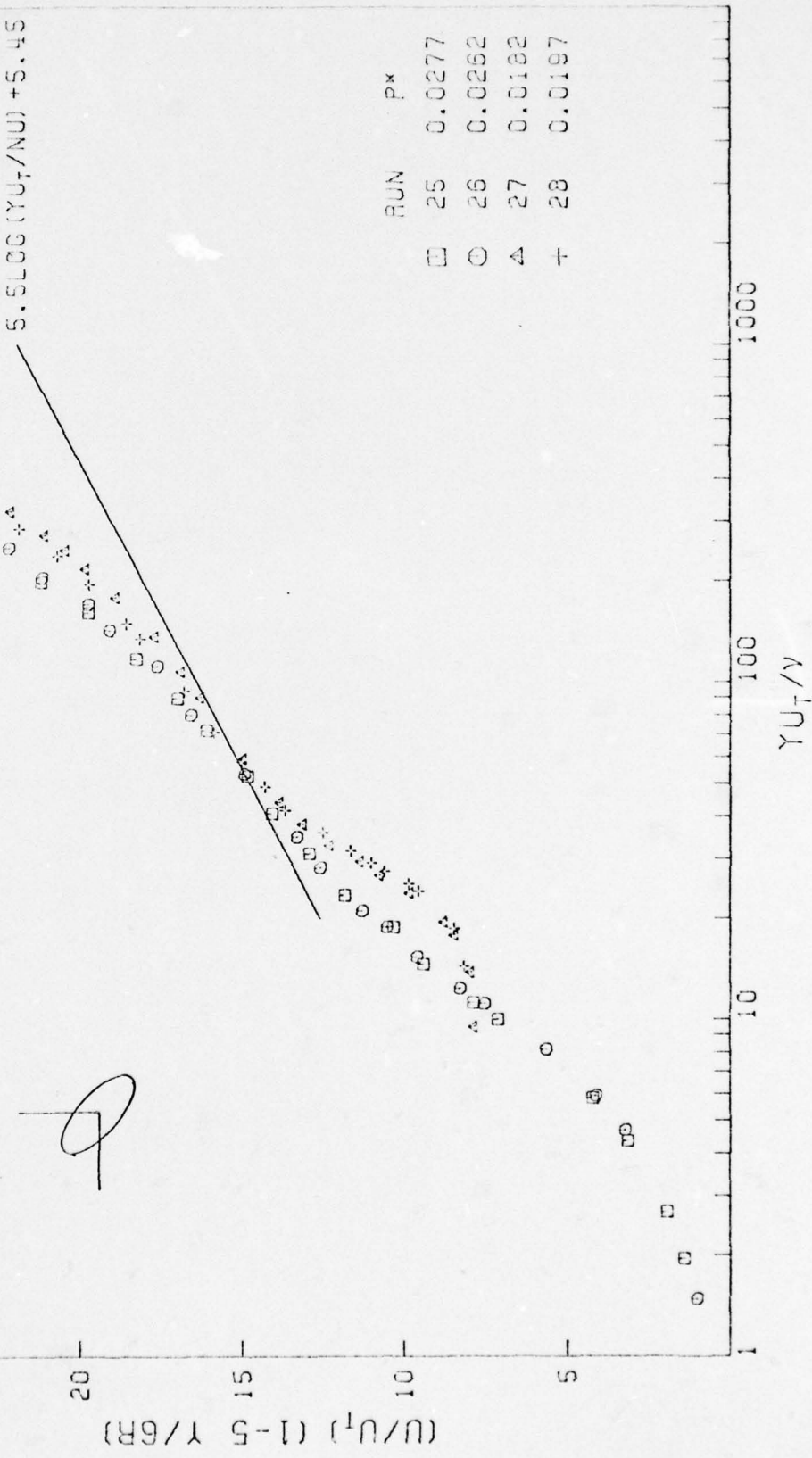


FIG. 4.2 BOUNDARY LAYER PROFILES IN MODIFIED  
LAW OF THE WALL COORDINATES

$X/C = 0.9380$   
 $\text{ALPHA} = 90^\circ$



$(U/U_T) (1 - 5 \gamma/6\Gamma)$

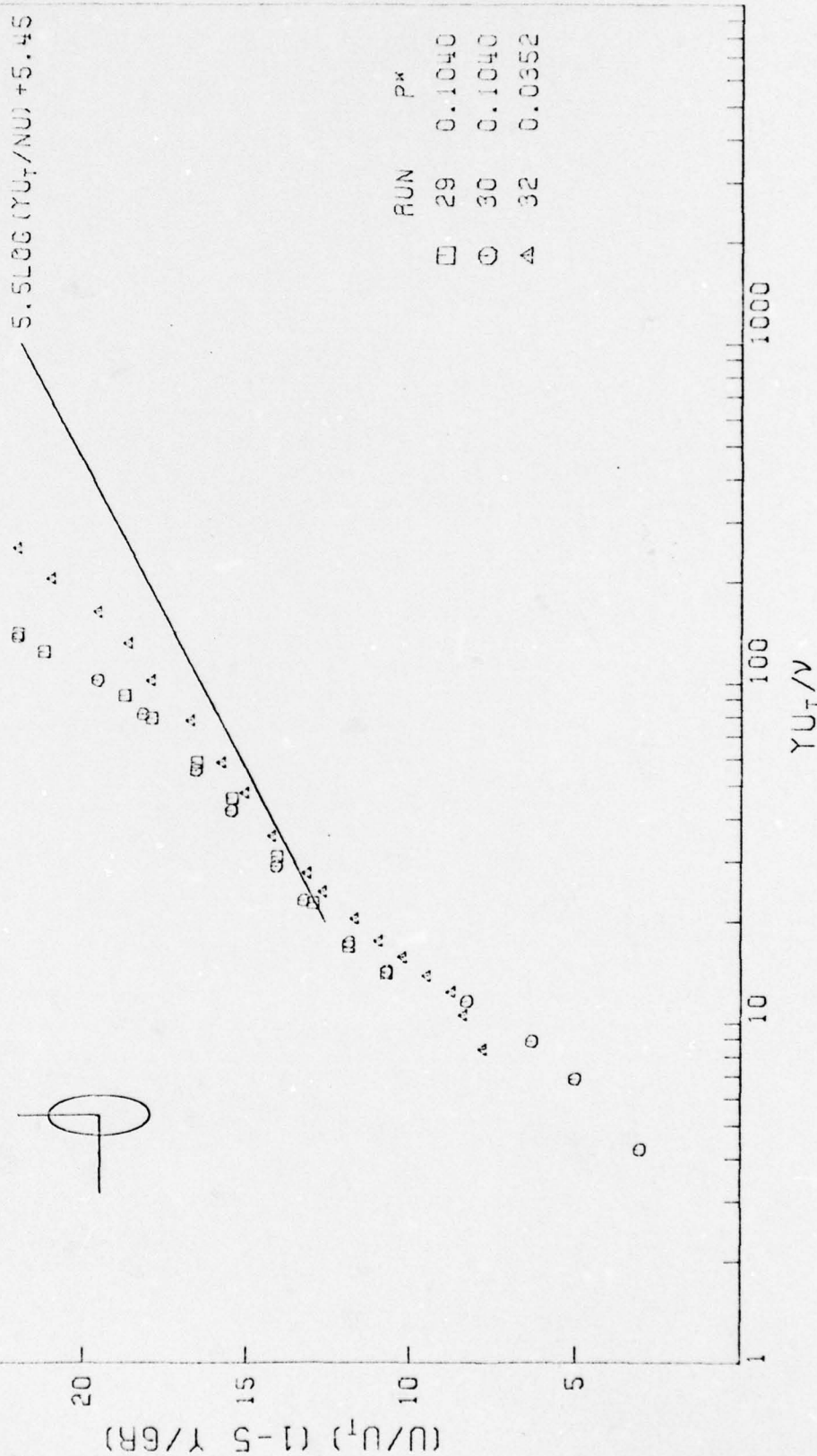


FIG.4.3 BOUNDARY LAYER PROFILES IN MODIFIED LAW OF THE WALL COORDINATES

$X/C = 0.9380$   
 $\text{ALPHA} = 135^\circ$

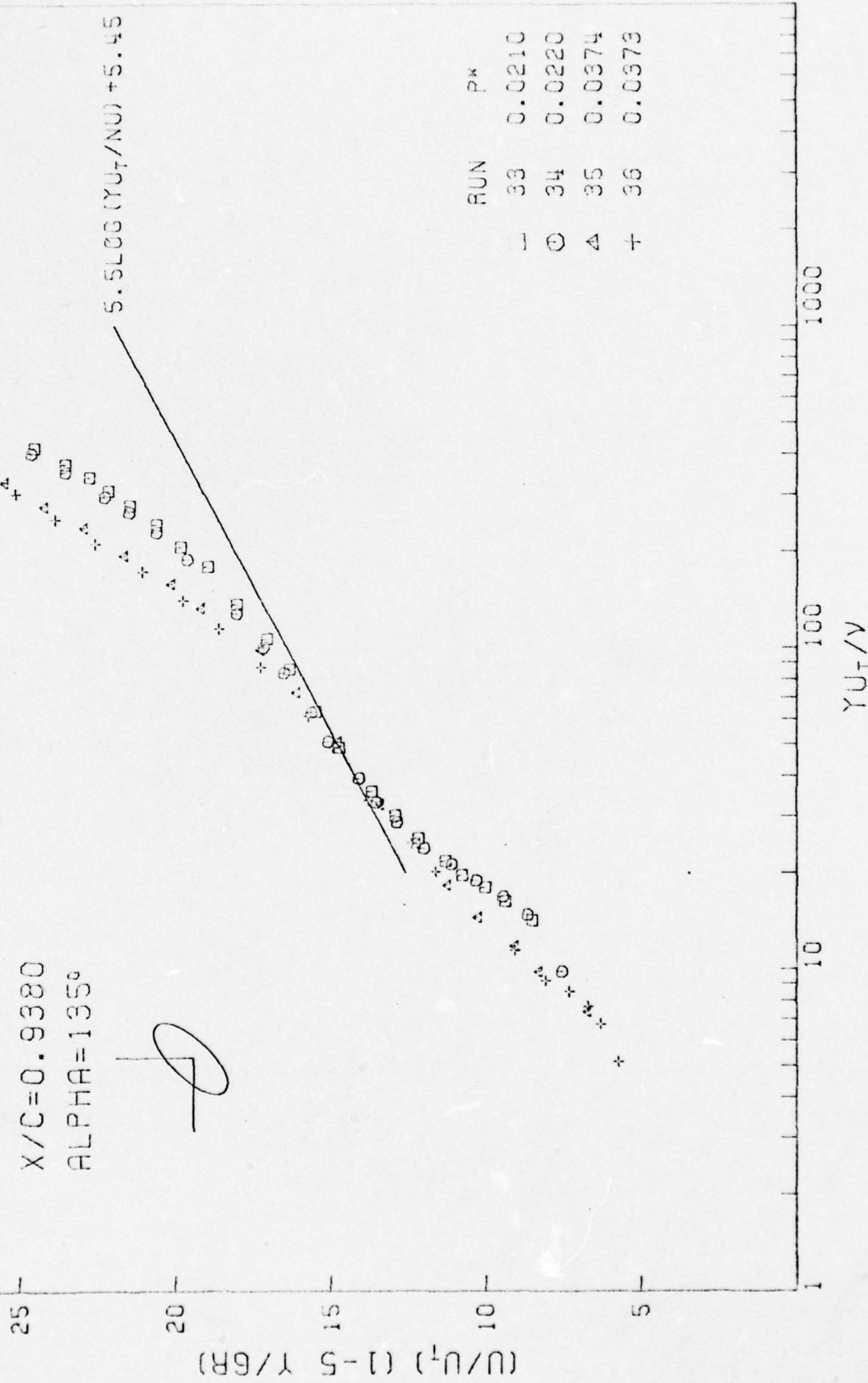
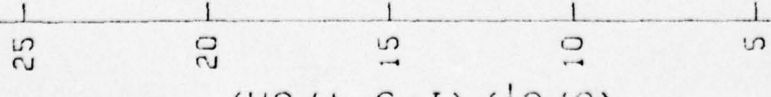


FIG.44 BOUNDARY LAYER PROFILES IN MODIFIED  
LAW OF THE WALL COORDINATES

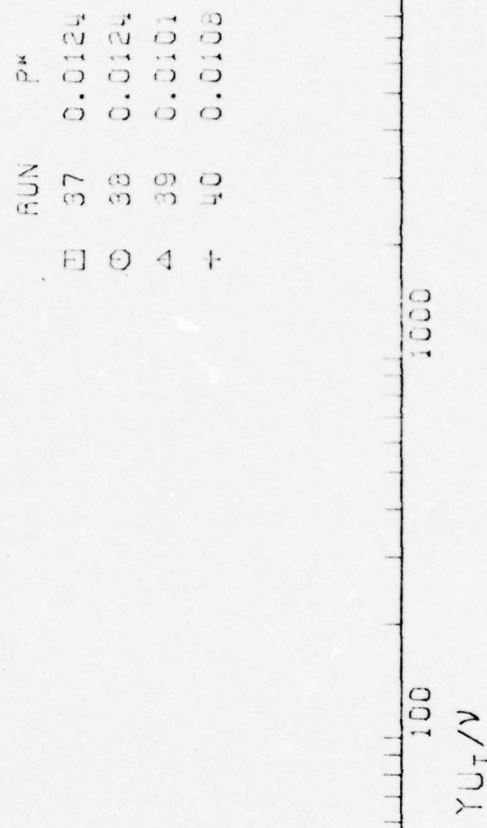
$X/C = 0.9380$

$\text{ALPHA} = \text{NG}^0$

$$5.5 \log (\gamma U_T / \nu) + 5.45$$

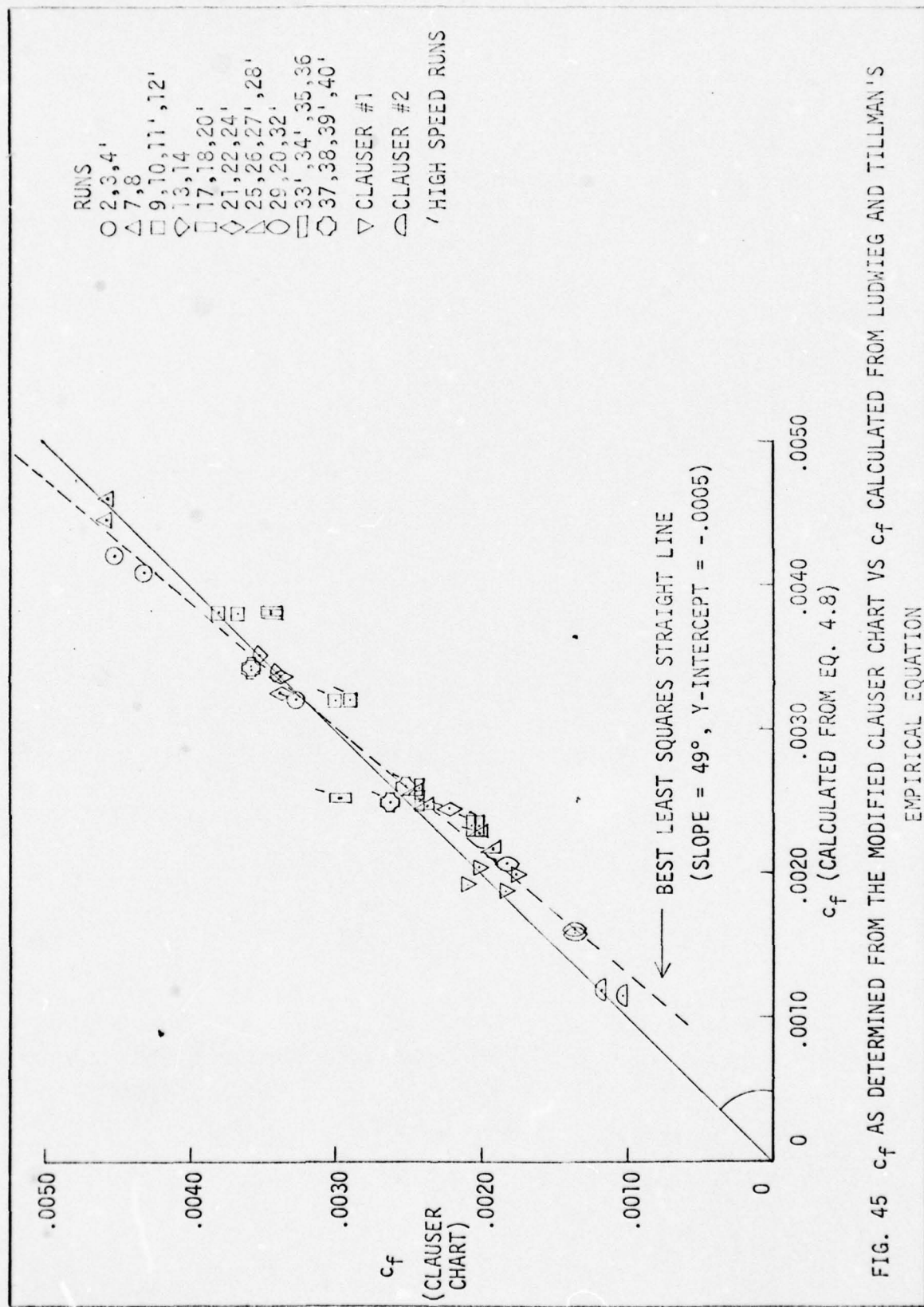


$$(U/U_T) (1 - 5 Y/6R)$$



$$\text{RUN} \quad P^*$$

37	0.0124
38	0.0124
41	0.0101
40	0.0108



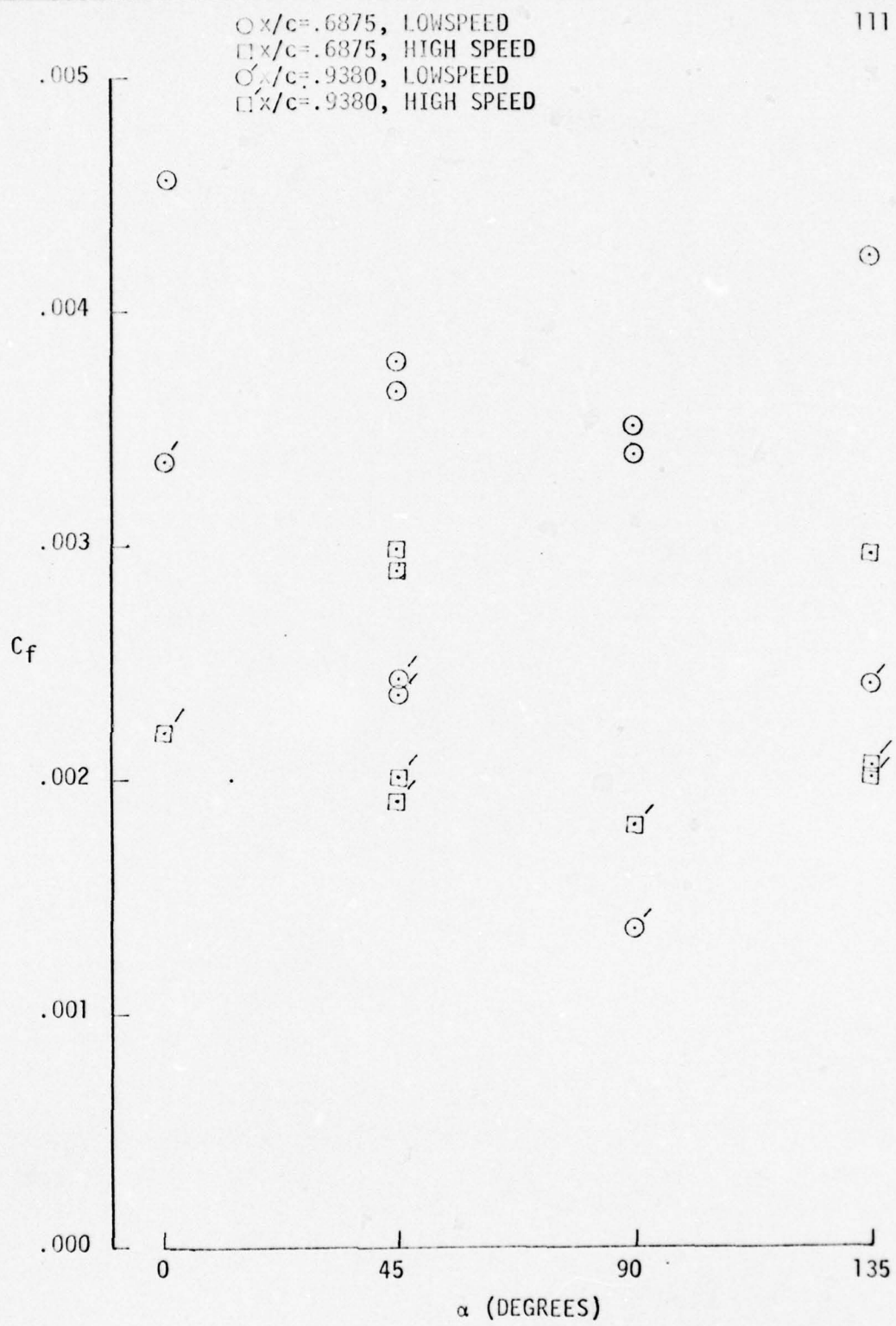


FIG.46 THE LOCAL SKIN COEFFICIENT VS. ELLIPSE ANGLE

○  $x/c = .6875$ , LOW SPEED  
 □  $x/c = .6875$ , HIGH SPEED  
 ○  $x/c = .9380$ , LOW SPEED  
 □  $x/c = .9380$ , HIGH SPEED

112

$\uparrow \phi' .1040$

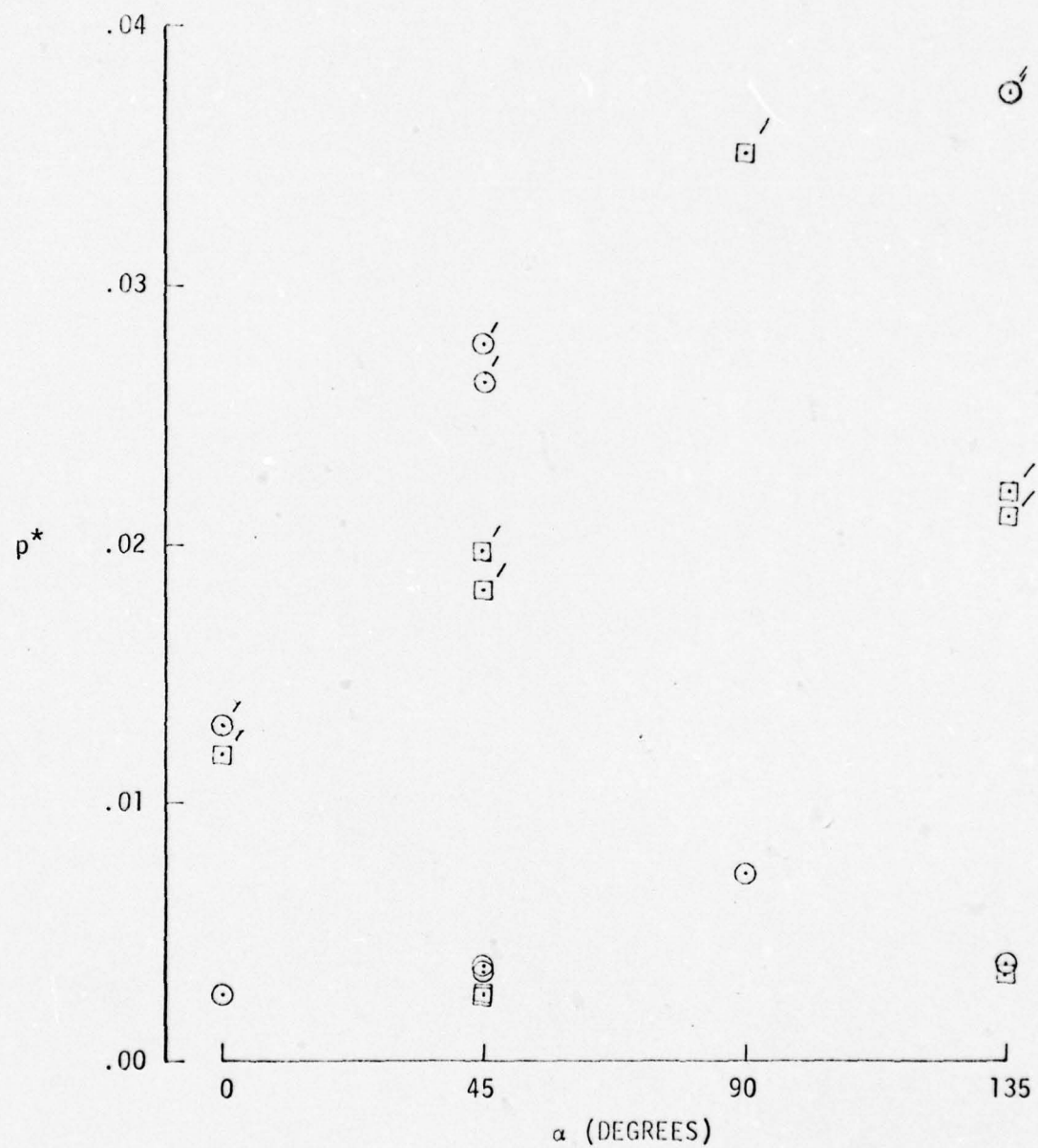


FIG.47 THE NONDIMENSIONAL PRESSURE GRADIENT ( $p^*$ ) VS. ELLIPSE ANGLE

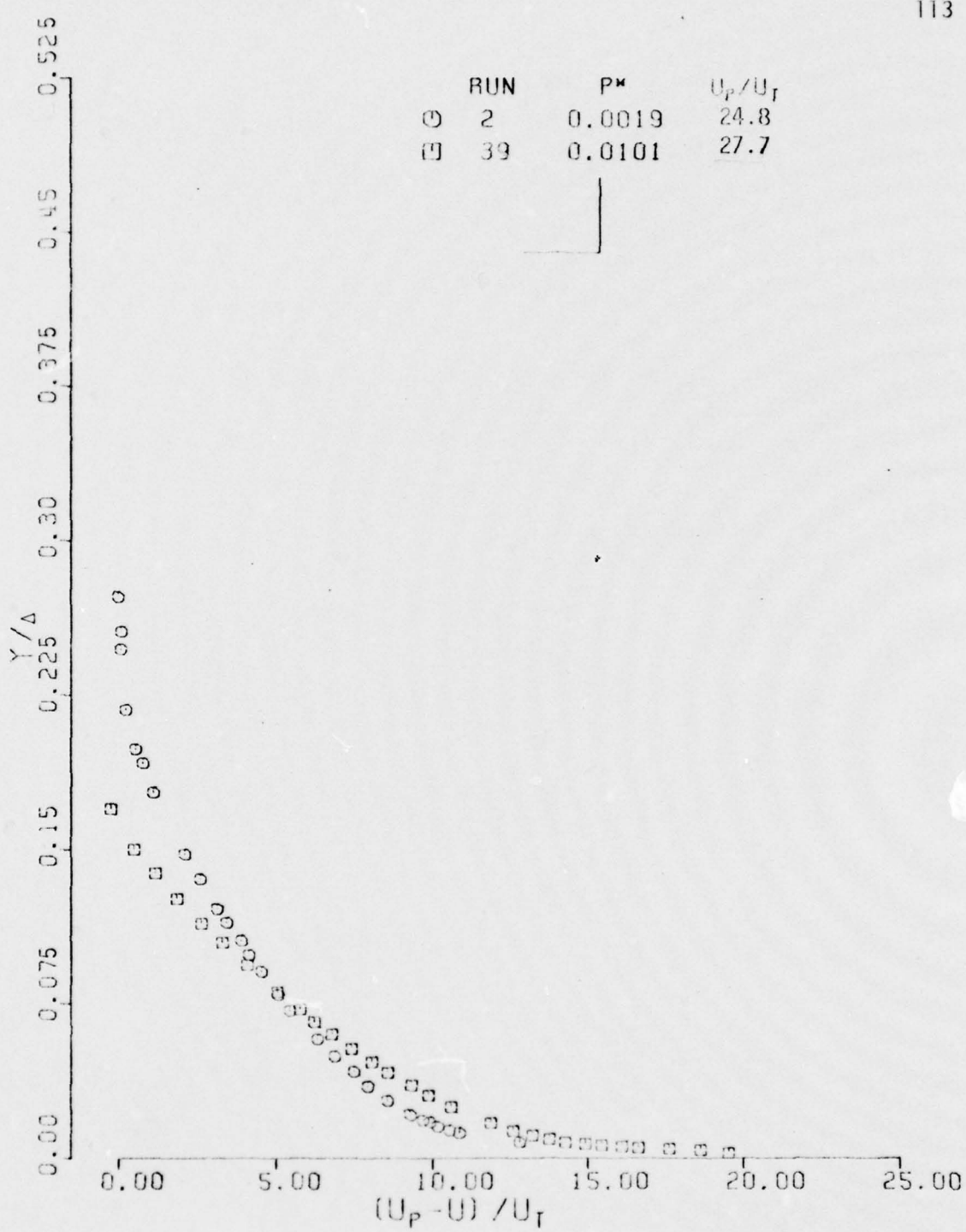


FIG. 48 THE VELOCITY DEFECT LAW

ALPHA=NO °

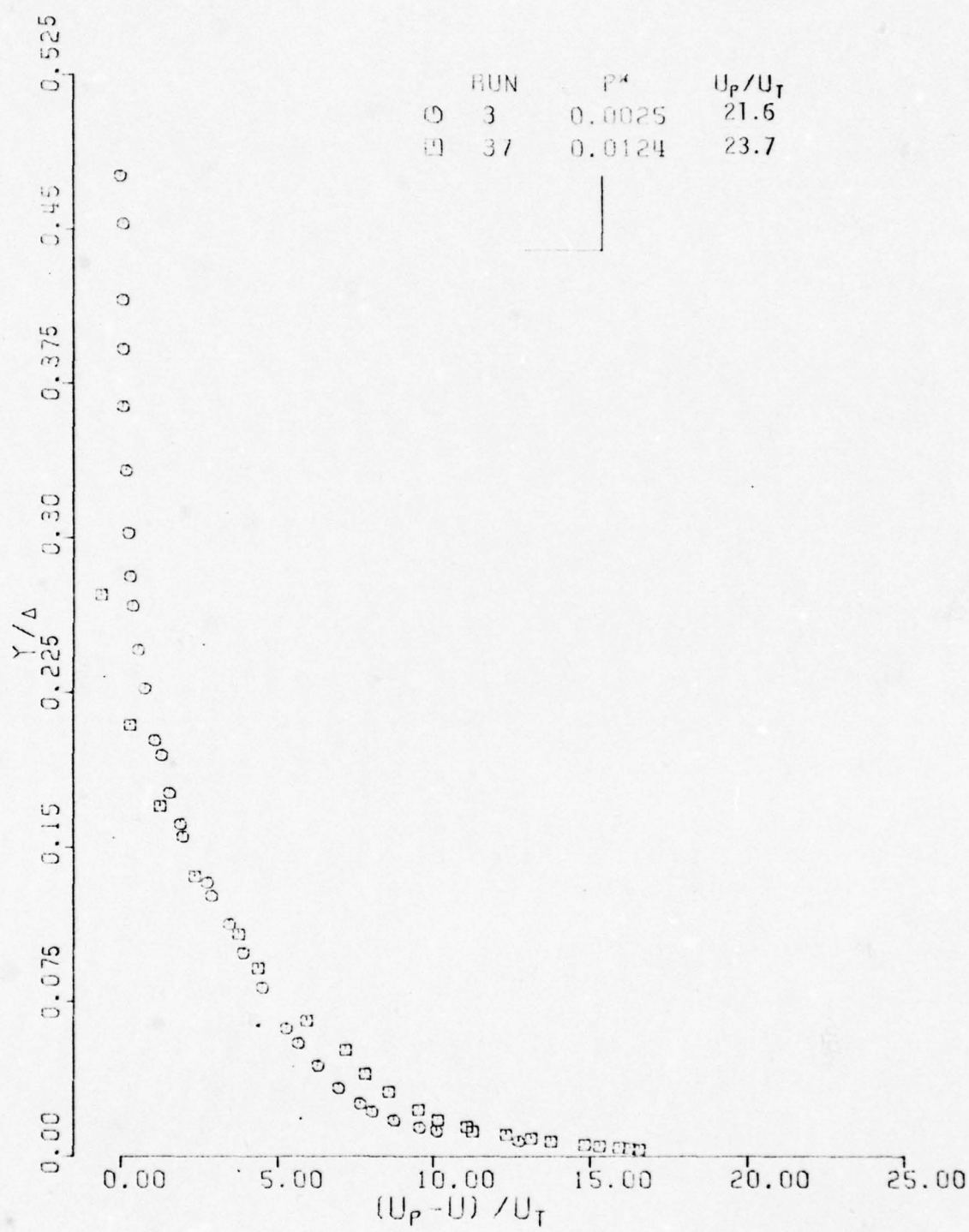


FIG.49 THE VELOCITY DEFECT LAW  
ALPHA=NO °

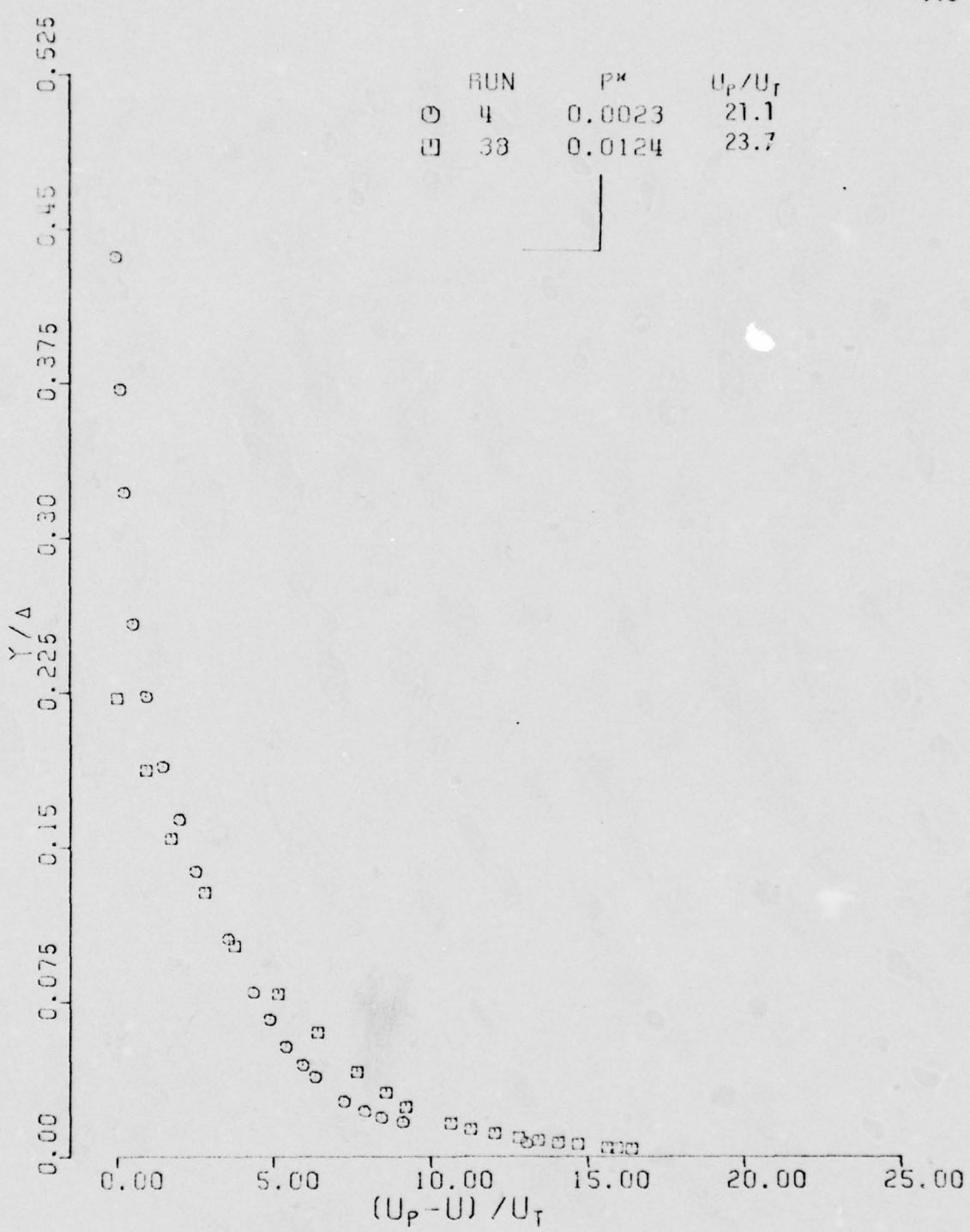


FIG.50 THE VELOCITY DEFECT LAW

ALPHA=NO °

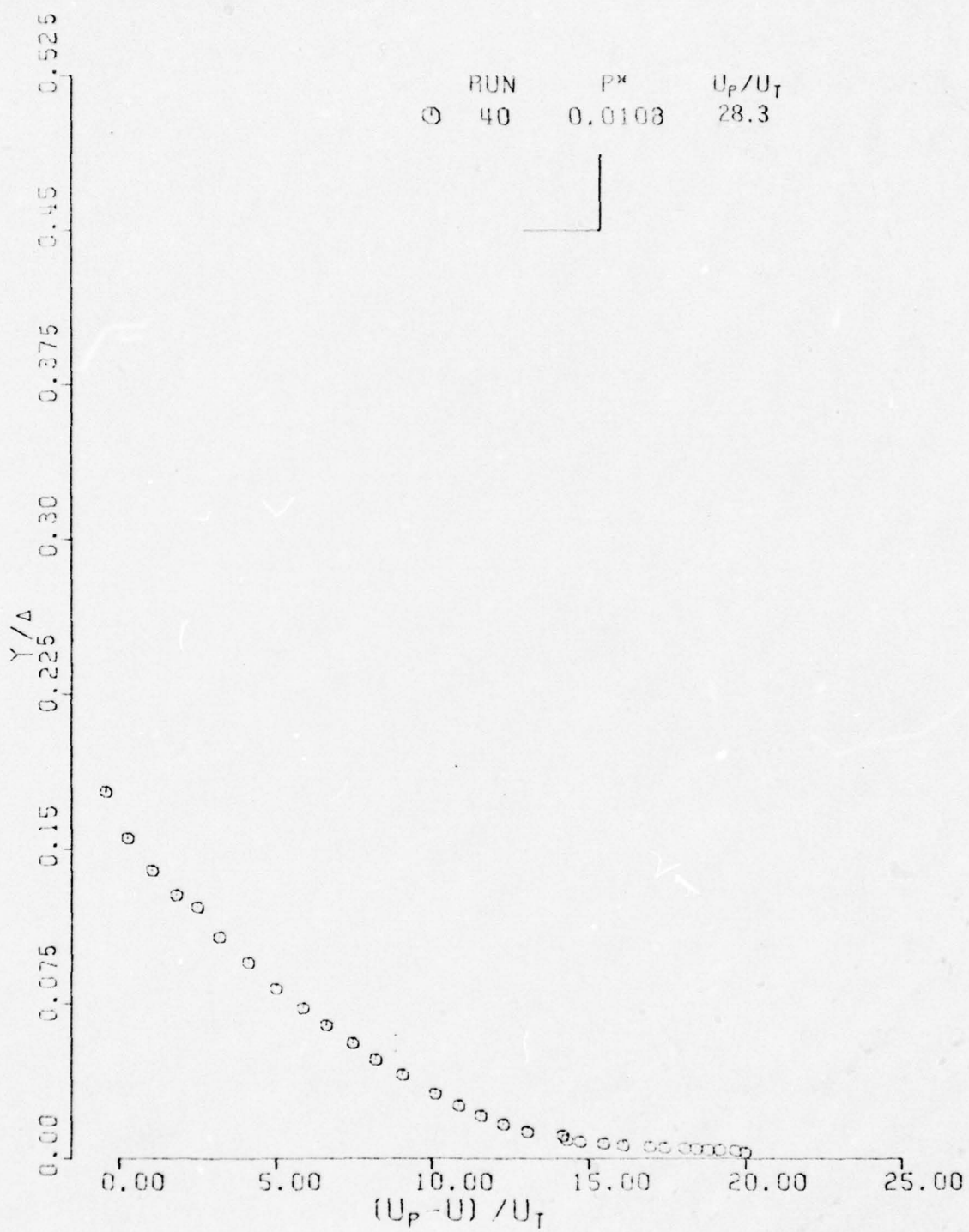


FIG.5f THE VELOCITY DEFECT LAW

ALPHA=NO °

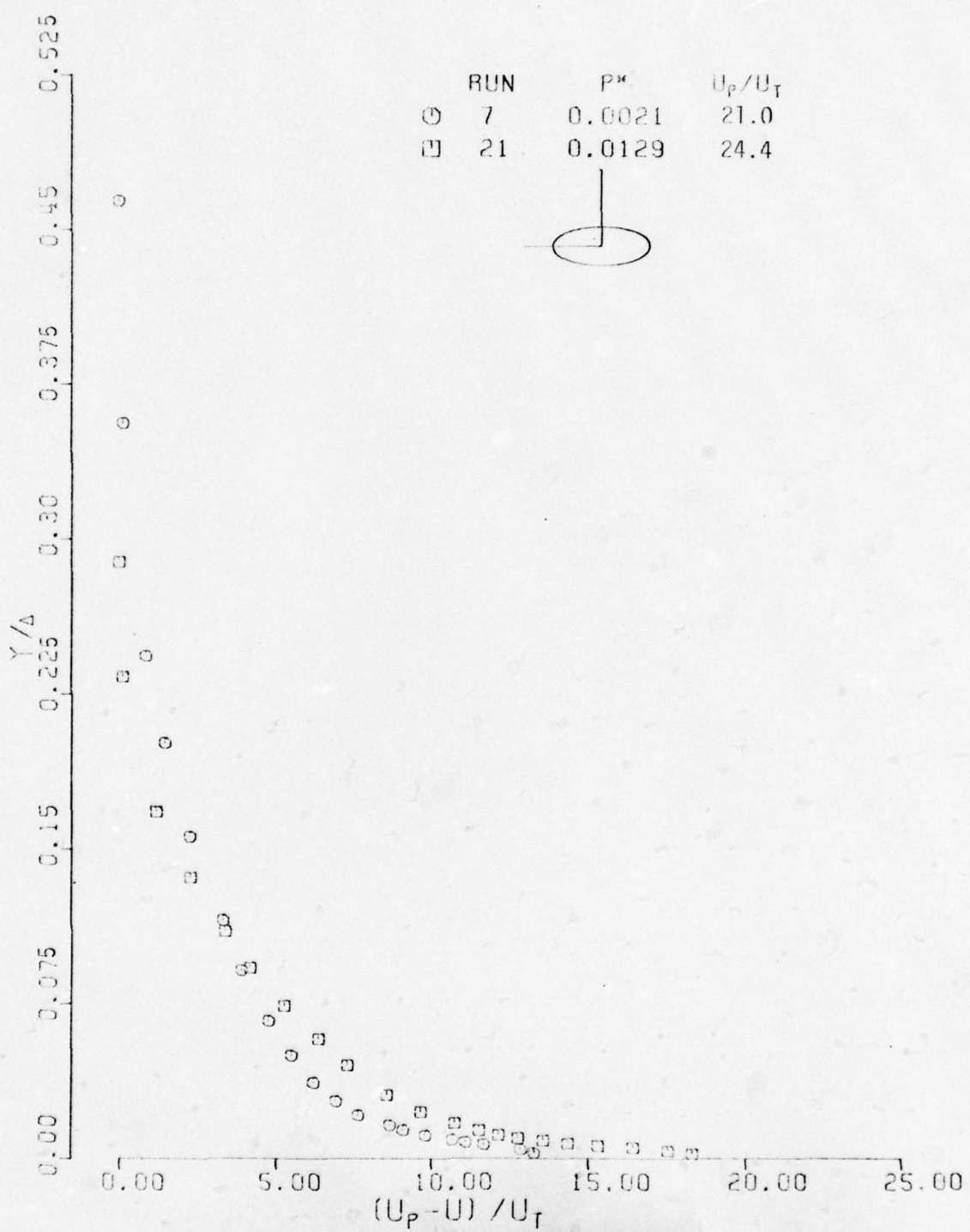


FIG.52 THE VELOCITY DEFECT LAW  
ALPHA=0 °

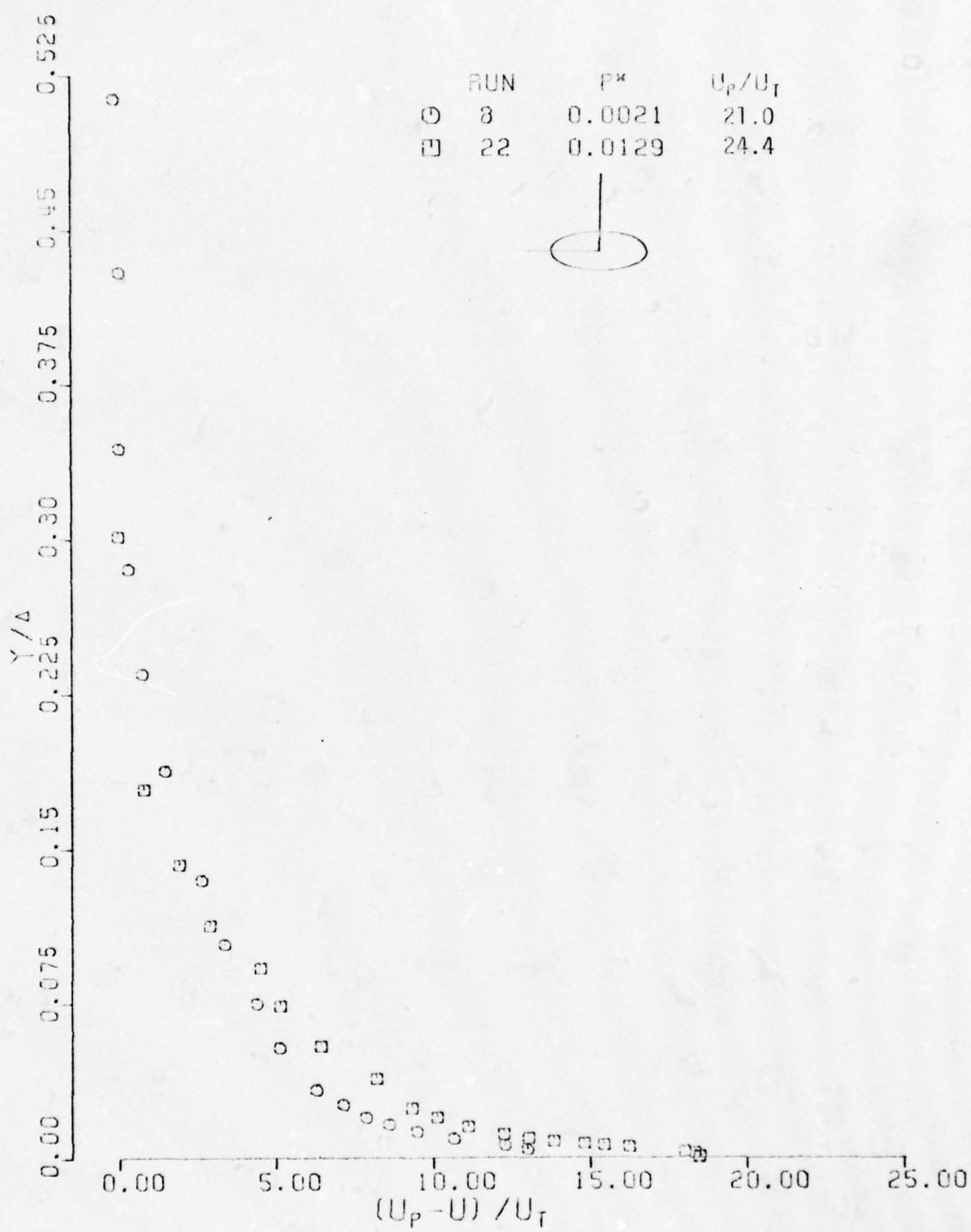


FIG.53 THE VELOCITY DEFECT LAW

ALPHA=0 °

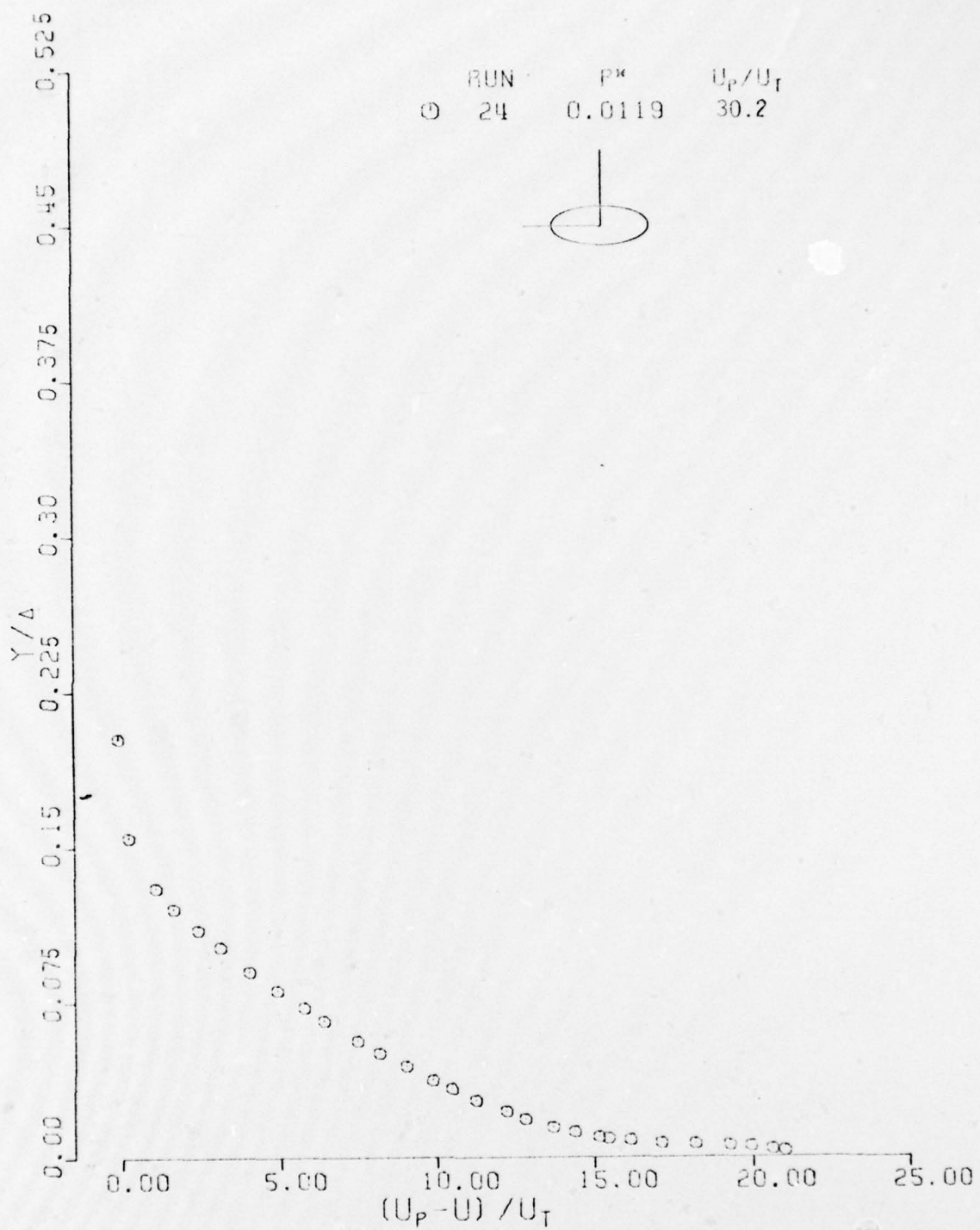


FIG.54 THE VELOCITY DEFECT LAW

ALPHA=0 °

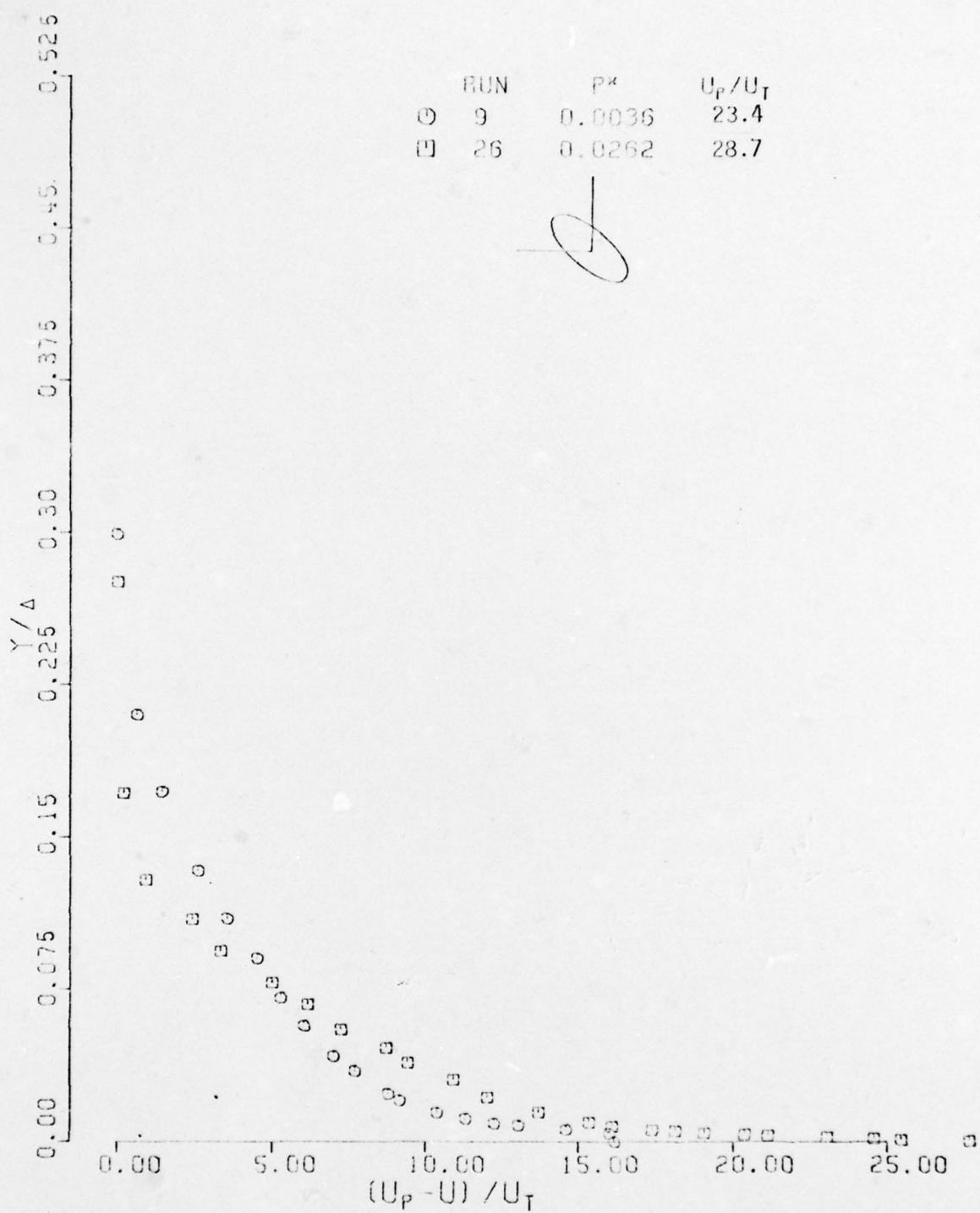


FIG.55 THE VELOCITY DEFECT LAW

ALPHA=45 °

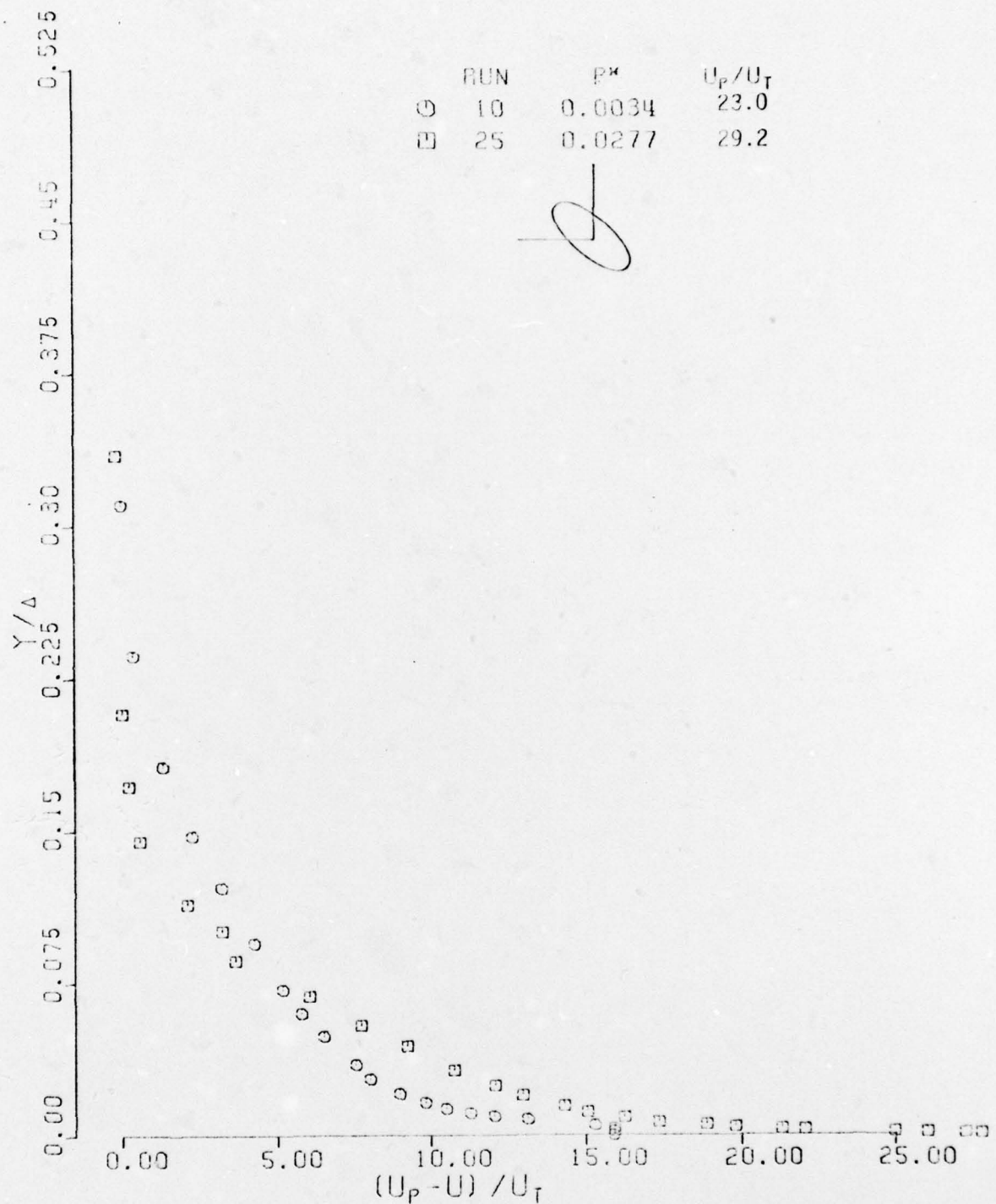


FIG.56 THE VELOCITY DEFECT LAW

ALPHA=45 °

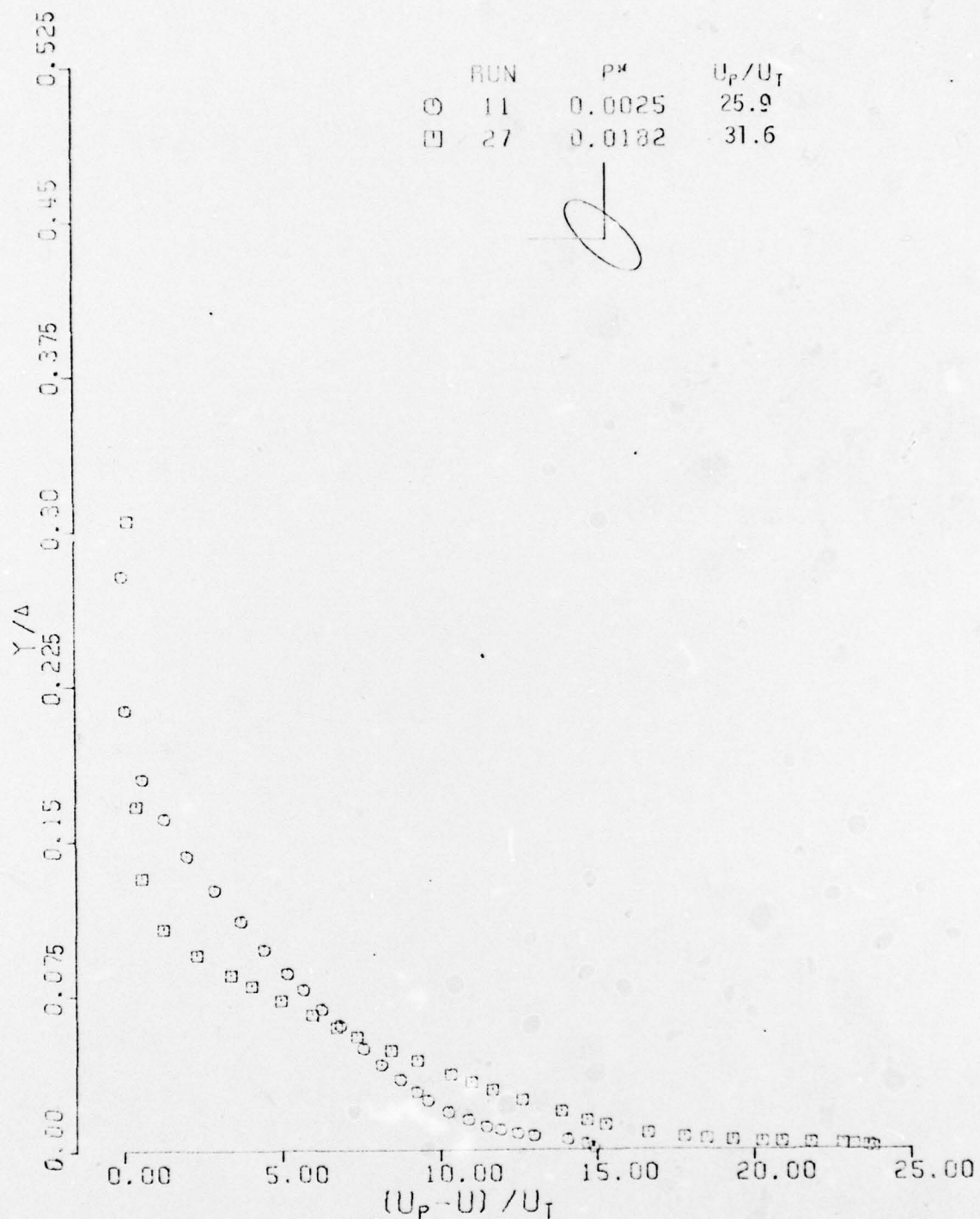


FIG.57 THE VELOCITY DEFECT LAW  
ALPHA=45°

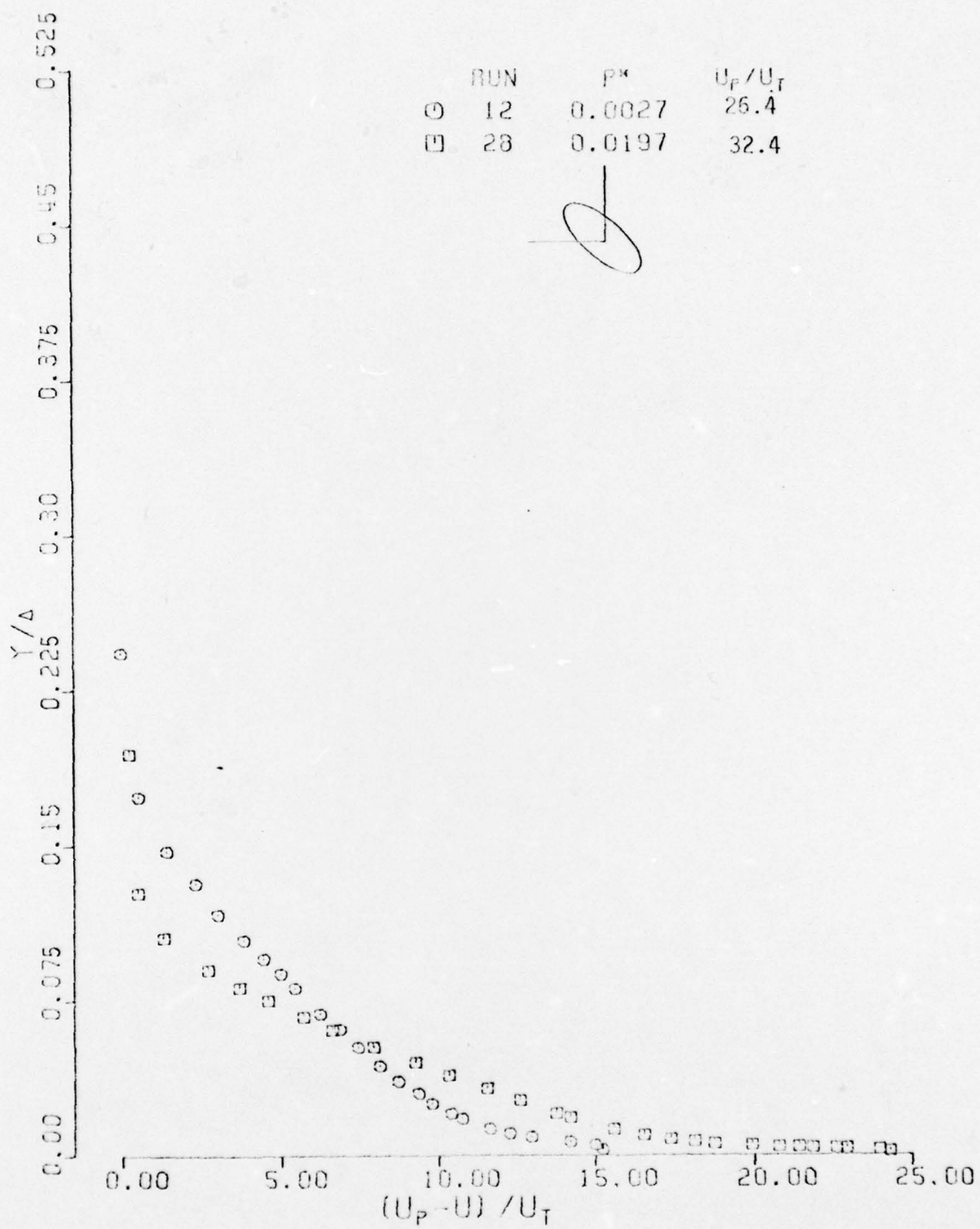


FIG.58 THE VELOCITY DEFECT LAW  
ALPHA=45 °

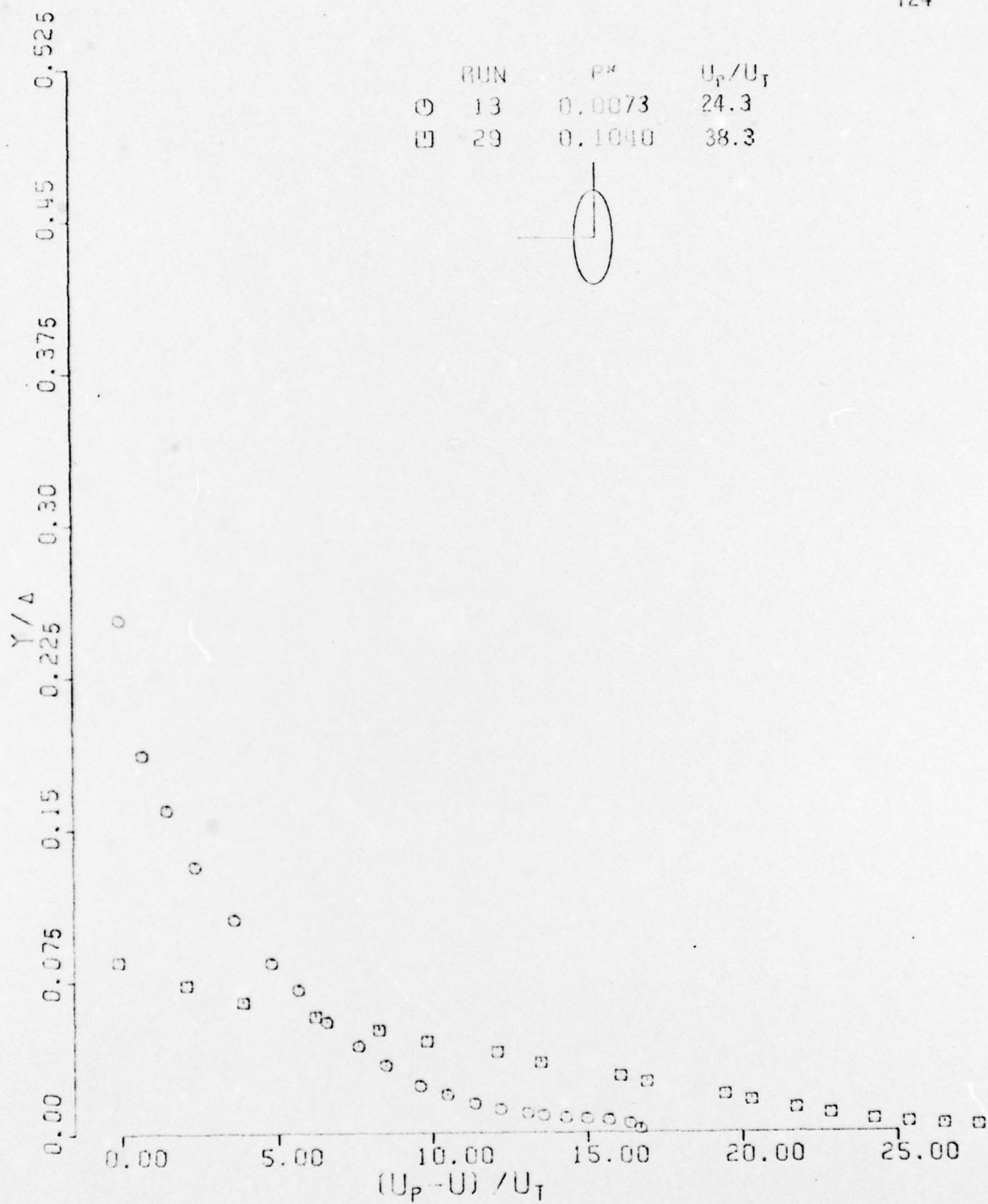


FIG.59 THE VELOCITY DEFECT LAW  
 $\text{ALPHA}=90^\circ$

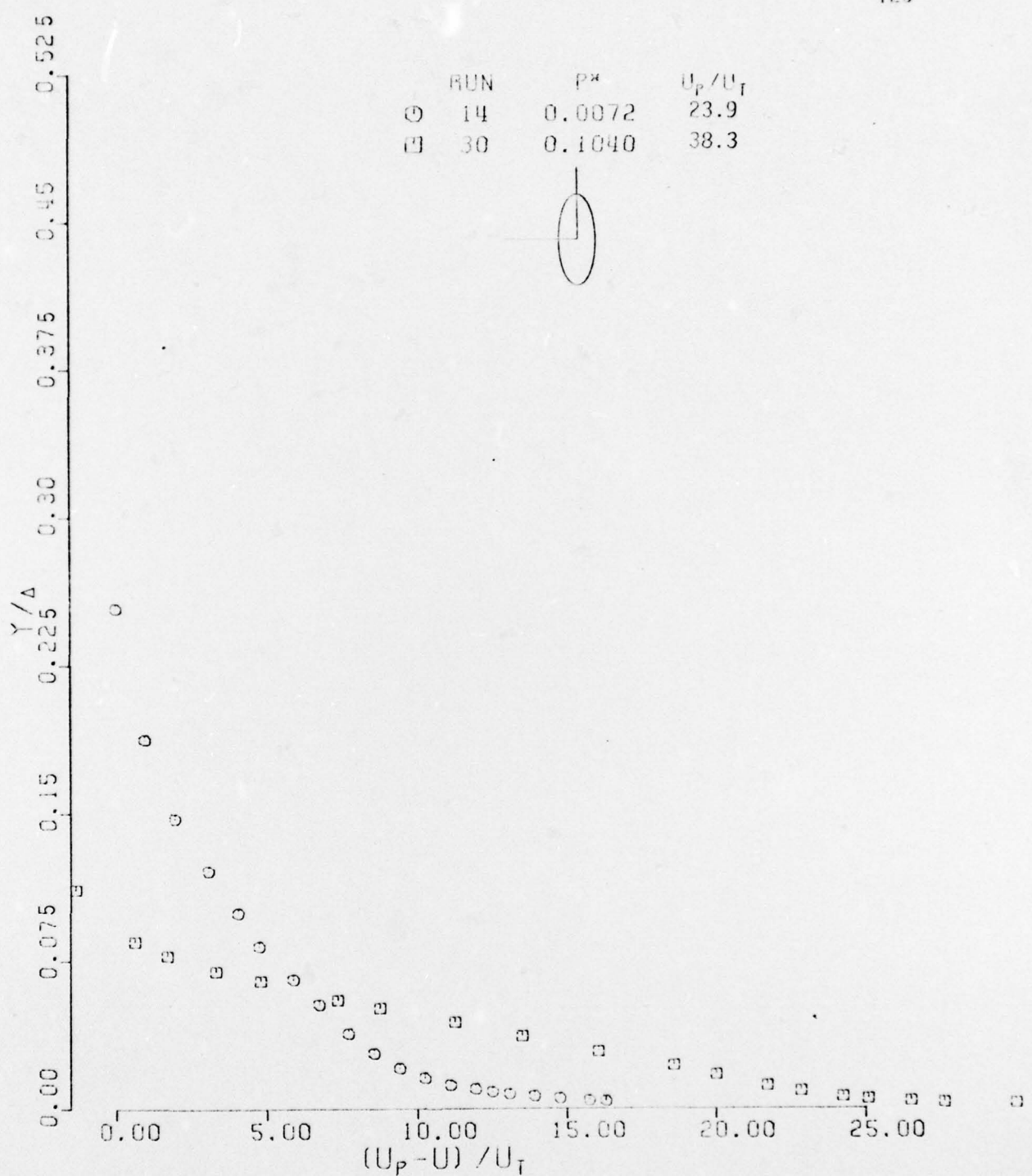


FIG.60 THE VELOCITY DEFECT LAW  
ALPHA=90°

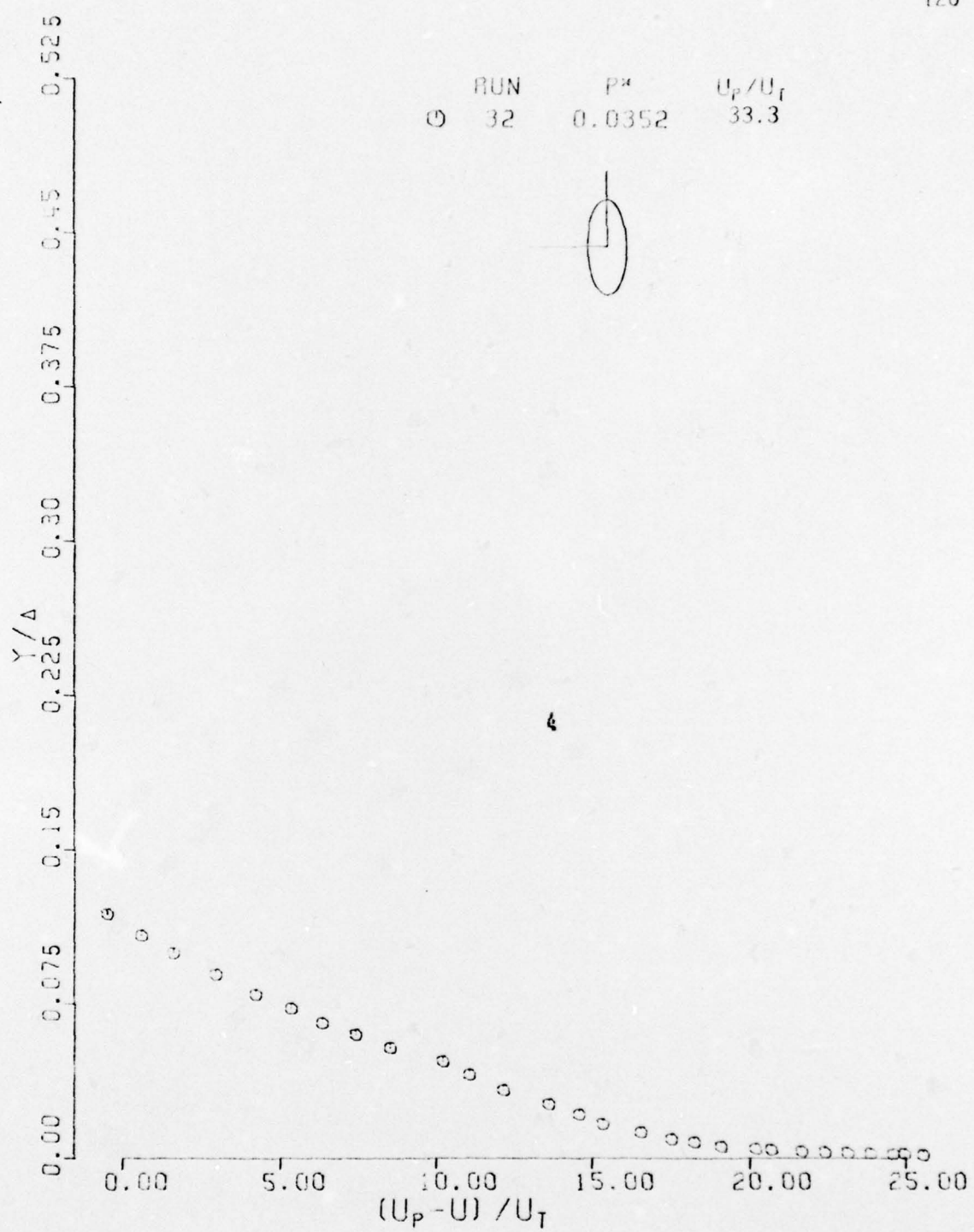


FIG.61 THE VELOCITY DEFECT LAW

ALPHA=90 °

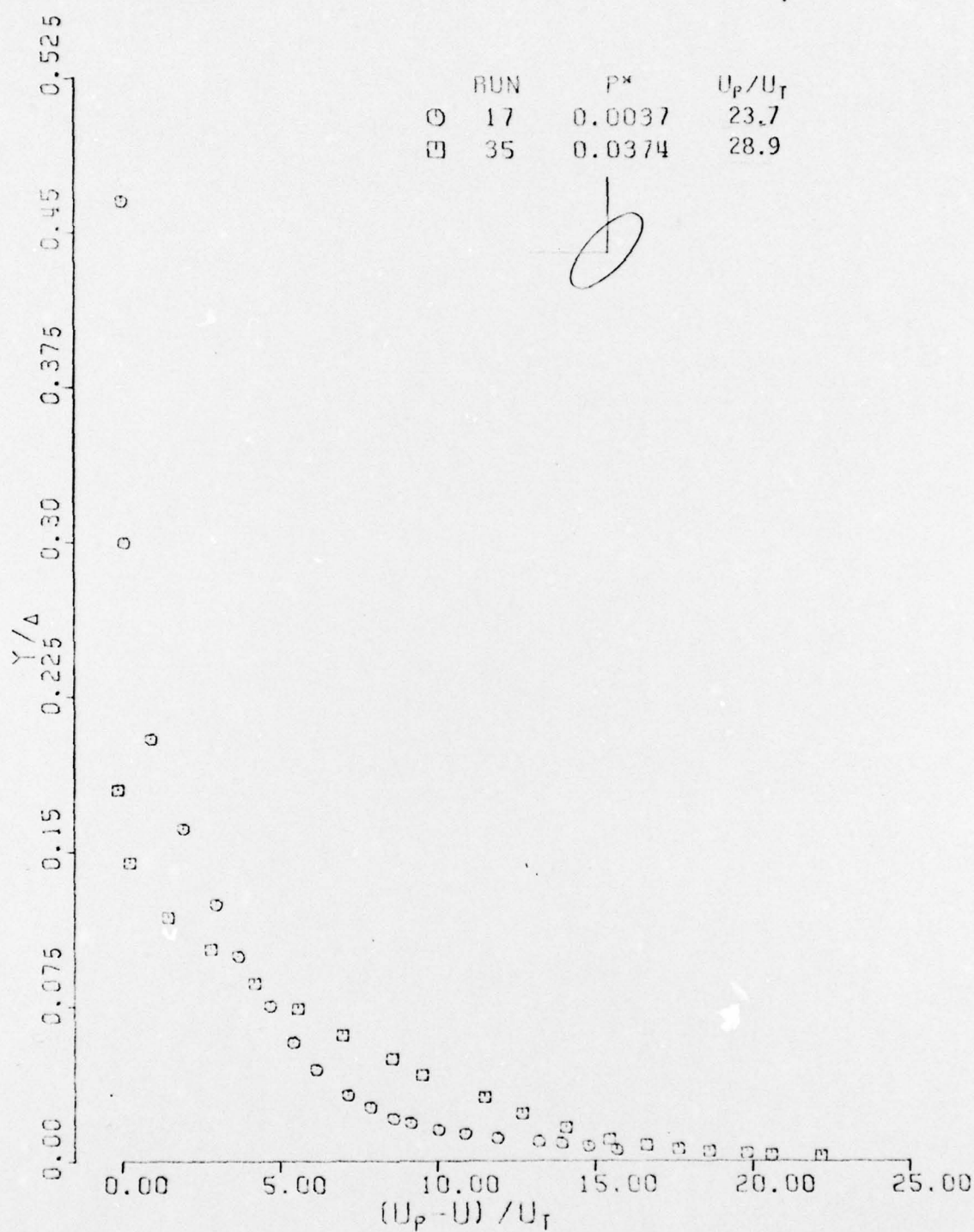


FIG.62 THE VELOCITY DEFECT LAW  
ALPHA=135°

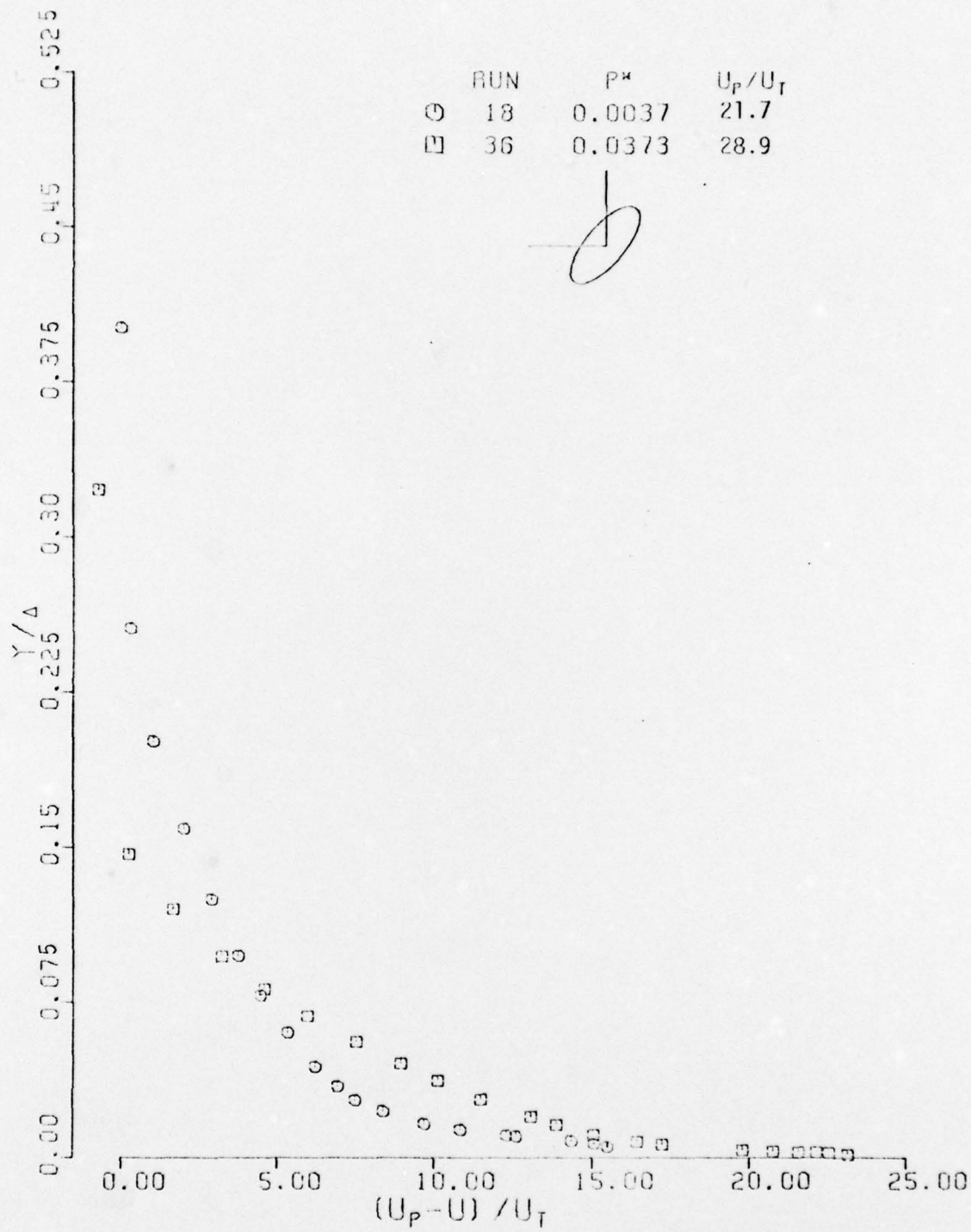


FIG.63 THE VELOCITY DEFECT LAW

ALPHA=135°

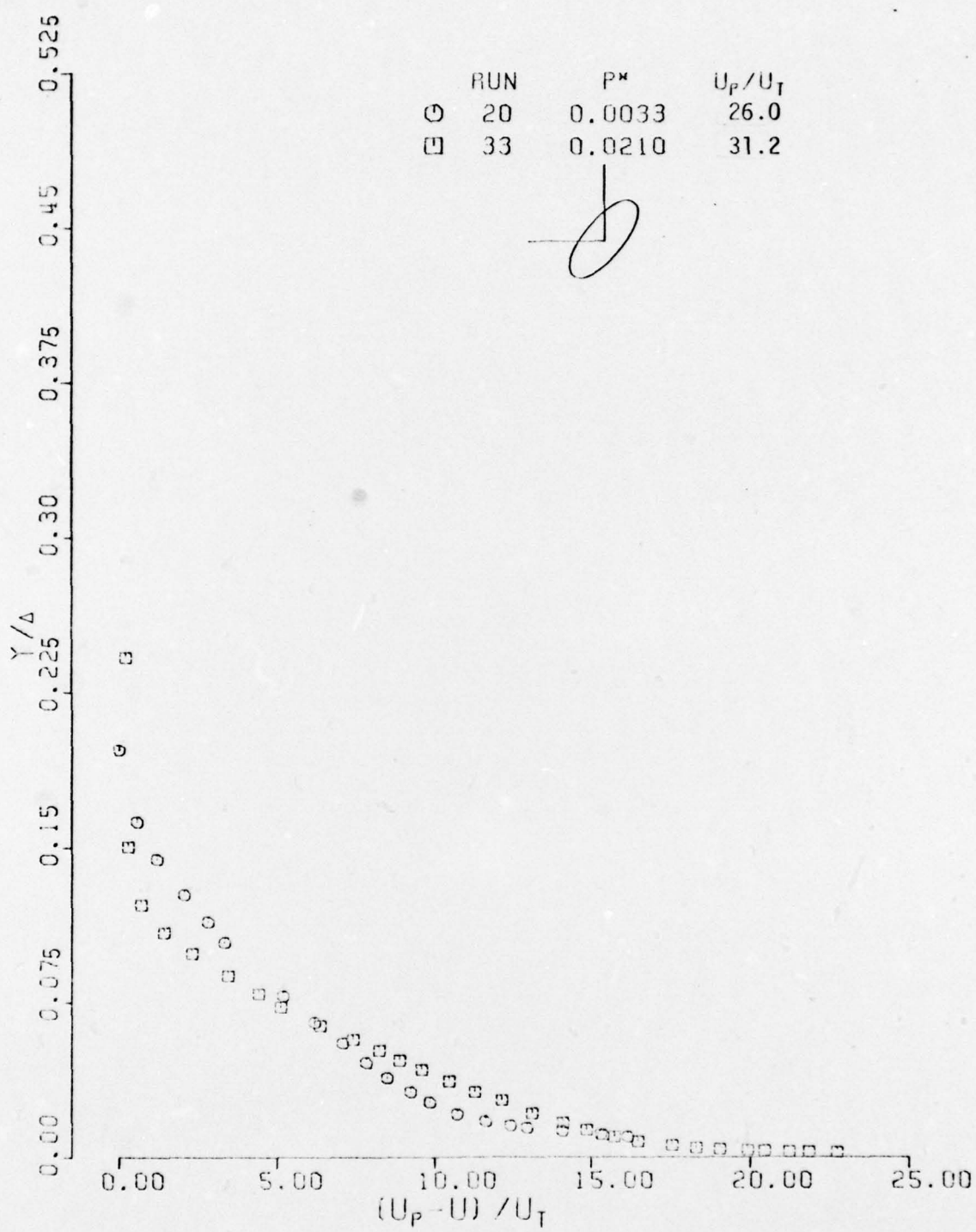


FIG.64 THE VELOCITY DEFECT LAW

ALPHA=135°

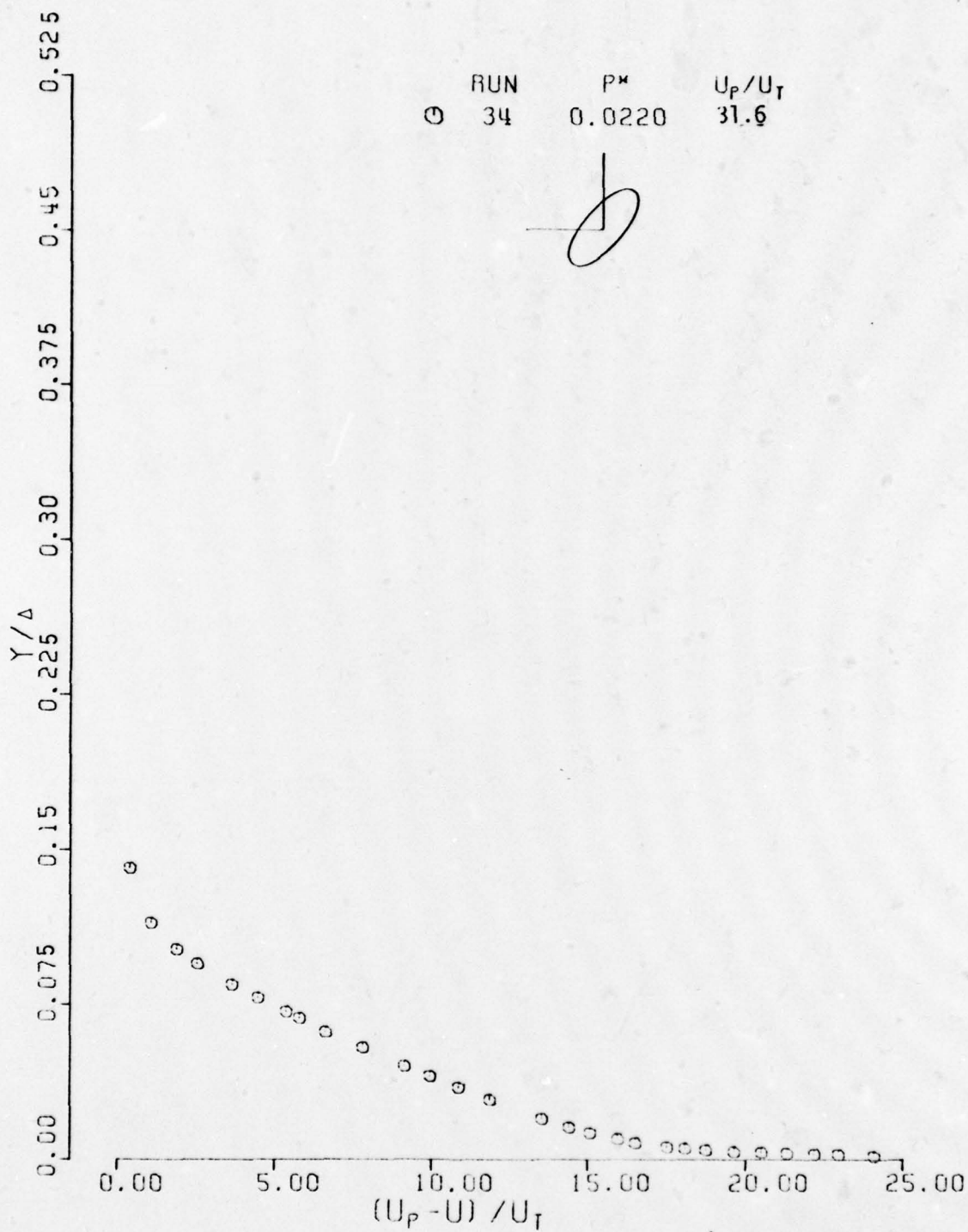


FIG.65 THE VELOCITY DEFECT LAW

ALPHA=135°

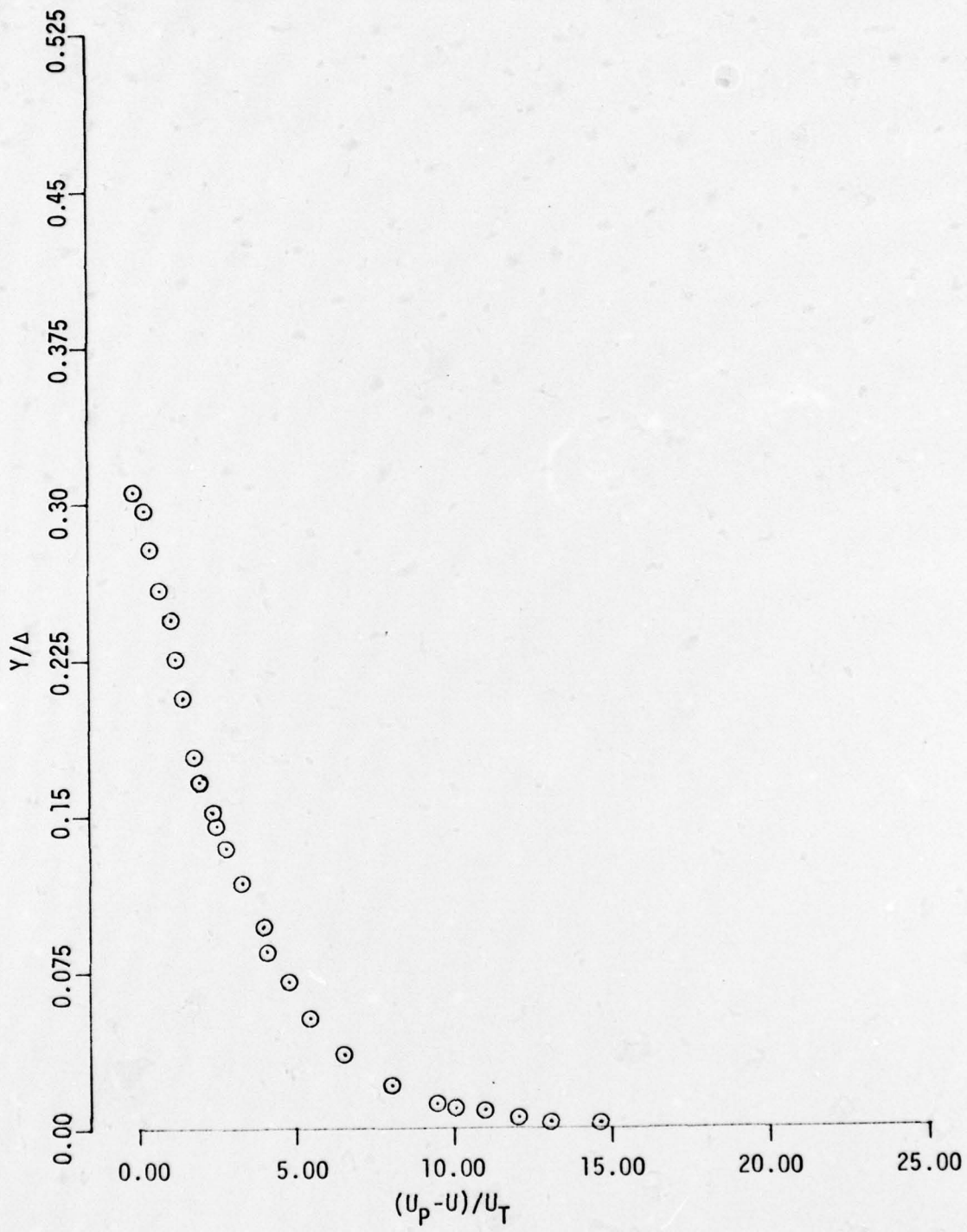


FIG. 66 THE VELOCITY DEFECT LAW  
FLAT PLATE TURBULENT BOUNDARY LAYER PROFILE FROM PHASE 1

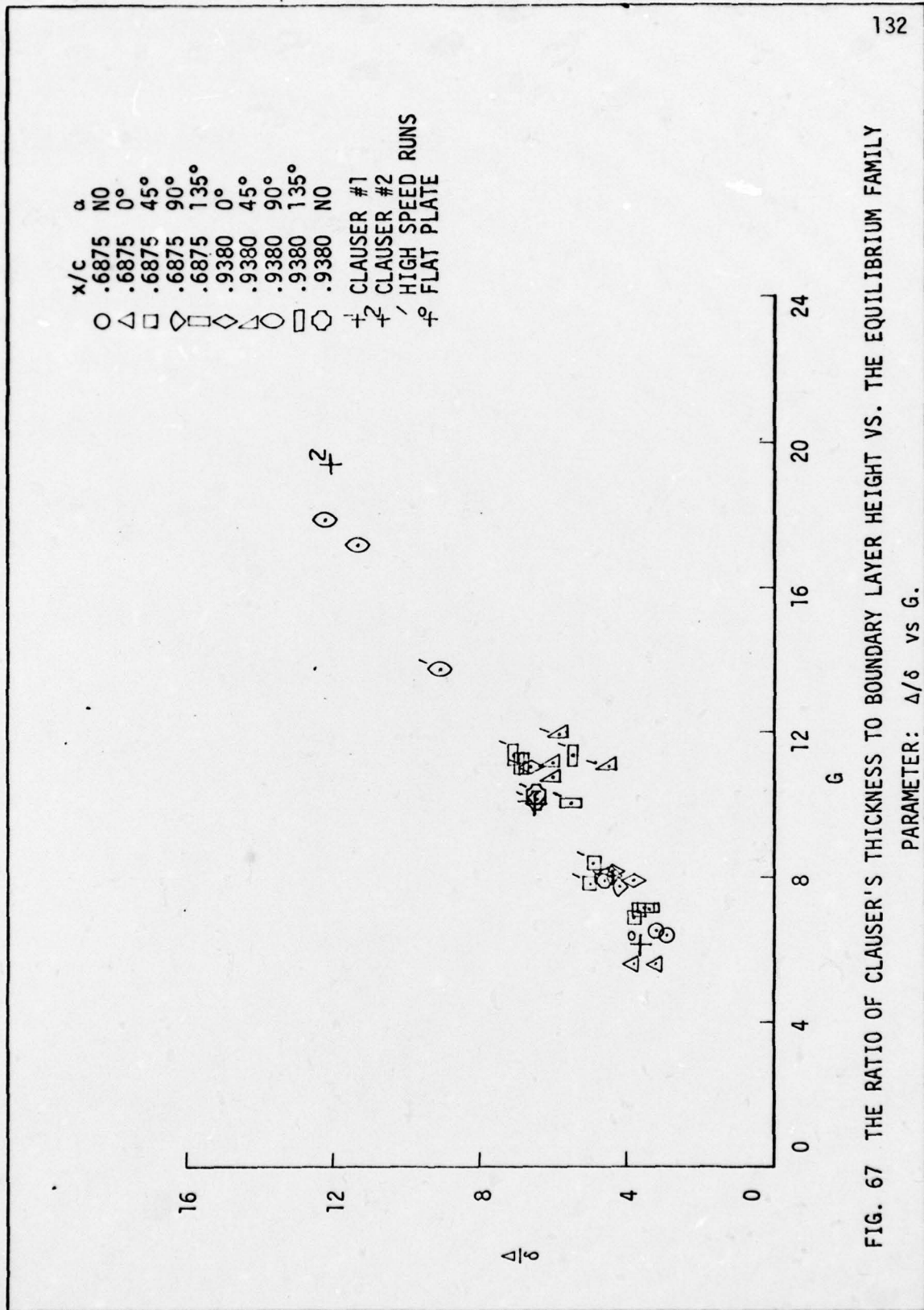


FIG. 67 THE RATIO OF CLAUSER'S THICKNESS TO BOUNDARY LAYER HEIGHT VS. THE EQUILIBRIUM FAMILY  
PARAMETER:  $\Delta/\delta$  vs  $G$ .